LIÈGE université Library

https://lib.uliege.be

https://matheo.uliege.be

Master thesis and internship[BR]- Master's thesis : Imaging characterization of the radial-velocity brown dwarf HD18757B[BR]- Integration internship

Auteur : Teloi, Mayané
Promoteur(s) : Maire, Anne-Lise; Loicq, Jerome
Faculté : Faculté des Sciences appliquées
Diplôme : Master en ingénieur civil en aérospatiale, à finalité spécialisée en "aerospace engineering"
Année académique : 2020-2021
URI/URL : http://hdl.handle.net/2268.2/11572

Avertissement à l'attention des usagers :

Tous les documents placés en accès ouvert sur le site le site MatheO sont protégés par le droit d'auteur. Conformément aux principes énoncés par la "Budapest Open Access Initiative"(BOAI, 2002), l'utilisateur du site peut lire, télécharger, copier, transmettre, imprimer, chercher ou faire un lien vers le texte intégral de ces documents, les disséquer pour les indexer, s'en servir de données pour un logiciel, ou s'en servir à toute autre fin légale (ou prévue par la réglementation relative au droit d'auteur). Toute utilisation du document à des fins commerciales est strictement interdite.

Par ailleurs, l'utilisateur s'engage à respecter les droits moraux de l'auteur, principalement le droit à l'intégrité de l'oeuvre et le droit de paternité et ce dans toute utilisation que l'utilisateur entreprend. Ainsi, à titre d'exemple, lorsqu'il reproduira un document par extrait ou dans son intégralité, l'utilisateur citera de manière complète les sources telles que mentionnées ci-dessus. Toute utilisation non explicitement autorisée ci-avant (telle que par exemple, la modification du document ou son résumé) nécessite l'autorisation préalable et expresse des auteurs ou de leurs ayants droit.

Imaging characterization of the radial-velocity brown dwarf HD18757B

University of Liège

Faculty of Applied Sciences

Supervisors:
Dr. Anne-Lise Maire
Pr. Jérome Loicq

Author:
Mayana Teloi

Thesis committee:
Pr. Damien Hutsemekers
Dr. Christian Delacroix

A thesis submitted in fulfillment of the requirements for the degree of Aerospace Engineering

Academic Year 2020-2021

Abstract

Context. A long radial velocity survey that started with Elodie and then extended with Sophie spectrographs discovered a potential companion around a sun-like star of 11.4 Gyr, called HD18757 and situated at 24.2 pc. This survey outcomes a potential substellar companion revolving around HD18757 with an angular separation of 0.9±0.1 arcsec, a period of 109 yr and a minimal mass of 35.2±1.2 M_{jup}. Regarding these characteristics, the object is drawn as a brown dwarf candidate.

Aims. In order to verify the substellar nature of the object, it is essential to characterize the orbital parameters, the spectral type and to constrain the dynamical mass of the companion, named HD18757B. Identifying such a substellar object allows to increase our understanding on their formation, their composition and their nature.

Methods. To do so, several techniques are applied to retrieve the photometric and orbital information. At first, HD18757B is observed in the L' band with the imaging instrument LMIRCam mounted on the Large Binocular Telescope. This observation is based on the high contrast angular differential imaging method and is further processed with the Vortex Image Processing package. Secondly, imaging data is coupled with astrometric observation from Gaia/Hipparcos and radial velocity measurements from Sophie and Elodie to run in a Markov-Chain Monte Carlo simulation. Finally, the measured parameters are compared to the properties of brown dwarfs from evolutionary and formation models.

Results. The angular differential imaging analysis shows no detection of HD18757B which implies an old and faint substellar object. Regarding the Markov-Chain Monte Carlo study, it constrains all orbital parameters but the inclination and the longitude of ascending node leading to two sets of solutions: prograde and retrograde orbits. In addition to the orbit determination, the Markov-Chain Monte Carlo establishes the companion dynamical mass of $36.528^{+2.261}_{-2.134}$ M_{jup} and predicts its positions at different epochs for direct imaging observations. Most important, this study strengthens the substellar hypothesis and draws a high elliptic wide-orbit object with an edge-on orientation. The fact that the orbit tends to an edge-on configuration indicates that the true companion mass is close to the one estimated with radial velocity measurements.
Furthermore, the evolutionary model predictions are in agreement with the direct imaging study as they depict a faint, cold and old substellar companion. More specifically, by assuming an age of 11.4 Gyr, the companion temperature varies within [514, 534] K, its radius's is approximately of [0.0849, 0.0862] R_{jup} and the luminosity is varying within [-6.321, -6.283]. With these characteristics, the companion is estimated to be a late T- or early Y-type brown dwarf, thus having respectively strong methane or ammonia in its atmosphere.
Lastly, formation models' predictions do not clear the ambiguity on the nature of brown dwarfs. Whether the Gravitational disk instability formation scenario that is appropriate for planet formation or the Protostellar disk fragmentation scenario for stars, both are relevant for HD18757B.

Key words.techniques: radial velocity - high contrast angular differential imaging - astrometry - methods: Vortex Image Processing - Markov-Chain Monte Carlo - stars: HD18757 - brown dwarfs

Contents

Introduction

Brown dwarfs are low mass objects, from 0.012 to 0.08 M_{sun}, which are standing between stars and planets. The occurrence of such substellar objects is pretty low, especially in binary systems. Typically, researchers discovered that at orbital separations of 0-3 AU, their occurrence is less than 5% (known as the Brown Dwarf Desert), around 10-1000 AU, they are found at 2-4% and beyond this separation, their frequency is estimated to 18%.[1]
Observation of such substellar objects is challenging due to their particular features, those are described in section 1. Regarding their low occurrence and their detection difficulty, current brown dwarfs' models contain uncertainties. Therefore the characterization of substellar companions is essential to improve understanding on their nature and enhance formation and evolutionary models.

A 20-year radial velocity survey with spectrographs Sophie and Elodie highlighted several wide-orbit potential brown dwarfs around sun-like stars.
The study all along this thesis focuses on the description of one particular binary system: HD18757 and its companion. The star HD18757 is located at 24.2 pc from Earth and its age is estimated to be 11.4 Gyr. With radial velocity measurements of this star, several features of the companion HD18757B are estimated such as a minimal mass of 35.2±1.2 M_{jup}, a semi-major axis of 0.9±0.1 arcsec and a period of 109 yr.[2] In regards to those characteristics and in particular to the low mass, the companion is a promising brown dwarf. However, the radial velocity method cannot constrain the object dynamical mass, nor can it establish all the orbital parameters of the object, in particular the inclination. For this reason, complementary observation techniques are used such as the high contrast angular differential imaging and astrometry. Altogether, three detection methods are adopted to characterize this binary system and are described in section 2.

To verify the substellar nature of the companion, we observe HD18757B in the L' band with the LMIRCam instrument that is mounted on the Large Binocular Telescope.[3] LMIRCam is an imaging instrument that allows high contrast angular differential imaging, thus providing speckles attenuated scientific images.[4] The data obtained from the LBT is processed via the Vortex Image Processing package developed by the University of Liège. The processing part explained in section 3, is divided in a pre- and post-process analysis which final aim is to spot a potential companion.[5] To demonstrate the performances of the Vortex Image Processing package and to verify the processing methodology, an additional dataset is considered and reviewed in section 3.3.[6]

Following the direct imaging analysis, a Markov-Chain Monte Carlo study is performed on the system in order to constrain the orbital parameters of HD18757B, to estimate its dynamical mass and to assess its orbit orientation on the sky. This analysis, detailed in section 4, combines information from the radial velocity measurement, the direct imaging observation and the astrometric evaluation.[7]

At the end of these two evaluations, the mass of the substellar object is constrained, which allows to further study the companion characteristics. This is done via an analysis with evolutionary models that predicts the object parameters such as the bolometric luminosity, the effective temperature and the radius.[8, 9, 10, 11] These properties enable to assess the object spectral type, discussed in section 5, and strengthens the brown dwarf initial assumption. In addition to the evolutionary model discussion, a comparison between current brown dwarf's formation models is developed in section 6. This discussion targets two formation scenarios, the Gravitational disk instability used for planets and the Protostellar disk fragmentation adequate for stars, and assesses their suitability for HD18757B.[12, 13]

The results of all analyses and the perspectives for future work are summarized in section 7. The perspectives part consists in a review of future and current space- and ground-based telescopes appropriate to image the object and an introduction to the new Gaia Early Data Release 3 astrometric measurements in order to improve the orbital fit.[14]

1 What is a brown dwarf ?

A brown dwarf is an object classified as substellar given the ambiguity of its nature, not a planet nor a star but in between.
A star is characterized by nuclear fusion in its core with an autoregulated energy production. This regulation means that if the energy production is reduced, it will induce the pressure to decrease which consequently will lead to a contraction of the core. Later results in an increase in pressure and temperature, thus triggering the energy production back.[15]
The chemical reactions taking place in stars are exclusively nuclear fusion and are started by the proton-proton chain given in Equation 1.1:

$$
\begin{aligned}
{}^1\mathrm{H} + {}^1\mathrm{H} &\rightarrow {}^2\mathrm{H} + \mathrm{e}^+ + v \\
{}^2\mathrm{H} + {}^1\mathrm{H} &\rightarrow {}^3\mathrm{He} + \gamma \\
{}^3\mathrm{He} + {}^3\mathrm{He} &\rightarrow {}^6\mathrm{Be} \\
{}^6\mathrm{Be} &\rightarrow {}^4\mathrm{He} + 2{}^1\mathrm{H}
\end{aligned}
\tag{1.1}
$$

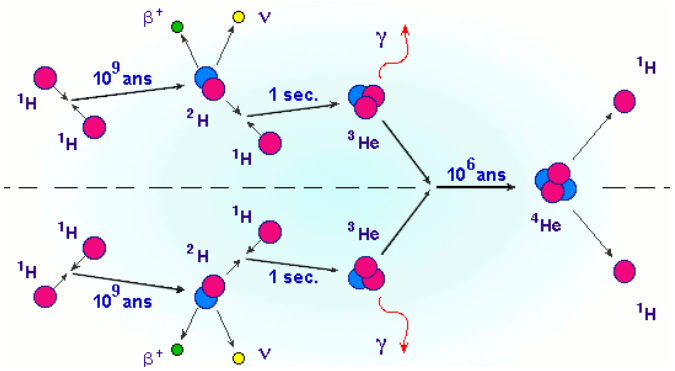

FIGURE 1.1: Graphical representation and time-scale of the proton-proton chain where β^+ or e^+ is a positron, γ is a high energy photon (gamma ray) and ν is a neutrino.[16]

This chain is activated at temperatures above 10^7 K and continues with helium fusion for stars with mass similar to the Sun. Nuclear reactions can go further with the fusion of heavier nuclei at higher temperatures for more massive stars.
As brown dwarfs are less massive than sun-like stars, typically between 0.012 M_{sun} and 0.08 M_{sun} at formation, not all are massive enough to go further than the deuterium's fusion, which is the first step of the proton-proton chain, confer Equation 1.1. For this reason, the International Astronomical Union sets the deuterium fusion as the limit between brown dwarfs and planets. This limit corresponds to an object mass of 0.012 M_{sun} or 13 M_{jup} below which the object has not enough mass to initiate the proton-proton chain and is considered as a planet.
The upper limit of 0.08 M_{sun} is the mass required to initiate hydrogen fusion and thus sets the separation between brown dwarfs and stars. Within these established limits, low mass brown dwarfs can fuse deuterium and more massive ones can go up to lithium fusion.[1]

Even though these substellar objects fuse some nuclei at the beginning of their life, the nuclear reactions in their core are not sustained. As a result, brown dwarfs do not have an autoregulated energy production which leads to very different evolution patterns compared to stars. Stars on the main sequence mostly undergo an increase in luminosity and the expansion of their stellar core. While brown dwarfs are subjected to a decrease in temperature, luminosity and a contraction of their substellar core with time.

Considering their internal nuclear reactions and evolution pattern over time, these low mass objects can pass through several stages such as the M, L, T or Y type. These spectral classes characterize a star in terms of its effective temperature, luminosity and atmospheric composition.
From Figure 1.2, it can be noticed that all types are distinct from each other due to different absorption bands at specific wavelengths. Besides this particularity, the spectral types are mainly classified with respect to the effective temperature. As explained previously, a brown dwarf cools down with time due the lack of energy production. Therefore, cool brown dwarfs are usually considered to be at the end of their life while warmer ones are assumed to be young. With this perspective, young objects are classified as M-type for temperatures ranging in [3000, 4000] K, then comes the L-type with temperatures from 2000 K down to 1300 K, the T-type temperatures within [700, 1300] K and eventually the Y-type which is the ultra-cool one with temperatures reaching 200 K.[18]
In reality, the transition from one class to another is not so clearly defined and the types are subdivided into sub-classes to provide a more accurate description.

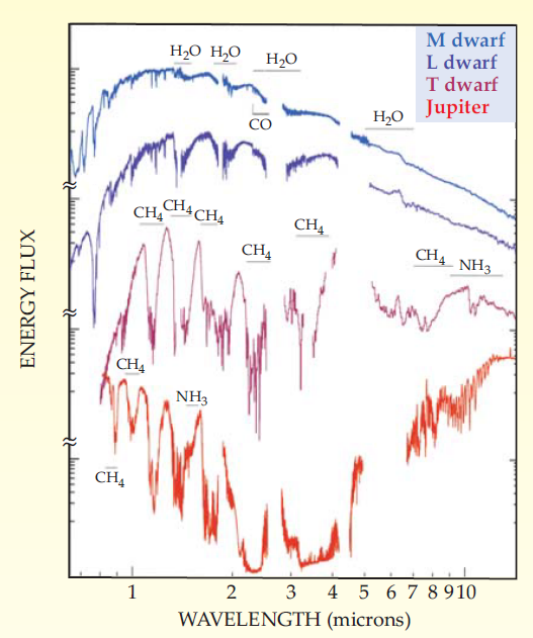

FIGURE 1.2: Near-infrared spectra of M, L and T type brown dwarfs.[17]

In order to verify the spectral type of an object, its spectrum must be retrieved via imaging methods. The first observed brown dwarf was Teide 1 via the direct imaging method in 1995. Since this first discovery, many brown dwarfs have been found through several techniques such as the radial velocity and the transit method.[1] In point of fact, imaging these substellar objects is challenging in several ways, especially the ones evolving in binary systems with main sequence stars. Such substellar companions are hard to image from Earth due to the large contrast difference between the object and the stellar brightness, the small angular separation between the object and the host star, and perturbations induced by Earth's atmosphere. The contrast difference is of the order of $[10^{-10}, 10^{-2}]$ depending on the spectral type of the star and the object, and the angular separation typically varies between [0.1, 5] arcsec.

To attenuate the star's luminosity, researchers use coronagraphic masking and tend to observe in the near infrared, corresponding to wavelengths in [1, 3] µm, where the star's luminosity is low compared to the companion's higher thermal emission.[19] However observing at small wavelengths constrains the angular resolution given by:

$$\theta = 1.22\frac{\lambda}{D} \tag{1.2}$$

where θ is the instrument's angular resolution, λ is the wavelength at which the instrument observes and D is the instrument's aperture.[20]

If two observed objects have an angular separation smaller than θ, such as being close to each other, then the image is unresolved and blurry. This condition, better known as the Rayleigh Criterion and depicted in Figure 1.3, states that "*the imaging process is said to be diffraction-limited when the first diffraction minimum of the image of one source point coincides with the maximum of another*".[21]
Therefore the angular resolution is limited by the diffraction limit of the instrument which depends on the lens aperture and the wavelength as presented in Equation 1.2. Since the wavelength varies within [1, 3] µm, the only parameter that allows to reach high angular resolution is the lens' diameter. As a result, observations in the near infrared require large aperture telescopes to reach high angular resolution.

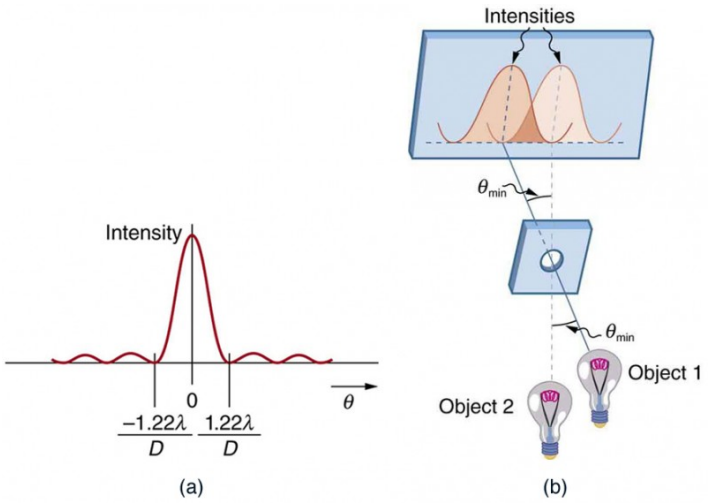

FIGURE 1.3: (a) Graph of intensity of the diffraction pattern for a circular aperture. (b) Two point objects produce overlapping diffraction patterns. Shown here is the Rayleigh criterion for being just resolvable. The central maximum of one pattern lies on the first minimum of the other.[22]

In addition to the instrument diffraction limit, the small angular separation matter leads to two main technical difficulties. The first being the distinction between the companion's light emission and the one of the star that dominates. The second one is the instrumental aberrations creating speckles which account for the diffracted light from the telescope and the scattered light from wavefront aberrations.[1]
More precisely, speckles result from the interference of different spatially coherent[1] wavefronts and lead to small spots on the image.[23]
To solve these issues, technological improvements aim to build large aperture telescopes, use interferometers and observing imaging methods to improve resolution. One of the imaging methods currently used is the angular differential imaging technique which is applied in this project and developed in section 2.1.

Regarding Earth's atmospheric perturbations, they are minimized via the use of adaptive optics. Atmospheric perturbations are caused by the variation of the diffraction index due to the temperature difference between the atmospheric layers. Subsequently, it results in the distortion of the light rays.[19] In order to flatten the distorted wavefronts, mirrors are monitored through actuators. More specifically, wavefronts sensors measure wavefront fluctuations which are then processed through a control loop and a read-time computer. Subsequently, the computer send the information to actuators that adapt in consequence the mirrors positioning.[1]

Another brown dwarfs intriguing characteristic is their low occurrence nearby stars. This paucity of brown dwarfs in the vicinity of other stars is called 'The Brown Dwarf desert'.[24]
The region called 'the desert' covers distances around host stars smaller than 3 au and targets objects with masses in the range of 10-80 M_{jup}.[1] The origin of this desert is not completely understand but several theories related this phenomenon to formation mechanisms such as migration and external interactions.[25]

This review highlights that brown dwarfs are very peculiar as their properties portray them as very small stars (failed stars) and giant planets, thus positioning them at the separation between planets and stars. Regarding brown dwarfs ambiguous phenomenology and particular properties, these substellar objects are of great interest for scientists.

[1]Coherence represents a constant phase relation between two waves. Spatial Coherence is a measure of the correlation of a light wave's phase at different points transverse to the direction of propagation.[23]

2 Detection methods

Brown dwarfs or exoplanets can be detected with different methods which are classified in two main categories: indirect and direct methods.
Direct methods consist in detecting the object visually but they are limited by the instruments' resolution. While indirect methods find the object via the object's influence on the host star. This influence can have various forms such as a variation in the star's luminosity or a fluctuation in the star's radial velocity.

Host star	RA [deg]	DEC [deg]	Distance [pc]	Age [Gyr]	Spectral type	[Fe/H] [dex]
HD18757	46.040	61.706	24.2	11.04+/-0.1	G4V	-0.27+/-0.02

TABLE 2.1: Characteristics of the host star HD18757 where RA and DEC are the right ascension and declination, and [Fe/H] represents the metallicity. Data from *Bouchy et al. 2016*

In this analysis, the star HD18757[2], which characteristics are gathered in Table 2.1, was observed by spectrographs Sophie and Elodie at different epochs to measure its radial velocity.[2] In addition to these measurements, we observed this star with the LMIRCam camera on the Large Binocular Telescope. To complement radial velocity measurements and direct imaging information, the companion's motion and positions were calculated via astrometric data from Gaia and Hipparcos.[27]
These three methods are described in detail in the following sections.

2.1 Angular differential imaging

The high-contrast direct imaging with ground-based telescopes allows to extract the spectrum of observed objects, consequently enabling the study of the atmosphere composition and effective temperature of the object. The major disadvantages of this method are the contrast difference and the angular separation between the host star and the companion, and the aberrations caused by the optical system and the Earth's atmosphere. The former is a limitation of the direct imaging method, while the latter is corrected with adaptive optics and a new observation strategy, the angular differential imaging (ADI).[1]

The angular differential imaging is a high contrast direct imaging technique. This technique relies on ground based-telescopes that observe the sky in pupil-stabilized or pupil-tracking mode. It means that the pupil of the telescope is stabilized on the detector, thus allowing the field of view to rotate with respect to the instrument. The aim of this strategy is to attenuate the quasi-static speckles coming from the imperfections of the optical instruments mounted on the telescope while preserving the companion's signal. With long exposure time, the aberrations caused by the telescope's mirrors mutate into a quasi-static noise. In order to attenuate this noise, the pupil is fixed to maintain the speckles stable, while the field of view rotates leading to a circular trajectory of the companion. The angle at which the field of view rotates is called the parallactic angle and is thus associated to each image. Therefore images or frames obtained are centered at a source point around which the background is rotating at a given parallactic angle and where the speckles are fixed.[4]
Since the speckles are fixed along the frames, the median of the stack accounts for the quasi-static speckles and leaves few traces of the companion's signal. This median is then removed from each frame leaving the companion's signal and the remaining uncorrelated component of the quasi-static speckle noise. By superimposing and de-rotating these frames, the signal of the companion is enhanced and the remaining noise is further averaged in the background.

This methodology is depicted in Figure 2.1 where A_i represent the raw frames.[28] The information that is removed from the cube, represented by B, is contained in the point spread function (PSF). Therefore,

[2]HD stands for Henry Draper Catalogue which is an astrometric and spectroscopic data catalogue for more than 225,000 of the brightest stars visible from the Northern Hemisphere.[26]

the methodology aims to model a reference point spread function which is then subtracted from the cube. The PSF characterizes the intensity distribution of the point source over the image, in other words it represents the degree of spreading of the host star's luminosity. This reference PSF can be computed with several algorithms based on the principal component analysis (PCA) or locally optimized combination of images (LOCI) method. Actually, there are a lot of different models but none that outperforms all the others since they have different strategies, computation times, advantages and disadvantages.[29] Therefore, many models relying on different approaches are developed in order to continually improve the speckles attenuation performances and thus reach higher contrasts. Moreover, the use of several algorithms allows to verify whether the detected signal is a companion or not by comparing the output between those algorithms. For instance, if algorithm 1 finds a potential companion at a certain position, the fact that algorithm 2 detects the same signal strengthens the result. These strategies are developed in further details in the post-processing paragraph.[29]

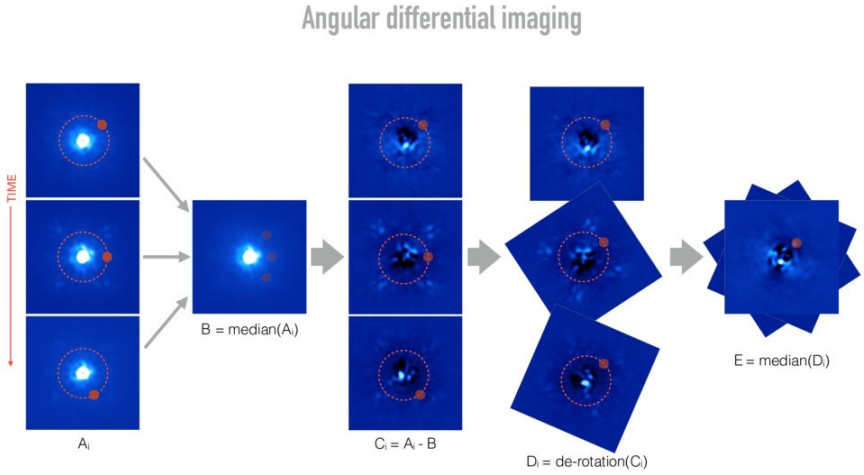

FIGURE 2.1: Model PSF subtraction general.(*Marois et al. 2006)*[30]

To summarize, an ADI dataset includes a 3D cube of several raw frames covering a certain period of time with fixed speckles and rotating substellar objects, the corresponding parallactic angles for each frame and a measured point-spread function.

In order to retrieve useful information from the ADI dataset such as contrast curves, signal-to-noise ratio maps or to detect companions, it is essential to apply pre- and post-processing procedures.
The pre-processing is composed of several steps. First, each frame must be centered around the source in order to align the quasi-static speckles pattern along the frames. Second, frames can be cropped around the star in order to decrease the frame size and consequently the memory allocation. Third, bad frames are discarded to reduce the cube size and to prevent discrepancies in the results. Bad frames are defined as frames with low correlation with reference to a chosen threshold. By removing bad sequences in the cube, the remaining frames are more correlated which enables to model a better reference PSF. Fourth, bad pixels are corrected by interpolating with their neighbours. In order to reduce even further the size of the cube, it is possible to apply a pixel binning which recombines the information of several pixels into one. In addition to pixel binning, the cube can be sampled temporally by taking the mean of every n frames.[31]

These pre-processing operations lead to a smaller cube where the information is concentrated on less frames and a lower amount of pixels. This reduction in size of the ADI cube leads to lower computation time and hence faster simulations. However, such data reduction cannot be done at the expense of information. For instance, the pixel binning must not smear too much the companion's signal, the number of remaining frames must be reasonable in order to model a good reference PSF, the cropped frames must include the companion's signal and so on. Thus there is, all along the pre-processing steps, a trade-off between the information loss and the computation time.[31]

The post-processing consists in modeling the PSF from the ADI cube. Then using the modeled PSF, the quasi-static noise is subtracted from the frames. Finally, each frame is rotated in order to align them and superimposed onto the other.
As introduced previously, the PSF can be modeled via several algorithms based on the LOCI or the PCA family method. The LOCI methods implement a reference PSF based on linear combination of the frames composing the cube. A particular algorithm of this family is the 'Median Reference PSF subtraction' which computes a single reference PSF as the median of the stack.
Regarding the PCA family method, it is based on PCA processes that reduce the dimensions of large data by transforming a set of variables into a smaller one, called the principal components (PC). A particular algorithm of this family is the 'Full-frame ADI-PCA' that builds the reference PSF by projecting the image onto a lower-dimensional orthogonal basis derived from the data. The orthogonal basis is formed by the k PCs found via the eigenvalue decomposition of the covariance matrix $\mathrm{M}^T\mathrm{M}$, where M is a matrix $\in \mathbb{R}^{n\times p}$ with n the number of frames and p the total number of pixels in one frame. The principal components are chosen to take into consideration the aberrations while neglecting the companion signal. Low order PCs mainly contain the static features such as the speckles, whereas high order PCs account for dynamic features like the companion signal. Accordingly, increasing the number of PCs results in a better noise reduction, however, at a certain order, the signal of the companion is also considered, thus leading to auto-subtraction. Therefore, the number of PCs considered is a trade-off between the quasi-static speckles noise attenuation and the companion detection.[31]

2.2 Radial Velocity

The radial velocity technique (RV) is an indirect method to detect exoplanets or brown-dwarfs via the Doppler-effect. This method consists in analysing the spectrum of an object in order to determine any shift towards longer or shorter wavelengths. A shift towards longer wavelengths in the object's spectrum is called a redshift and means than the object is moving away from the Earth. On the contrary, a shift towards shorter wavelengths is considered as a blueshift and reveals an object moving towards the Earth. Regarding this behaviour, scientists look for periodic shift patterns in the spectrum of a star which reflects a back and forth motion of the studied star. This recurring movement is associated to the presence of a companion which is thus found indirectly.[32]

The Doppler formula links the redshift to the relative radial speed between the star and the companion thus allowing astronomers to represent radial velocity graphs. These radial velocity measurements form a sine-like curve which depends on the orbit eccentricity, the orbital period and the companion's minimal mass. For instance, the star HD18757 was observed by spectrographs Sophie and Elodie at different epochs. With the obtained spectrum, the periodic shift pattern is isolated and converted into radial velocity measurements as shown in Figure 2.2. For a perfectly circular orbit, the radial-velocity curve would depict a sine wave which semi-amplitude is noted κ. The semi-amplitude relates the orbital parameters to the minimal mass of the studied companion via:

$$K \approx \left(\frac{2\pi G}{P M_*^2}\right)^{\frac{1}{3}} \frac{M_{\text{planet}} \sin i}{\sqrt{1-e^2}} \qquad (2.1)$$

where K is the semi-amplitude, G is Newton's constant, M_* is the mass of the parent star, i is the

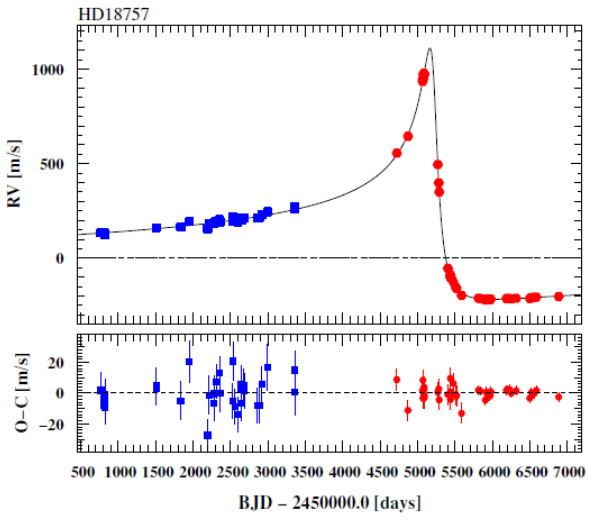

FIGURE 2.2: Radial velocity curve of HD18757 obtained with Elodie (blue) and Sophie (red). The residuals or systematic errors are displayed on the lower panel.[2]

inclination of the plane of the orbit with respect to
the plane of the sky, P the period and e the eccentricity.[33]

The parameter $M_{planet} \sin i$ represents the minimal mass of the companion which can be close or far from the real companion mass. This particularity is related to the orbit inclination that cannot be constrained because the measured motion is projected along the line of sight. The major disadvantage of the Doppler spectroscopy detection strategy is that it is more appropriate to edge-on orbits than face-on orbits and since the inclination is unknown, the derived mass is a lower limit. In addition to this limitation, the RV method is sensitive to stellar activity which is high for young stars. For this reason, this method tends to measure mature stars with lower activity, in contrast to the direct imaging method which is more appropriate for young exoplanets with high thermal emission.[32]

As already mentioned, the star HD18757 was observed via spectrographs Elodie and Sophie. The Elodie spectrograph is functional since 1993 and is located at the Haute-Provence Observatory. This instrument can achieve a spectral resolution R = 4200 at wavelengths from 0,391 µm to 0,681 µm.[34] Regarding the Sophie spectrograph, it is also situated at the Haute-Provence Observatory and its first light was obtained on July 2006. This spectrograph has two modes of resolution: high spectral resolution with R = 75000 and high efficiency resolution with R = 40000. The Sophie spectra cover wavelengths from 0.382 µm to 0.693 µm.[35]

2.3 Astrometry

Astrometry evaluates the position, the distance and the motion of stars. In particular, positions are evaluated as separation and position angle and motion is represented by proper motion (PM). The proper motion of a star is the apparent motion of the star across the celestial sphere and it is described by the right ascension and declination components.[36] More precisely, these components are angular distances that locate a point in the equatorial coordinate system, they can be seen as the longitude and latitude on the celestial sphere[3].

Proper motion measurements are important in order to determine potential companions around stars. A binary system has its photocenter dissociated from its center of mass due to the presence of the companion around the star. Therefore, by observing the proper motion of the photocenter, related to the star, and the one of the barycenter, it is possible to determine the influence of a companion. Astronomers look at the difference between the long-term proper motion that is associated to the center of mass, and the short-term proper motion that accounts for the photocenter and the barycenter of the system. This difference in the proper motions is called the proper motion anomaly (PMa) and is thus indicative of a companion orbiting the star.[27]

This strategy is based on a major assumption: the photocenter is associated to the star, thus neglecting the photometric contribution of the companion. Regarding this aspect, the astrometric observation method is effective for high luminous stars with faint companions but it introduces inconsistencies in the measurements for systems with bright companions. In this context, measuring our system via astrometry is consistent given the large contrast difference between HD18757B and its star.

In this analysis, proper motion datasets are obtained from the observations of Hipparcos and from the second data release of Gaia (GDR2). Hipparcos was a space astrometry mission that operated from 1989 to 1993 and mapped 118,218 stars.[37] Gaia is also a space astrometry mission created by ESA. It launched in 2013 and is scheduled to end in 2025. Gaia's primary goal is to map over a billion stars in our

[3]The celestial sphere is a projection of the Earth surface on the sky. This sphere is used to locate stars via equatorial coordinate system as shown in Figure 4.1

galaxy in order to understand the origin and evolution of the Milky Way.[24]
Thus the computation of the proper motion anomaly is such as:

$$\Delta\mu_{\mathrm{H/G2}} = \mu_{\mathrm{H/G2}} - \mu_{\mathrm{HG}} \tag{2.2}$$

where $\Delta\mu_{\mathrm{H/G2}}$ is the PMa measured with Hipparcos or GDR2, $\mu_{\mathrm{H/G2}}$ is the short-term PM vector from Hipparcos or GDR2 and μ_{HG} is the long-term PM vector resulting from the combination of the two catalogs.
As shown in Figure 2.3, the motion of the barycenter G, depicted by the vector μ_{HG}, is rectilinear and uniform while the motion of the photocenter A seems to follow a virtual orbit around the barycenter. By comparing the difference between the long-term barycenter motion and the instantaneous motion of the photocenter relative to the center of mass, the projected motion of the photocenter around the barycenter can be derived.

In order to retrieve the long-term PM vector that covers the Hipparcos and GDR2 data, both datasets are combined. However, as the two datasets correspond to different epochs, the light travel time effect must be taken into account.

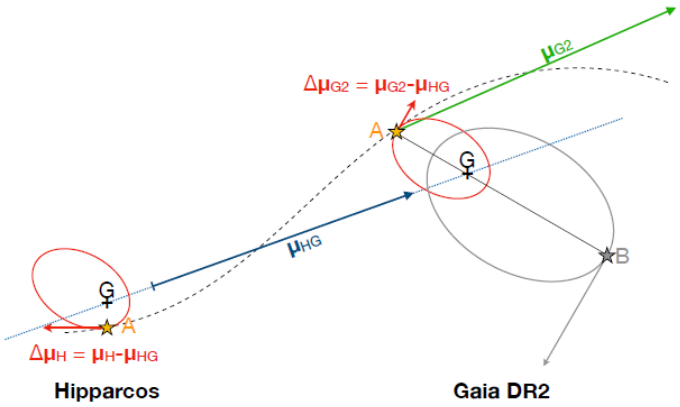

FIGURE 2.3: Principle of the determination of the proper motion anomaly $\Delta\mu_H$ (at Hipparcos epoch) and $\Delta\mu_{G2}$ (at Gaia epoch). μ_{HG} is the long term proper motion determined from the Hipparcos and Gaia positions. It is considered here the case of a companion with a negligible photometric contribution compared to the primary.[27]

The astrometry detection strategy is often coupled with the radial velocity technique due to its complementarity. Astrometry is well suited for the observations of face-on orbit while, the Doppler spectroscopy is more appropriate to edge-on orbit. Moreover, astrometric data are able to accurately estimate the companion's mass whereas the radial velocity technique only provides a lower limit. Besides, this technique is less sensitive to stellar activity in comparison to the RV method, hence it can detect young and old exoplanets. Despite these strengths, this method requires instruments with high degree of precision that is its major limitation.[38]

3 High contrast Angular Differential Imaging method

As mentioned before, HD18757 was observed with the LMIRCam camera mounted on the Large Binocular Telescope. From these observations, an ADI cube with a dimension of (9349, 399, 399) and two PSF of 399×399 pixels are obtained. The two PSF correspond to evaluations before and after the scientific observation and are non-saturated. The double measure of the PSF allows to assess the variability in the observations' condition of the scientific images. Since in practice observing a stellar object takes time, it is important to ensure that the observation conditions remain fairly stable during the monitoring. Regarding their non-saturation, it provides the photometric information of the host star as this data is missing in the scientific images. Scientific observations are performed with a coronagraph that masks the parent star due to faint close-in companions and hence suppress its photometry.
The images which are thus saturated and the PSF that are non-saturated, have both different integration time, meaning that the received information must be normalized. The scientific images have an exposition time of 0.8104 sec while the PSF are measured over a period of 0.0824 sec. Therefore the two PSF are normalized following:

$$PSF_{norm} = \frac{0.8104}{0.0824} \times PSF \tag{3.1}$$

Moreover, a Gaussian fit is performed on the two point-spread functions, as seen in Figure 3.2, in order to retrieve the full width at half maximum (FWHM). This parameter represents the wideness of the PSF Gaussian curve at $f_{max/2}$ as shown in Figure 3.1 and characterizes the images' spatial resolution.

$FWHM_{x1} = 9.803$ px $\quad FWHM_{y1} = 8.844$ px
$FWHM_{x2} = 9.899$ px $\quad FWHM_{y2} = 8.785$ px

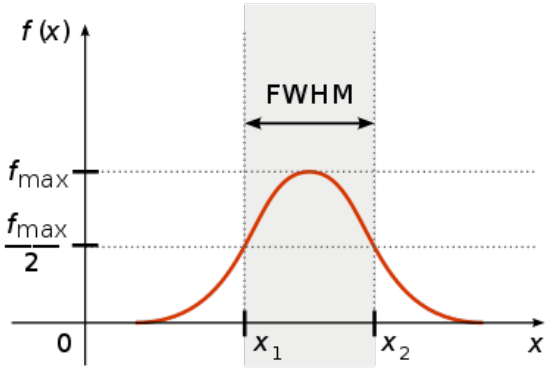

FIGURE 3.1: Full Width at Half Maximum of a Gaussian.[39]

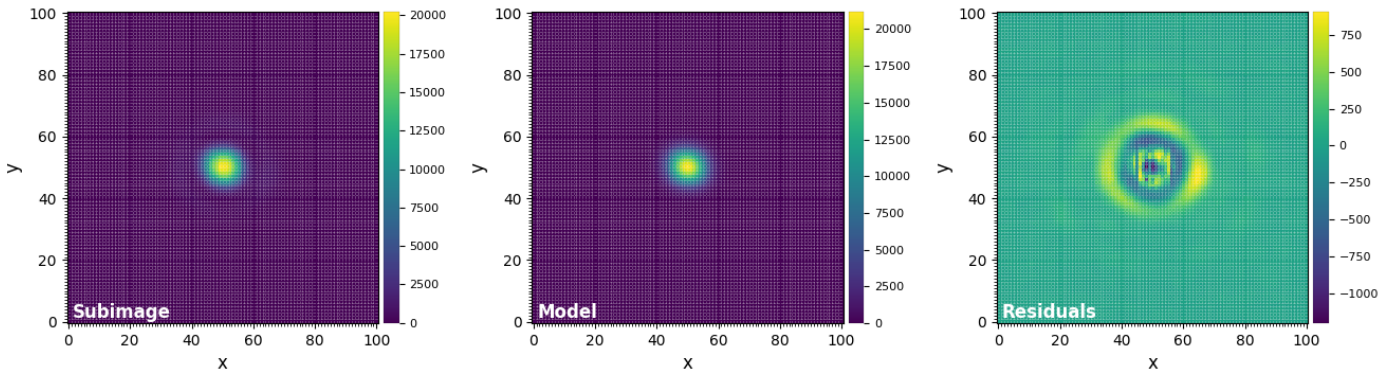

FIGURE 3.2: Sub-image is the PSF from the dataset, model is the 2D Gaussian model computed and the residuals is the difference between the original PSF and the 2D Gaussian model.

In the frame of this project, the Vortex Imaging Processing (VIP) python package is used for the pre- and post-processing on the ADI dataset derived from HD18757 observations. The main advantage of VIP is that it is an open source code that combines several exoplanet data processing tools. Therefore, the code is appropriate for several techniques and can be used to assess these detection techniques in the same environment.[5]

3.1 Pre-processing

As already introduced, the pre-processing step consists of several operations that decrease the cube's size by compacting the information and discarding bad frames. In this analysis, the cube is first cropped to a frame size of 207 pixels and then undergoes a pixel binning which reduces the size to 104 pixels. This new size is determined in terms of the total semi-major axis between the host star brown dwarf companion assumed to 0.9 arcsec. The latter represents the angular separation between the host star and the searched companion, thus imposing the field of view of one frame to cover at least twice 0.9 arcsec. This value is converted in pixels via:

$$\begin{aligned} & platescale \times binning \times pixels_{nbr} \geq 2a_{tot} \\ \iff & pixels_{nbr} \geq \frac{2a_{tot}}{platescale \times binning} \\ \iff & pixels_{nbr} \geq \frac{2 \times 0.9}{10.707 \times 10^{-3} \times 2} \\ \iff & pixels_{nbr} \geq 84 \text{ pixels} \end{aligned} \tag{3.2}$$

Where the plate scale gives the angular separation per pixels, more precisely it represents the size of the field covered in one pixel. The binning is a coefficient standing for the amount of pixels merged into one and a_{tot} is the total semi-major axis of the host star-companion system.
In order to be sure that the companion is included in the frame, an angular separation of 1.1 arcsec is assumed which leads to a frame size of 104 pixels accounting the binning.

From Figure 3.3, it is observed that the initial scientific images are oversampled, thus allowing the pixel binning without smearing the companion's signal. The Nyquist Sampling theorem states that '*the sampling must be at least twice the highest spatial frequency component in the image*'.[40] The spatial frequency is related to the FWHM such as the criterion is adapted to 'FWHM must be greater than at least twice the pixel size'.[41] That is, the sampling or the number of pixels in the frame must be greater or equal to two pixels across resolution limit:

$$2 \text{ pixel} \leq FWHM \tag{3.3}$$

Since the FWHM computed is high and equals to 9.342 in pixels, the criterion is respected and a binning of a factor two maintains an acceptable spatial resolution.

After reducing the cube in the x and y directions, it is also possible to decrease it along the third direction by removing bad frames and sampling it temporally. Bad frames are discarded if their correlation is below a threshold which is computed with respect to a reference frame. Regarding the down sampling, it is done by combining every 15 frames into one. This choice results from a trade-off between the size reduction of the cube and the quality of the modeled PSF. The last operation of the pre-processing is to remove bad pixels by merging them with their neighbours.

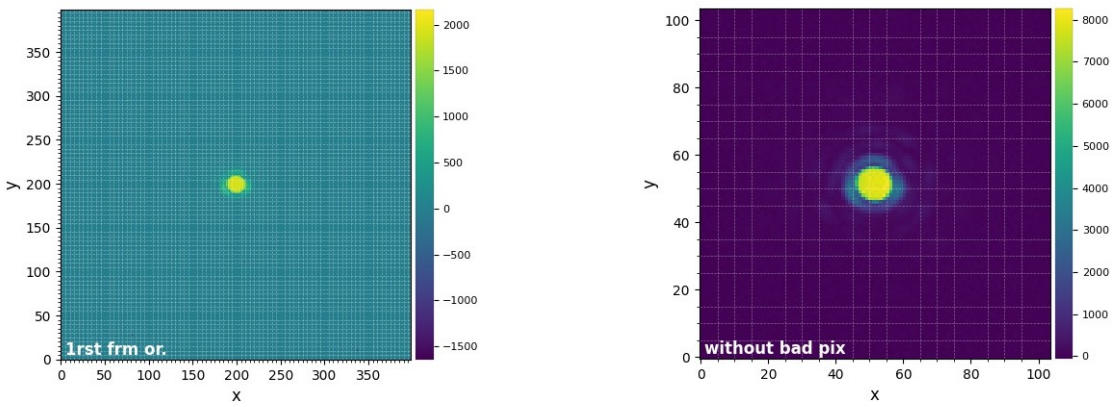

FIGURE 3.3: First raw frame of the ADI cube (not pre-processed), on the left and the first frame of the ADI cube after the pre-processing, on the right.

At the end of the pre-processing, the cube dimensions are (529,104,104).

3.2 Post-processing

This reduced cube is used for the post-processing part which consists in subtracting the PSF, computing the contrast curves and detecting the companion.
Three different algorithms are used for modelling and subtracting the post-coronagraphic star PSF from the frames: the median reference PSF subtraction, the full-frame ADI-PCA and the pairwise frame differencing. These algorithms are chosen because they have low computation time and display good performances. Figure 3.4 shows the three algorithms' outputs with their corresponding signal-to-noise ratio maps. Signal-to-noise ratio (SNR) maps are assessing the signal-to-noise ratio on each pixel, that is comparing the level of the desired planet signal over the background noise:

$$S/N \equiv \frac{\mu_{planet}}{\sigma_{noise}} \tag{3.4}$$

Where μ_{planet} is the pixels' values of the planet and σ_{noise} is the noise computed as the standard deviation of the pixels in an annulus of FWHM diameter, at the same radial distance from the center of the frame.[5]

From Figure 3.4, it is seen that these post-processing final frames do not share a same pattern and do not highlight a companion at first sight. Typically, if a companion had been detected, then we would had seen common spots among the three post-processed images.

To detect potential companions on the post-processing final frames, a detection algorithm from VIP is run with several modes. The detection algorithm swaps the frames in search of regions in the images that share a constant property or with a property varying in a specific range. These regions are called blobs and can be found through several techniques or modes. The use of several modes allows to verify the result by reinforcing it when the same blob is found by all.
The first mode is known as 'lpeaks' and is based on the search of local peaks above the background noise. The second one is called 'log' and consists in finding local maxima in the Laplacian of Gaussian images. And the last mode used is 'snrmap' which evaluates peaks above a threshold given by the SNR maps.[5]
By running the detection algorithm with these modes, no companions are detected.

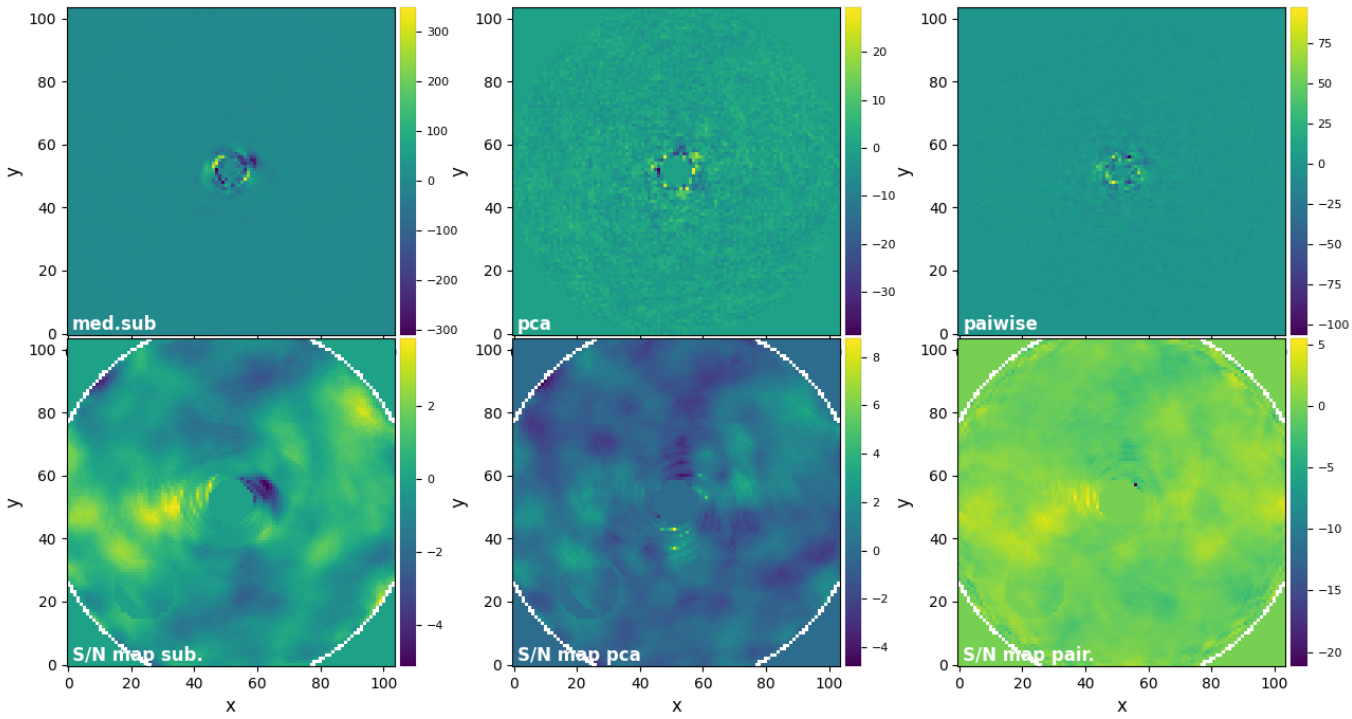

FIGURE 3.4: Angular Differential Imaging model PSF subtraction techniques with their signal-to-noise ratio map. Med stands for median reference PSF subtraction, pca refers to the full-frame ADI-PCA and pair. represents the Pairwise frame differencing method.

To understand this non-detection, contrast curves are computed from the post-processing final frames. Figure 3.5 depicts the 5-σ contrast in terms of the angular separation between the companion and the host star, where 5-σ implies that the signal's level is 5 times higher than the background noise. From the figures, it can be seen that for angular separations higher than 0.5 arcsec, the contrast is of the order of 10^{-3} which is low.
Moreover, it is seen that the contrast curve decreases slightly until 0.35 arcsec then flattens around 10^{-3} for higher angular separations. This overall tendency highlights the fact that speckles' noise dominates close to the star and is attenuated for higher angular separation. Whereas further from the star, the contrast is limited due to the thermal background.
In practice, these curves impose a limit above which the companion can be found and since no companion is detected, it is deduced that its contrast is lower than 10^{-3}.

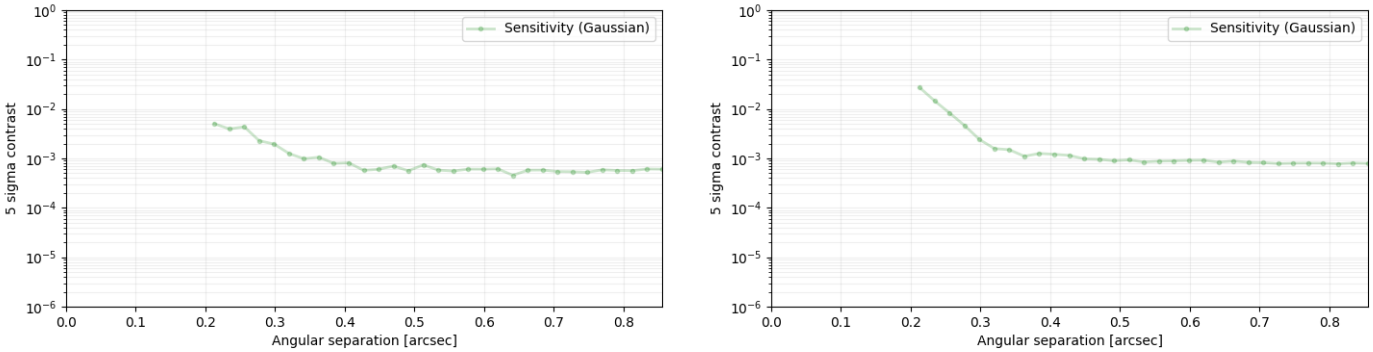

FIGURE 3.5: 5-σ contrast curve from the post-processing frames obtained with the median reference PSF subtraction and the full-frame ADI-PCA.

To verify this result and the contrast computed via VIP, a theoretical contrast is evaluated via:

$$\begin{aligned} d &= \frac{1}{\pi} \\ &= \frac{1}{42.39 \times 10^{-3}} \\ &= 23.586 \text{ pc} \end{aligned} \tag{3.5}$$

$$\begin{aligned} M_{star} &= m_{star} - 5\log_{10}(d) + 5 \\ &= 4.967 - 5\log_{10}(23.586) + 5 \\ &= 3.104 \end{aligned} \tag{3.6}$$

$$\begin{aligned} \Delta M &= M_{comp} - M_{star} \\ &= 16.04 - 3.104 \\ &= 12.936 \end{aligned} \tag{3.7}$$

$$\begin{aligned} contrast &= 10^{\frac{-\Delta_M}{2.5}} \\ &= 10^{\frac{-12.936}{2.5}} \\ &= 10^{-6} \end{aligned} \tag{3.8}$$

Where d is the distance in pc of the star HD18757, M_{star} is the absolute magnitude and m_{star} is the apparent magnitude of the star. The absolute magnitude is obtained from the evolutionary model of *Baraffe et al. 2003* for a mass of 0.03 M_{sun} and an age of 10 Gyr. The apparent magnitude represents

the brightness of an object and depends on the distance. Therefore, it is preferable to work with absolute magnitudes which are the apparent magnitudes the stars would have at 10 pc.
The apparent magnitude is interpolated from the magnitudes obtained with WISE, through the VizieR photometry viewer hosted by CDS, in order to have the apparent magnitude at the observing wavelength of 3.8 µm which corresponds to the L' band.[42]

From this computation, the contrast obtained is of the order of 10^{-6} which is indeed lower than the contrast curve from VIP. Therefore, this theoretical contrast confirms the hypothesis that the companion has a low contrast and is situated below the detection limit imposed by VIP, which explains its non-detection.

In addition to the theoretical contrast verification, it is interesting to test the efficiency of the detection algorithm from VIP. This verification is performed by injecting fake companions at different contrast level and checking whether they are detected or not.

A fake companion is injected around the star at 25 pixels from its center at different contrast levels. This position corresponds to an angular separation of 0.5 arcsec and thus predicts a similar contrast of 10^{-3}, confer to Figure 3.5. Regarding its contrast and position, it is reasonable to analyse the detection performance and compare them to HD18757B.
Figure 3.6 depicts the experience with the first row presenting the companions with a contrast of 10^{-4}, the second row exhibiting the companions at a contrast of 10^{-3} and the last row being the companions at a contrast of 10^{-2}. By looking carefully, companions with high contrasts can be spotted visually. As the contrast decreases, the companion becomes fainter and is overcome by the background.

By running the different modes of the detection algorithm explained earlier, it appears that some modes detect the fake companion. As a matter of fact, companions with a contrast of 10^{-2} and 10^{-3} are found via 'lpeaks' and 'snrmaps' for the post-processing images obtained with ADI-PCA and the classical approach. For companions at a level of 10^{-4}, only the 'snrmap' mode detect the object on the ADI-PCA image. This analysis highlights the fact that objects with a contrast lower than 10^{-4} are not expected to be found via this detection algorithm. Since HD18757B has a theoretical contrast of 10^{-6}, it cannot be detected by the algorithm.

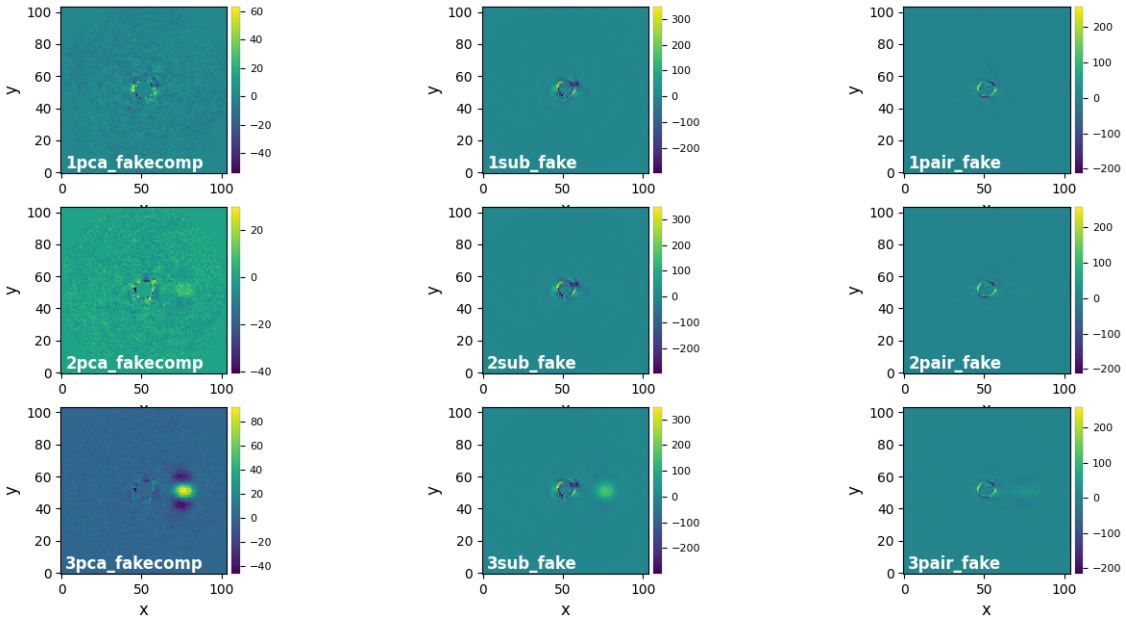

FIGURE 3.6: Post-processing final frames with a fake companion injected at different contrast level from top to bottom: first row for 10^{-4}, second row for 10^{-3} and third row for 10^{-2}. The PSF subtraction is done via the full-frame ADI-PCA, the median reference PSF subtraction and the Pairwise frame differencing method.

3.3 Algorithm verification with extra dataset

Since no companion is detected, it is interesting to verify the entire VIP methodology described in the previous section. To proceed in this way, a new dataset from LMIRCam composed of an ADI cube with a dimension of (200,200,3219), one PSF of (31,31) and the parallactic angles is loaded and analysed. This dataset is coming from the Exoplanet Imaging Data Challenge where several fake companions were injected and were processed via several detection algorithms in order to assess their performances.[6] Therefore, the results and potential fake companions are known in advance which allows to verify the VIP methodology. This ADI cube is already pre-processed, only a temporal binning is applied which reduces the number of frames to 321. The down-sampling allows to decrease the computation time while preserving enough information to model the PSF.

It is assumed that the PSF and the scientific images are already normalized, thus they have the same integration time. The point spread function and the first frame of the ADI cube are displayed in Figure 3.7. From this PSF, it is possible to compute the FWHM in the x and y direction by applying a 2D Gaussian fit which outputs:

$$FWHM_x = 4.373 \text{ px} \qquad FWHM_y = 4.282 \text{ px}$$

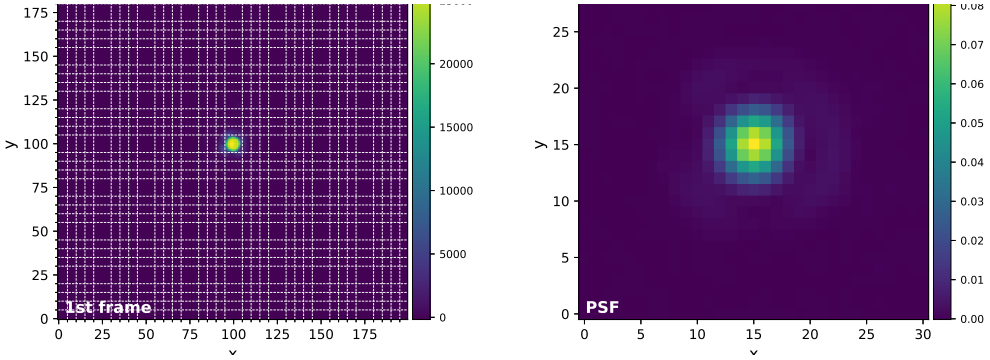

FIGURE 3.7: First frame of the ADI cube from LMIRCam and the non-saturated point spread function.

The noise attenuation on the cube is performed with the classical median subtraction and the ADI-PCA algorithms. The PCA method is run with 10 PCs in order to maximize noise reduction while preserving the companion's signal.
Moreover, contrast curves are computed from the post-processed images and are shown in Figure 3.8. It is seen that contrast is decreasing with larger angular separations implying that the companion is easier to spot when it is further away from the parent star. An object in the vicinity of a star that is much brighter and bigger is difficult to detect due to the large contrast and luminosity difference between them.

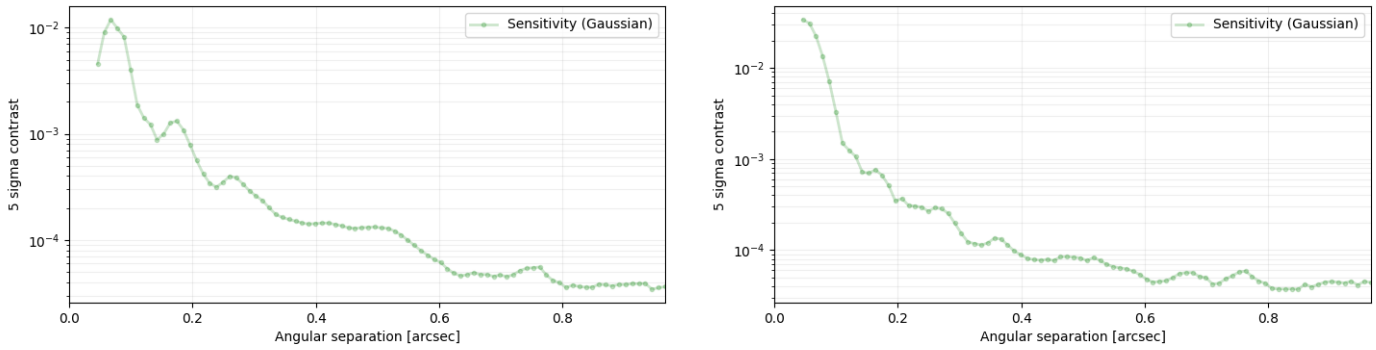

FIGURE 3.8: 5-σ contrast curve from the post-processing frames obtained with the median reference PSF subtraction and the full-frame ADI-PCA.

With the post-processed images that are noise attenuated, derotated and combined as the median of the stack, it is possible to apply detection algorithms to search for blobs. In this analysis, three blobs detection methods are used: 'lpeaks', 'log' and 'snrmap' on both the median subtraction and ADI-PCA post-processed frames. Modes 'lpeaks' and 'log' are set differently for the post-processed median subtraction and ADI-PCA frames. More precisely, the background noise, which imposes the level of noise above which a companion can be detected, is set to 1 for the median subtraction and to 3 for ADI-PCA. This setting difference is due to the high performance of ADI-PCA which allows to better screen the blobs on the post-processed ADI-PCA frame. The results of the detection algorithms are summarized in Figure 3.9.

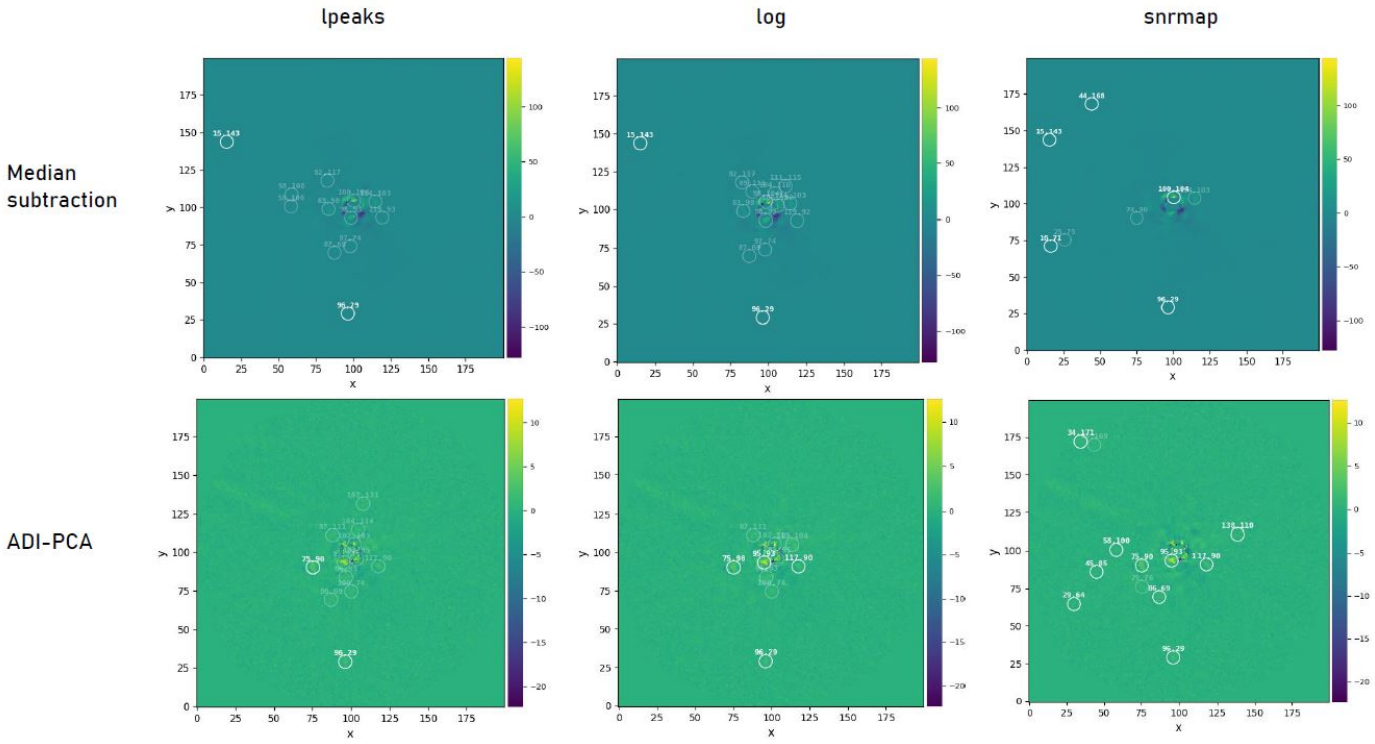

FIGURE 3.9: Post-processed frames with median subtraction and ADI-PCA algorithms where blobs found via 'lpeaks', 'log' and 'snrmap' modes are highlighted with white circles.

The results of this analysis show that detection algorithms implemented in the VIP library are efficient. By comparing the blobs discovered with VIP's methodology and the ones from the data challenge, it is evident that some match. In particular, blobs situated in (96,29) and (117,90) are found with each mode on both post-processed frames and correspond to the fake companions, as shown in Figure 3.10.
These coordinates correspond to an angular separation of:

$$\begin{aligned} d_{star/companion} &= \sqrt{(x_{star} - x_{companion})^2 + (y_{star} - y_{companion})^2} \\ &= 71 \text{ pixels } \& \text{ } 19 \text{ pixels} \end{aligned} \tag{3.9}$$

$$\begin{aligned} a &= \frac{platescale \times binning \times pixels_{nbr}}{2} \\ &= 0.76 \text{ arcsec } \& \text{ } 0.211 \text{ arcsec} \end{aligned} \tag{3.10}$$

By comparing the contrast predicted at these angular separations, it is obvious from Figure 3.8 that the companion at 0.211 arcsec has a contrast of at least 10^{-3}, whereas the one at 0.76 arcsec has a minimal contrast of 10^{-4}. Since both companion are detected, it is inferred that their contrasts are higher.

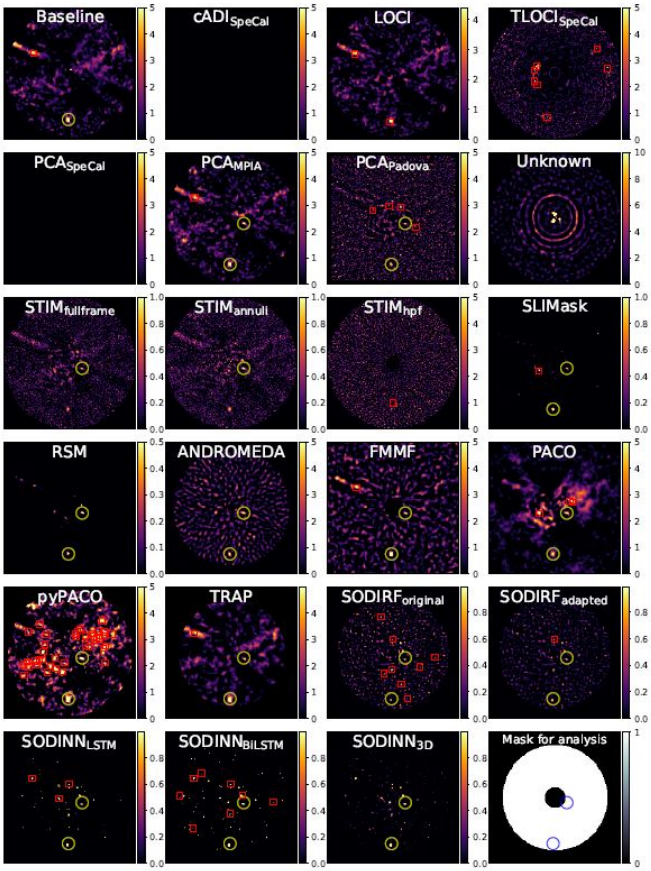

FIGURE 3.10: Results of the ADI subchallenge for the second LBT/LMIRCam dataset (lmr2).[6]

4 Markov-Chain Monte Carlo method

The Markov-Chain Monte Carlo (MCMC) is a method to fit a set of parameters on data. More precisely, the parameters are used to build models that are compared to data. A model can be seen as a walker defined by a specific combination of parameters. Each walker explores the parameter space within the allowed range defined by the priors, and generates a new model for that step. The models are then compared to data and the ones with the highest likelihood are kept. This process outputs a posterior distribution of the best-fitted models from which samples are drawn.[43]

4.1 Initialization

For this analysis, the parameters' set is composed of the dynamical masses of the companion and the host star, the astrometric data and the information derived from the radial velocity technique. The Markov-Chain Monte Carlo algorithm is implemented and referenced in *Maire et al. 2020.*
More particularly, the astrometry is defined by:

- The period P of the companion's orbit.
- The eccentricity e which characterizes the shape of the companion's orbit.
- The inclination i that indicates the orientation of the orbit with respect to the line of sight between the observer and the star.
- The longitude of the ascending node Ω pictured in Figure 4.1.
- The argument of periastron ω illustrated in Figure 4.1.
- The time of periastron passage T_0 which is the time of closest approach to the host star.
- The offset in the right ascension between the model and the proper motion measured by Gaia/Hipparcos.
- The offset in the declination between the model and the proper motion measured by Gaia/Hipparcos.
- The parallax from the second Gaia data release.

The radial velocity is represented by:

- The Semi-amplitude κ of the radial velocity sine curve.
- The instrumental offset between Sophie and Elodie. Because the dataset of radial velocities is obtained with two different instruments, the data must be calibrated.
- The jitter on Elodie σ_{RV1} which accounts for stellar activities effects.
- The jitter on Sophie σ_{RV2} which accounts for stellar activities effects.
- The systemic velocity that accounts for the stellar proper velocity which cannot systematically be measured by the instrument.

Parameters	Unit	Symbol
Orbital period	[yr]	P
Inclination	[°]	i
Longitude of ascending node	[°]	Ω
Argument of periastron	[°]	ω
Eccentricity	[-]	e
Time of periastron - 2 450 000	[days]	T_0
astrometric semi-major axis	[mas]	a_1
Total semi-major axis	[mas]	a
Semi-amplitude	[m/s]	κ
systemic velocity	[m/s]	v_0
Host-star mass	[Ms]	M_1
Companion mass	[Mj]	M_2
Instrumental offset	[m/s]	Δ_{RV}
Jitter 1	[m/s]	σ_{RV1}
Jitter 2	[m/s]	σ_{RV2}
parallax	[mas]	π
Right ascension	[mas/yr]	$\Delta_{\mu_{RA}}$
Declination	[mas/yr]	$\Delta_{\mu_{DEC}}$

TABLE 4.1: Parameters mentioned in the analysis with their corresponding symbols and units.

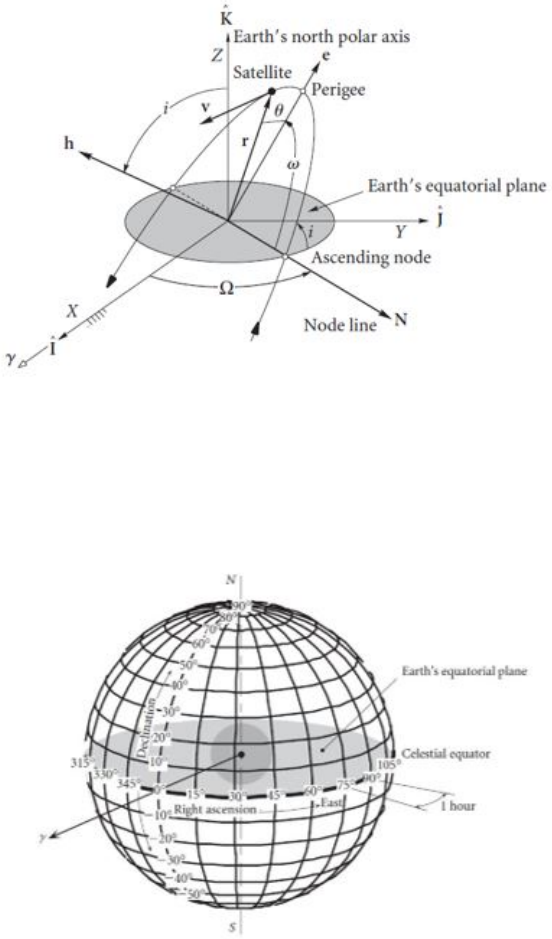

FIGURE 4.1: Orbital parameters and the geocentric right ascension-declination frame.[44]

To summarize, the Markov-Chain Monte Carlo is run for 100 walkers to sample a 16-parameter model over 3×10^4 steps. The initial guesses with their error width are displayed in Table 4.2.[7]

Initial guesses				Width
P	[yr]	109	(logP)	18
e	[-]	0.943	$\sqrt{e}\sin\omega$	0.01
			$\sqrt{e}\cos\omega$	0.01
i	[°]	75	$\log(\sin i)$	10.0
Ω	[°]	205		10.0
ω	[°]	44°		
T_0	[BJD]	2 455 220		0.8
κ	[m/s]	665.8		5.9
V_0	[m/s]	-245		10.0
π	[mas]	42.39		0.305
M1	[M_{sun}]	0.88Ms	A1 = M1+M2	0.060828
M2	[M_{sun}]	0.045Ms		0.02
Δ_{RV}	[m/s]	120		9.5
σ_{RV1}	[m/s]	1.4	$\log(\sigma_{RV1})$	0.5
σ_{RV2}	[m/s]	2.7	$\log(\sigma_{RV2})$	0.5
$\Delta\mu_{RA}$	[mas/yr]	0		0
$\Delta\mu_{DEC}$	[mas/yr]	0		0

TABLE 4.2: Initial guesses and the width of interval of uncertainty for the Markov chain Monte-Carlo.

Together with the width and the initial values, priors are set for each parameter in order to impose the allowed range within which parameters can vary. More particularly, log-flat priors are assumed on the period, the jitters' parameter, the $\sin i$ and on the companion's mass, Gaussian priors are used for the parallax and the total mass companion-star and uniform priors are set for the rest of the parameters.
For instance, log-flat priors are computed following the described computation for:

- The period

$$\begin{aligned} &\log P + \log P - \log\left(P - width\right) \longrightarrow \frac{P^2}{P - width} = 130.5 \text{ yr} = 47632 \text{ days} \\ &\log P - \log P + \log\left(P - width\right) \longrightarrow P - width = 91 \text{ yr} = 33215 \text{ days} \end{aligned} \tag{4.1}$$

  It results in $P = 109^{+21.5}_{-18}$ yr.

- The inclination

$$\begin{aligned} &\log\sin i + |\log\sin i - \log\left(\sin 180 - i - width\right)| \longrightarrow \arcsin\frac{\sin i^2}{\sin 180 - i - width} = 67.1° \\ &\log\sin i - |\log\sin i + \log\left(\sin 180 - i - width\right)| \longrightarrow \arcsin|\sin\left(180 - i - width\right)| = 97° \end{aligned} \tag{4.2}$$

  Parameter i is initialized to $73^{+25}_{-5.8}$ °

- The jitters are set to $\sigma_{RV1} = 1.4^{+0.86}_{-0.5}$ m/s and $\sigma_{RV2} = 2.7^{+0.77}_{-0.5}$ m/s.

By taking into account the widths on the guesses represented by *width* and the corresponding priors, the initial values for the Markov Chain Monte-Carlo are:

	$\log P$	$\sqrt{e}\sin\omega$	$\sqrt{e}\cos\omega$	$\log(\sin i)$	Ω	T0	κ	V0	π	A1	M2	Δ_{RV}	$\log(\sigma_{RV1})$	$\log(\sigma_{RV1})$	$\Delta\mu_{RA}$	$\Delta\mu_{DEC}$
	38 520	0.702	0.666	80.755	202.437	2.45e6	669.696	-241.835	42.4	0.869	0	122.493	1.210	3.277	0	0

TABLE 4.3: Parameters' initial values for the chain of the MCMC. Note that the P value, in this table, is given in days.

4.2 Analysis

The Markov-Chain Monte Carlo algorithm outputs two characteristic graphs called the Chain plot and the Corner plot. These two graphs bring additional information about the method's convergence and the parameter space covered.

Chain plots, also called Walk plots, represent the posterior distribution of the parameters' set for a number of steps, in this case 30 000 iterations. In practice, it shows the walkers' path over the parameter space. Figure 4.2 illustrates that all chains are smooth and vary within a specific interval. These smooth patterns indicate that parameters' values have stabilized around a global minimum in the parameters' space. By contrast, a Walk plot with noisy patterns would reveal the non-convergence of the Markov-Chain Monte Carlo method, since the graphs are smooth, the non-convergence is not verified.

Along with the graph's smoothness, convergence can be assessed with the study of the integrated autocorrelation time.[45] This parameter characterizes the dependence among the samples as it is related to the variance. In other words, it represents the number of steps required to obtain two consecutive independent samples. On that account, a small integrated autocorrelation time denotes a fast convergence of the MCMC and a low dependence between the samples. Whereas a bigger integrated autocorrelation time defines a non-converged MCMC with correlated chains.[46]
Table 4.4 gathers the maximal autocorrelation time of the 13 fitted parameters and shows that values vary approximately within [13,49].

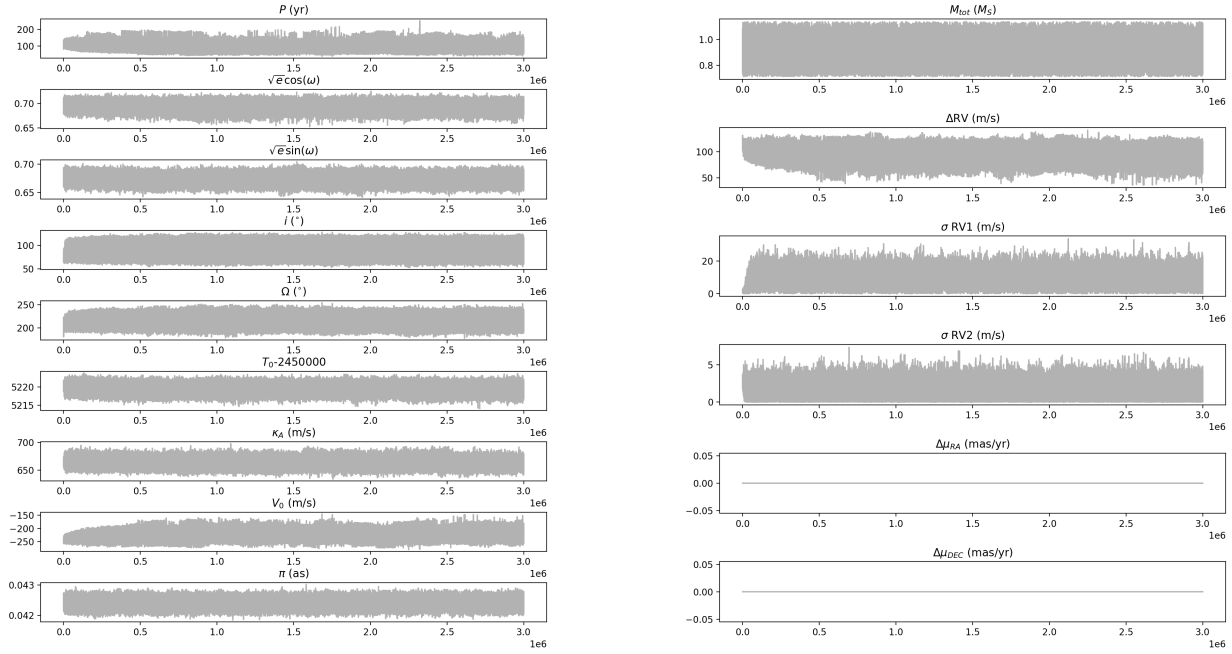

FIGURE 4.2: Chain plot derived from the posterior distribution of the fitted parameters via the Markov-Chain Monte Carlo method[4]

Corner plots provide information about the spread between the fitted parameters. These graphs are computed from the MCMC posterior distributions that have been trimmed and burned-in. The trimming process consists in keeping the information of the chain every n steps such as preserving the information while decreasing the chain size. This method is applied because consecutive steps in the chain are highly

[4]All plots are computed with the MCMC algorithm implemented by A.-L Maire, described in *Maire et al. 2020*

correlated, thus it does not introduce biaises.
The burn-in process is used to discard the first samples of the chain in order to start to collect the information at an equilibrium distribution.
In this analysis, a burn-in of 60% is applied and the chains are trimmed every 50 steps. These operations lead to 24000 orbits kept.

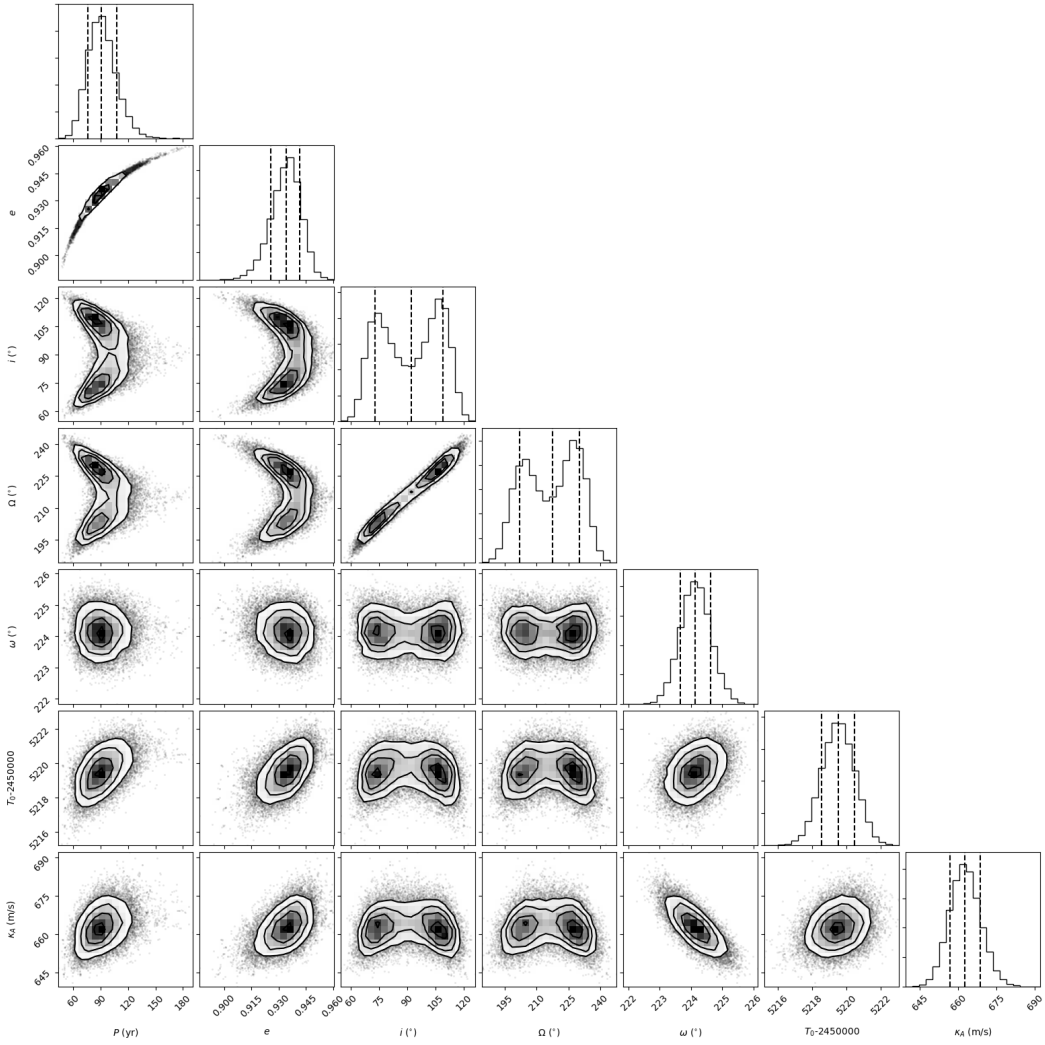

FIGURE 4.3: Corner plot of the first seven parameters used for the model.

From Figure 4.3, it is shown that the inclination and the longitude of the ascending node present two peaks. This phenomenon is due to the fact that the inclination is not constrained via radial velocity technique, nor with direct imaging method as the companion is not detected, neither with astrometric measurements which evaluations are far from the perigee. These two peaks correspond to inclinations 0 $\leq i_1 \leq 90°$ and $i_2 = 180°$ - i_1. The inclination i_1 leads to a prograde motion while companion with a i_2 inclination have a retrograde motion around the host star. This difference does not impact the mass determination of the companion given by Equation 2.1 where the factor $M_{planet} \sin i$ is unchanged considering that the sine of anti-additional angles is the same.

In addition to the indication on the orientation, an inclination of 0° represents a face-on orbit with respect to the line of sight between the observer and the star and an inclination of 90° is a edge-on orbit with respect to the line of sight. Since the companion's inclination for both orbit families is closer to 90° than 0°, it can be deduced that the orbit is strongly tilted such as being almost perpendicular to the line of sight.

Regarding the ambiguity on the longitude of ascending node, it is related to the two inclinations. In reality, the longitude of the ascending node is the angle laying in the reference plane at which the orbit crosses the reference plane, as depicted in Figure 4.1. Therefore the value difference in the two longitudes of ascending node corresponds to the angular difference in inclination between the two orbit family at the intersection with the reference plane.[47]

Regarding the other orbital parameters, they present a unique peak meaning that their value have stabilized around a local minimum. It is seen that the eccentricity is closer to one leading to a highly-eccentric orbit. Moreover, the orbital period is estimated around 90 yr which fits with the highly-eccentric solution, as these types of orbit display long period. Furthermore, the analysis shows that the time of closest approach is assessed to 5219 days where the companion's angular position is approximately of 224°. This time of closest approach or time of periastron passage matches the peak in the radial velocity graph exhibited in Figure 4.7. This observation is expected since the companion's radial velocity is the highest at its periastron. The peak's height is estimated to 662.45 m/s by the MCMC analysis and is similar to the one shown in Figure 4.7.

Parameters	Unit	Integrated Autocorrelation time
P	[yr]	44.951
i	[°]	23.044
Ω	[°]	22.897
$\sqrt{e}\sin\omega$	[-]	15.871
$\sqrt{e}\cos\omega$	[-]	18.387
T_0 - 2 450 000	[days]	17.734
κ	[m/s]	15.143
V_0	[m/s]	41.858
M_{tot}	[Ms]	13.59
Δ_{RV}	[m/s]	34.092
σ_{RV1}	[m/s]	49.281
σ_{RV2}	[m/s]	15.082
π	[mas]	13.332

TABLE 4.4: Integrated autocorrelation time of the fitted parameters.

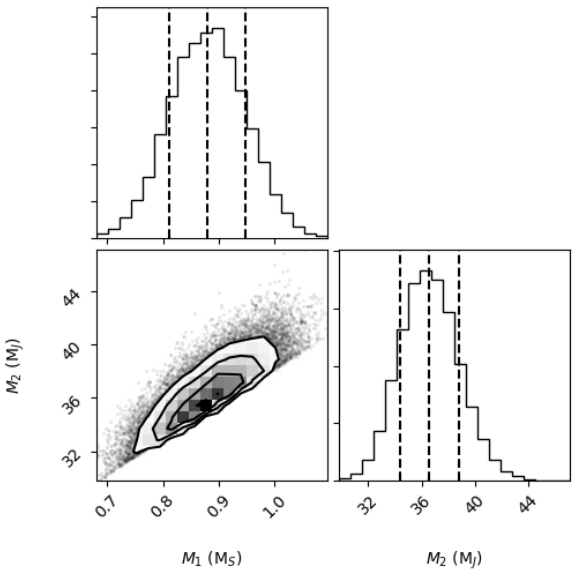

FIGURE 4.4: Corner plot depicting the companion's dynamical mass, in jovian mass M_{jup}, and the mass of the host star, in solar mass M_s.

For the dynamical masses of the host star and the companion, their estimation is displayed in Figure 4.4. The graph highlights that both masses are related and that the parameter space is bounded. The corner plot marks a lower threshold at which no samples are drawn. This threshold corresponds to the minimal mass derived with the radial velocity method and used as the initial condition in the MCMC. In particular, the posterior distribution of the companion's mass is close to the initial value derived with

the Doppler spectroscopy. Considering that this method is more appropriate to edge-on orbit than face-on ones, this result indicates that the companion's orbit is tilted. This observation is in agreement with the value's inclination found and discussed previously.

As for the parameters related to instruments Sophie and Elodie, their posterior distribution is displayed in Figure 4.5. It is seen that the jitters on Elodie are higher than the ones on Sophie, this is explained by the fact that the precision of the Sophie spectrograph is higher than the Elodie spectrograph.

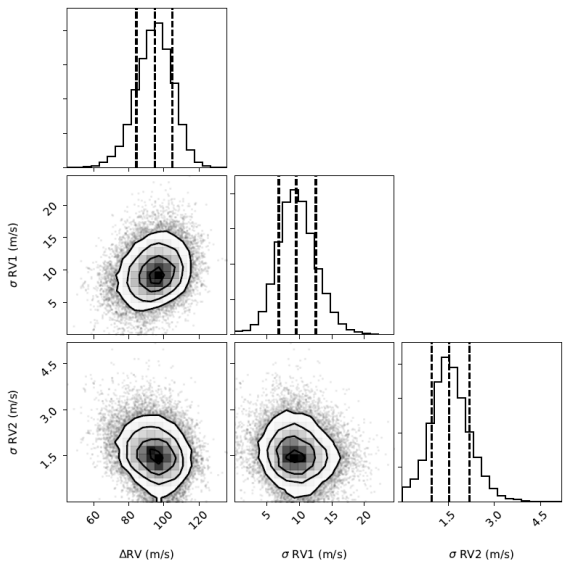

FIGURE 4.5: Corner plot of the jitters applied on instruments Sophie and Elodie and the offset between the two instruments.

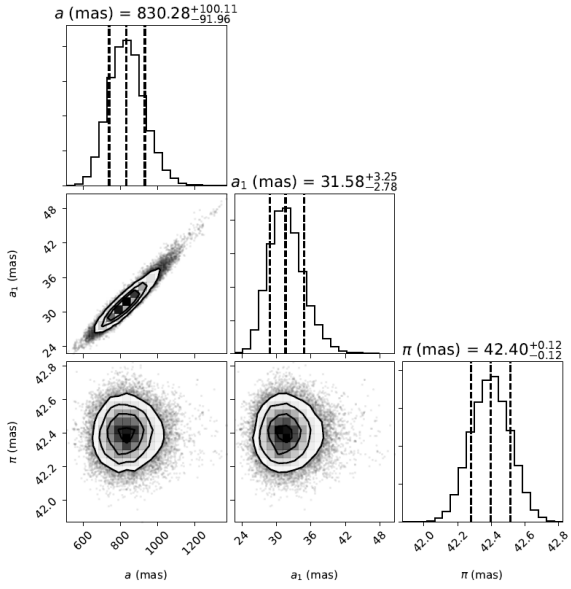

FIGURE 4.6: Corner plot on the fitted parallax, the computed astrometric semi-major axis and the total semi-major axis representing the star-companion system.

The MCMC analysis allows to determine the orbital parameters of the companion including the computation of the semi-major axis of the star-companion system. This component characterizes the distance between the star and the companion, and is used for making orbital predictions for direct imaging. In addition to the angular distance between the companion and the star, the astrometric semi-major axis is evaluated. The latter represents the distance between the star and the center of mass of the system. The barycenter of a system without a companion must match the photocenter as the total mass of the system is primarily due to the star. For a star with an orbiting companion, the barycenter shifts away because of the presence of a secondary body and thus leads to an astrometric semi-major axis non-null.
Moreover, these two parameters are related as seen from the posterior distribution displayed in Figure 4.6: as the semi-major axis increases, the astrometric semi-major axis grows too. This behaviour reveals that companions situated further away from their star, tend to move the barycenter further from their parent star.

The posterior distributions of the parameter's range for the Markov-chain Monte Carlo are summarized in Table 4.5.

Property	Median+/-1σ	68% confidence interval	Prior
Fitted parameters			
Orbital period P [yr]	$90.763^{+16.623}_{-14.469}$	75.887, 106.774	log-flat
Inclination i [°]	$75.89^{+8.468}_{-6.851}$	69.039, 84.358	log-flat $\sin(i)$
	$105.307^{+6.772}_{-8.837}$	96.469, 112.079	
PA of the ascending node Ω [°]	$204.604^{+6.878}_{-6.251}$	198.352, 211.482	uniform
	$227.179^{+5.762}_{-6.665}$	220.514, 232.942	
$\sqrt{e}\sin\omega$	$0.673^{+0.006}_{-0.006}$	0.667, 0.679	uniform
$\sqrt{e}\cos\omega$	$0.694^{+0.006}_{-0.007}$	0.687, 0.699	uniform
Time of periastron T0 - 2 450000[days]	$5219.505^{+0.964}_{-0.965}$	5218.507, 5220.429	uniform
Semi-amplitude κ [m/s]	$662.465^{+6.16}_{-5.86}$	656.529, 668.549	uniform
Systemic velocity V_0 [m/s]	$-226.648^{+13.047}_{-11.518}$	-238.166, -213.601	uniform
Instrumental offset Δ_{RV} [m/s]	$94.964^{+9.898}_{-10.667}$	84.296, 104.862	uniform
RV Jitter Elodie σ_{RV1}[m/s]	$9.501^{+3.018}_{-2.699}$	6.801, 12.519	log-flat
RV Jitter Sophie σ_{RV2}[m/s]	$1.541^{+0.646}_{-0.569}$	0.972, 2.187	log-flat
Parallax π [mas]	$42.399^{+0.117}_{-0.117}$	42.281, 42.516	gaussian
Host-star mass M_1 [M_s]	$0.881^{+0.068}_{-0.068}$	0.812, 0.949	gaussian M_1+M_2
Computed parameters			
Companion mass M_2 [M_{jup}]	$36.528^{+2.261}_{-2.134}$	34.393, 38.798	
Total semi-major axis a [mas]	$830.28^{+100.111}_{-91.96}$	738.319, 930.392	
Astrometric semi-major axis a_1 [mas]	$31.575^{+3.252}_{-2.777}$	28.798, 34.828	
Mass ratio M_2/M_1	$0.0395^{+0.002}_{-0.001}$	0.038, 0.041	
Eccentricity e	$0.931^{+0.0074}_{-0.0088}$	0.925, 0.941	
Argument of periastron ω [°]	$224.14^{+0.484}_{-0.485}$	223.659, 224.614	

TABLE 4.5: Orbital parameters of HD18757B from the Markov-chain Monte Carlo

As mentioned previously, the MCMC analysis is based on the radial velocity measurements coupled with data from the astrometric survey. These RV measurements are plotted in the following figures, along with Gaia and Hipparcos observations.

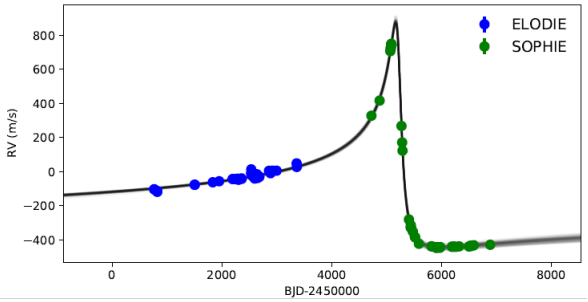

FIGURE 4.7: Dots are RV data gathered by Sophie and Elodie at different epochs. Lines represent the 50 orbits drawn from the posterior parameter distribution and are superimposed to display the highest likelihood orbit.

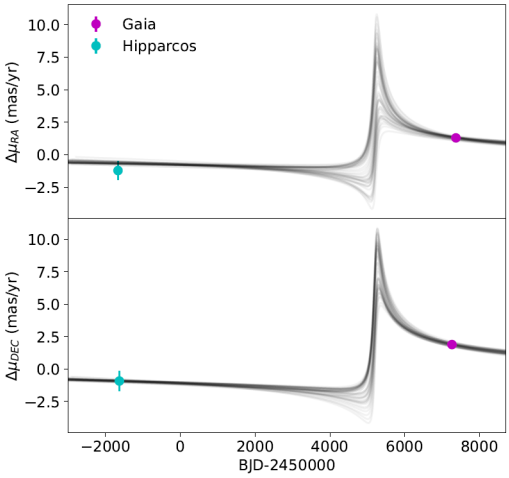

FIGURE 4.8: Dots are proper motion difference between Hipparcos, Gaia DR2 and Gaia-Hipparcos components: right ascension and declination

Figure 4.7 exhibits the radial velocity of the star at different epochs. From this sine pattern, it can be inferred that the host star is oscillating around the center of mass of the system due to the presence of a companion. This sine graph outlines a slight movement of the star which is periodic and is induced by a nearby companion. More particularly, the curve shape is affected by the companion's orbit eccentricity and mass. Since HD18757B is on a highly elliptical orbit, it is pretty close to the host star at perigee and much further away at apogee, thus resulting in a sharp sine curve.
More specifically, at perigee the companion being close to the star, has a stronger gravitational effect which induces a noticeable motion of the host star. This motion is described by the peak of 800 m/s around 5000 BJD-2 450 000. As the companion moves away, thus reducing its gravitational pull on the parent star, the star's radial velocity decreases abruptly.

Regarding the astrometric observations, they are displayed in Figure 4.8. This proper motion graph shows a similar behavior, to the RV graph, between 4000 and 6000 BJD-2 450 000. The peak in the proper motion graph indicates that the star is moving of approximately 3 mas per year.
By coupling the information from the RV and proper motion graph, it can be deduced that the star is undergoing a periodic displacement which is potentially due to a companion.

By looking at the proper motion shown in Figure 4.8, it is seen that the curves are indistinct. This phenomenon is caused by the overlapping of curves corresponding to both orbit solutions, prograde and retrograde. In order to improve the graph's readability, the proper motion for both orbit family is decoupled, as shown in Figures 4.9 and 4.10.
By separating the two solutions, it can be seen that their behaviour is different to one another. For orbits with an inclination smaller than 90°, the acceleration in the right ascension is first decreasing then increasing abruptly while the declination is continuously increasing. This tendency represents a prograde motion.
Regarding the second family, the acceleration in the declination is first decreasing then increasing while the ascension is continuously increasing. This behaviour is representative of a retrograde motion.

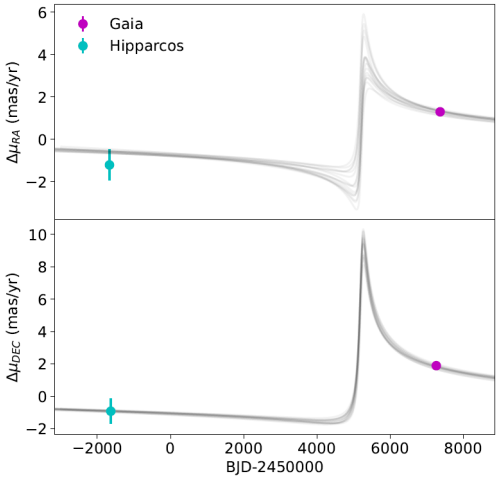

FIGURE 4.9: Acceleration of the star in the right ascension and declination for orbits with inclination smaller than 90°.

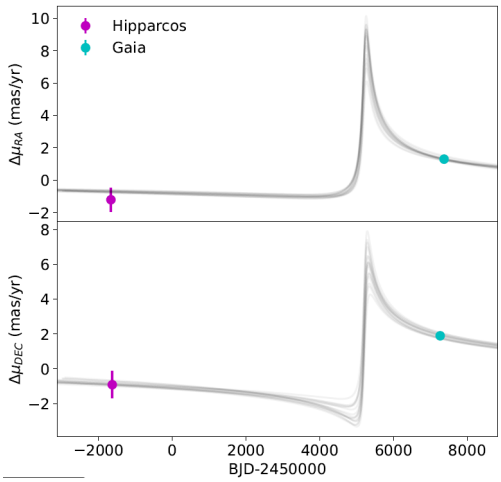

FIGURE 4.10: Acceleration of the star in the right ascension and declination for orbits with inclination greater than 90°.

In addition to the orbital parameters' predictions and the graphs of RV and astrometry, the MCMC simulation outputs predictions about the companion's orbit. These predictions correspond to what would have been measured by imaging, if the companion had been detected. Unfortunately, because the companion is not detected with data from LMIRCam, the following graphs forecast the companion's position at different epochs.

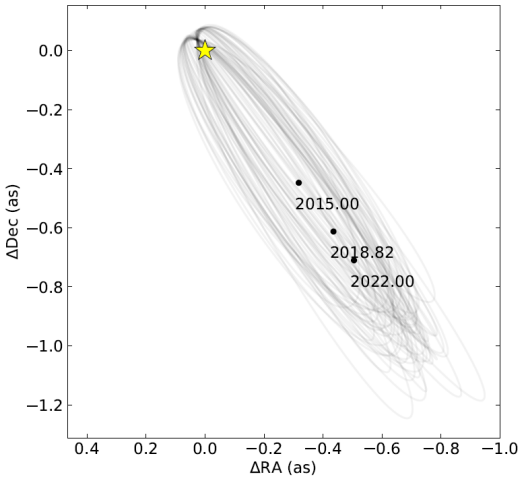

FIGURE 4.11: Computed orbits around the star projected onto the plane of the sky. Lines represent the 50 orbits drawn from the posterior parameter distribution and are superimposed to display the highest likelihood orbit. The host star is represent by '*' and the black dots show the past and future epochs along the orbit.

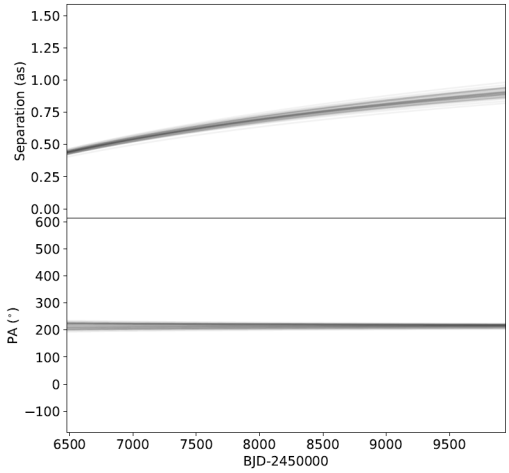

FIGURE 4.12: Separation angle and position angle of the companion relative to the parent star as a function of time.

Predictions about the companion's positions over several epochs are exhibited in Figure 4.11. This projected trajectory of the companion displays that orbits of the companion around the star are oriented

more edge-on than face-on with respect to the line of sight. This observation is in agreement with the fitted inclinations which have values closer to 90°, hence representing tilted orbits. By looking closer, it can be seen that once again, two types of orbit are displayed with two different inclinations, prograde and retrograde. This ambiguity is due to the fact that the inclination is not uniquely constrained because of the companion non-detection in angular imaging.

The two orbits family are also found in Figure 4.12, depicting the separation and position angles of the companion in terms of time. The evolution of the position angles is blurry due to the superposition of increasing and decreasing positions angles corresponding to the two types of orbits, prograde and retrograde orbits. The orbital type can be constrained with position angle measurements found by direct imaging. Such that if the companion is found by direct imaging, the separation with corresponding position angle of the companion will be given. Therefore, the behavior of the position angle, increasing or decreasing, selects the family of orbit, inclination greater or smaller than 90°.

Moreover, by separating the two families, it can be noticed that for orbits inclined with an angle smaller than 90°, the position angle of the companion is increasing. The opposite behavior is observed for companion on orbit with inclination greater than 90°.
This tendency is shown in Figure 4.13 and on Table 4.6 gathering position angles predicted at epoch (2015, 2018 and 2022) for both families.

Epoch	2457023.5	2458417.791	2459580.5
Family 1			
PA [°]	222.887	220.653	219.575
sep [mas]	542.297	743.550	867.497
Family 2			
PA [°]	547.583	748.869	869.893
sep [mas]	207.672	210.007	211.119

TABLE 4.6: Position (PA) and separation (sep) angles for Family 1,retrograde orbits and Family 2, prograde orbits at specific epochs.

These epochs are also marked as dots in Figure 4.11 and represent the positions of the companion in:

- 2015 $\longrightarrow$ BJD-2450000 = 7024
- 2018 $\longrightarrow$ BJD-2450000 = 8418
- 2022 $\longrightarrow$ BJD-2450000 = 9581

As already mentioned, these epochs correspond to predictions of the companion's position around the star. These predictions are used in direct imaging in order to observe the star at a specific epoch and position. The imaging data from LMIRCam of HD18757 was taken in 2018, equivalent to 8418 BJD. Table 4.6 shows that the angular separation at this epoch is predicted to 743.55 mas at which the contrast is limited by the thermal background. From the previous discussion in section 3, it was concluded that for such a separation, the contrast difference between the companion and the host is evaluated to 10^{-6}.

Furthermore, from Table 4.6 it is observed that angular separations are increasing, thus implying that the companion is currently moving away from the star. Those epochs correspond to the stabilization of the star's displacement after the RV peak.

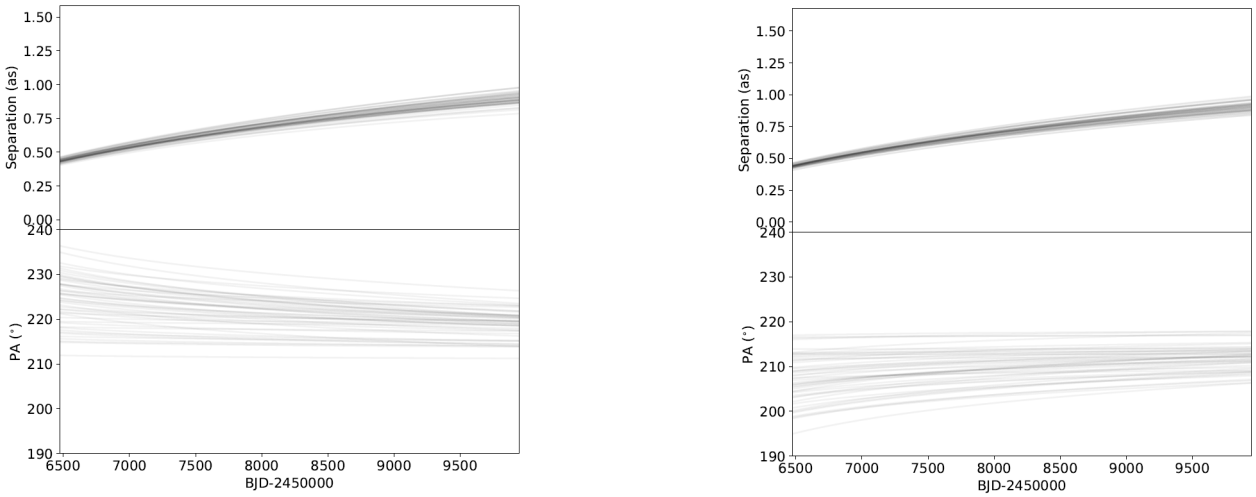

FIGURE 4.13: Separation and position angle for orbit having inclination greater and smaller than 90°.

The change in position angle is slow, approximately 3° over 7 years. Moreover, the astrometric data is covering epochs after the radial velocity peak, when the companion is shifting away from the star. As the companion is moving away at those epochs, the separation between the companion and the star is increasing until a maximum at the apogee. The evolution of the separation angle on the entire orbit must have a flatten bell-like curve due to the highly-elliptical orbit.

In the end, the MCMC simulation output a low mass object on a wide highly-elliptical orbit with an edge-on orientation with respect to the line of sight. Two sets of orbit are drawn from the computation, retrograde and prograde orbits due to the uncertainty on the inclination and the longitude of ascending node. The study predicts as well positions of the object at different epochs that are essential for the imaging observations.

4.3 Comparison with *Bouchy et al.*

Most of the parameters of the Markov-Chain Monte Carlo method are initialized with the values from *Bouchy et al.*, confer Table 4.2, hence it is interesting to analyse their deviations.

Table 4.7 gathers the orbital parameters of HD18757B from the MCMC analysis and from *Bouchy et al.* with their respective relative error. The relative error is computed such as:

$$RelativeError = \frac{|a-b|}{b} \times 100 \tag{4.3}$$

$$= \frac{|Bouchy - measured|}{measured} \times 100 \tag{4.4}$$

From the set of parameters, the majority present a low relative error except for the orbital period, jitters on Sophie and Elodie and the instrumental offset. The discrepancies on the period are due to the radial velocities' measures that cover only a fraction of the orbital phase, 17%.[2] Despite this low coverage, the orbital period is reasonably well bound as it is a highly eccentric orbit and astrometric data are combined as well.
Regarding the instrumental parameters, the jitters' terms can be more accurate with more radials velocities' measures on a shorter interval of time. In practice, with several radial velocities measurements, the stellar activity would be precisely determined and therefore the jitter terms would be valid. In particular, the jitters terms in our MCMC are set as free parameter and are thus optimized whereas they are estimated

empirically in *Bouchy et al.*.

Note that in Table 4.7, the companion's mass provided by *Bouchy et al.* represents a lower limit as it is the value derived from the radial velocity technique. Since the dynamical mass computed is close to the one of *Bouchy et al.*, it strengthens once again the hypothesis that the orbit is strongly tilted.

Property	Unit	HD18757B - MCMC	HD18757B - MCMC Bouchy et al.	Relative error on the mean value [%]
Orbital period P	[yr]	$90.763^{+16.623}_{-14.469}$	109^{+18}_{-16}	16.29
Time of periastron T0 - 2 450000	[days]	$5219.505^{+0.964}_{-0.965}$	$5220.0^{+0.8}_{-0.8}$	0.0095
Eccentricity e	[-]	$0.931^{+0.0074}_{-0.0088}$	$0.943^{+0.007}_{-0.007}$	1.44
Argument of periastron ω	[°]	$224.14^{+0.484}_{-0.485}$	$224^{+0.5}_{-0.4}$	0.0174
Total semi-major axis a	[mas]	$830.28^{+100.111}_{-91.96}$	917^{+103}_{-95}	10.32
Semi-amplitude κ	[m/s]	$662.465^{+6.16}_{-5.86}$	$665.8^{+5.9}_{-5.3}$	0.55
Host-star mass M_1	[Ms]	$0.881^{+0.068}_{-0.068}$	$0.88^{+0.06}_{-0.06}$	0.113
Companion mass M_2	[M_{jup}]	$36.528^{+2.261}_{-2.134}$	$35.2^{+1.2}_{-1.2}$	3.97
Instrumental offset Δ_{RV}	[m/s]	$94.964^{+9.898}_{-10.667}$	$120^{+9.5}_{-8}$	28.98
RV Jitter Elodie σ_{RV1}	[m/s]	$9.501^{+3.018}_{-2.699}$	1.4	85.74
RV Jitter Sophie σ_{RV2}	[m/s]	$1.541^{+0.646}_{-0.569}$	2.7	66.87

TABLE 4.7: Posterior parameters derived from our MCMC and the one from Bouchy et al. and the relative error on each parameter.

5 Evolutionary models

Evolutionary models are used to describe the properties of a substellar object or a planet. The properties consist in the effective temperature, the bolometric luminosity and the radius.
In this analysis, several models are used: The hybrid, cloudy and cloudless models from *Saumon et al. 2008* (SM08), the cloudless one from *Baraffe et al. 2003* (COND03), the cloudy one from *Chabrier et al. 2000* (DUSTY) and models from *Burrows et al. 1997* (BURR97).
These model predictions are compared and applied on the companion's data from *Bouchy et al.*.

5.1 Description

Models from Saumon 2008 assume adiabatic cooling of spherical, hydrostatic, nonmagnetic, nonrotating brown dwarf. These assumptions are valid for masses ranging in [0.0003,0.3] M_{sun}. The initial state is set to T_{eff}>4000 K and the surface boundary condition is chosen to match the interior entropy to the convective bottom of the atmosphere model, S(T_{eff}, g,[M/H],f_{sed}). The atmosphere model covers effective temperatures within $[500, 2400]$ K and includes a cloud model parameter f_{sed} that characterizes the efficiency of sedimentation of cloud particles. A higher sedimentation parameter represents optically thin clouds while a smaller sedimentation parameter expresses an atmosphere with thick clouds. Regarding this tendency, the sedimentation parameter is set to 2 for cloudy models and to 0 for cloudless models. In addition to cloudy models, SM08 simulates cloudless atmosphere with three different metallicities characterized by a metallicity index of [M/H]=0 for the solar metallicity, [M/H]=+0.3 dex and [M/H]=-0.3 dex[5].[10]

The evolution sequence of *Chabrier et al. 2000* is based on nongray atmosphere models that include dust formation and opacity for objects with $T_{eff} \in$[900, 2800] K. These models are called DUSTY and take into account dust scattering and absorption processes.[9]

On the opposite, the COND03 models neglect opacity and dust formation. They are based on nongray atmosphere models with effective temperatures ranging in [100,2800] K.[8]
Models developed in *Chabrier et al.* and *Baraffe et al.* account for conduction in the heat transport of brown dwarfs, compared to SM08 which neglects it. This difference leads to slightly higher luminosity predictions at a given age from COND03 and DUSTY models in comparison to SM08. However this difference decreases for smaller masses and thus becomes negligible. [10]

The evolution sequences of *Burrows et al.* are based on nongray cloudless atmosphere models for effective temperatures below 1300 K, developed by *Marley et al. (1996)*.[11]
This model uses the same equation of state and nuclear reaction rate as SM08 but considers a lower value for the helium abundance 0.25 compared to 0.28 for the COND03 models and to SM08. This low abundance results in less opaque atmosphere in comparison to other models.
In particular, BURR97 represent the cloudless models with low precision such as the lack of some sources of molecular opacity. Since BURR97 several improvements[6] concerning the evolution of brown dwarfs have been made. Therefore, this model sets an extreme boundary for the analysis of the predicted parameters.[10]

[5] decimal exponent

[6] (1) the recognition of the role of the K_I and Na_I resonance doublets at optical wavelengths (Burrows et al. 2000), (2) improved H_2 CIA opacity (Borysow et al. 2001; Borysow 2002), (3) a new line list for TiO (Allard et al. 2000; Freedman et al. 2008), (4) improved modeling of the condensation chemistry (Lodders 2002), (5) new sources of molecular opacity such as CrH, FeH, VO, and PH3 (Freedman et al. 2008 and references therein), and (6) expanded molecular opacity line lists—notably for CH_4 and NH_3 (Freedman et al. 2008).[10]

5.2 Analysis

From the Markov-Chain Monte Carlo analysis, it is perceived that the companion's mass is ranging in [34.4,38.8] M_{jup}. These masses correspond to a specific range of bolometric luminosities taken from models COND03 and DUSTY. Those models are exclusively considered as they are the only ones proposing apparent magnitudes in the L' band. The luminosities are correlated to absolute magnitudes in the L' optical band that provides information about the contrast:

$$contrast = 10^{(M_{comp_{L'}} - M_{star_{L'}})/-2.5} \tag{5.1}$$

This contrast is plotted within the allowed range of luminosities and compared to the contrast computed via the direct imaging algorithm.

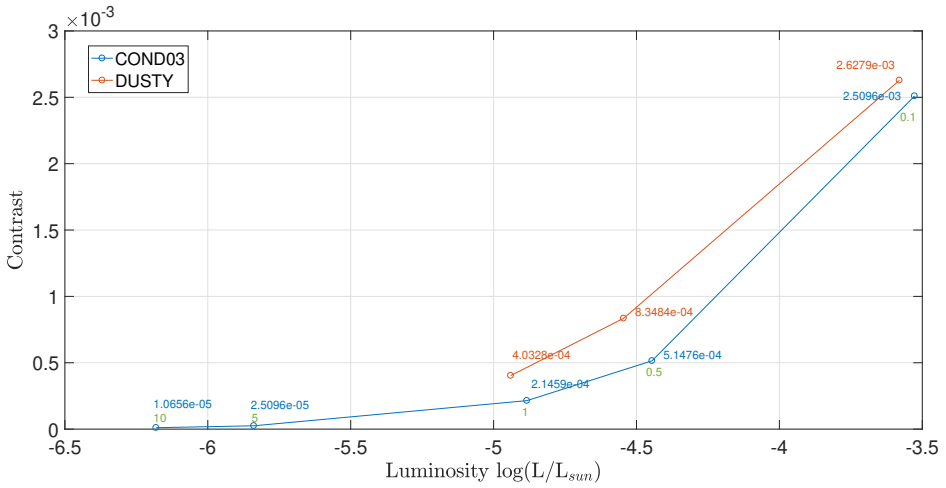

FIGURE 5.1: Contrast as a function of the bolometric luminosity for a fixed companion mass: 0.035 M_s. Model from *Baraffe et al.* for ages varying in [0.1,10] Gyr and from *Chabrier et al.* for ages varying in [0.1,1] Gyr in green.

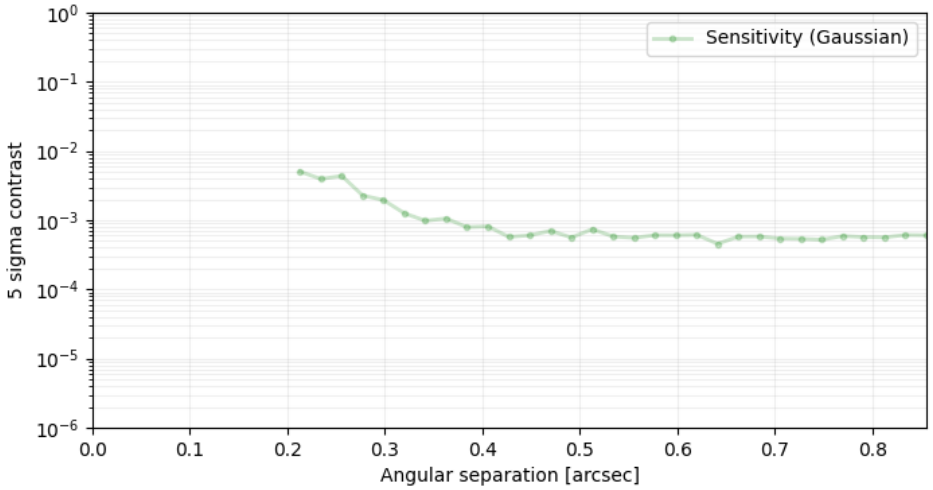

FIGURE 5.2: Contrast as a function of the angular separation computed with VIP from the direct imaging data.

Figure 5.2 demonstrates that for angular separation in [0.5,1] arcsec, the contrast is approximately of the order of 6×10^{-3}. This value imposes the threshold above which the companion can be detected. Since no companion is found with direct imaging, it can be deduced that the brown dwarf is below this detection

limit and therefore presents a lower contrast. This non-detection condition brings new information about the age of the companion.
Figure 5.1 proves that for contrast lower than 6×10^{-3} and a mass of 0.035 M_s, the companion is predicted to be older than at least 0.1 Gyr.

In addition to this contrast study, it is interesting to convert the VIP contrast into mass values. This conversion is displayed in Figures 5.3 and 5.4 and is based on the CON03 model for an age of 10 Gyr considering values in the L' filter. The COND03 model is considered for the conversation as it is the only model that provides magnitudes in the L' band.

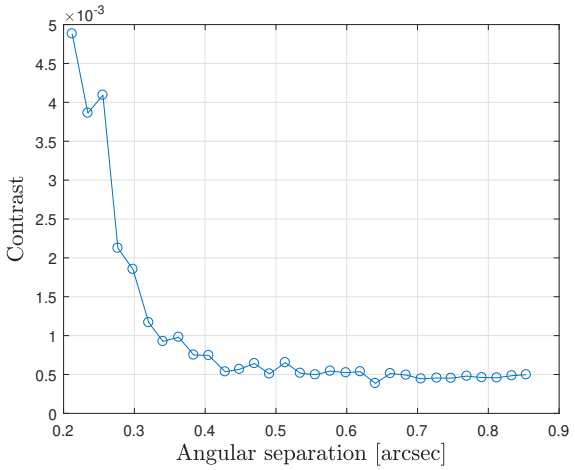

FIGURE 5.3: Contrast as a function of the angular separation computed via VIP from the ADI cube.

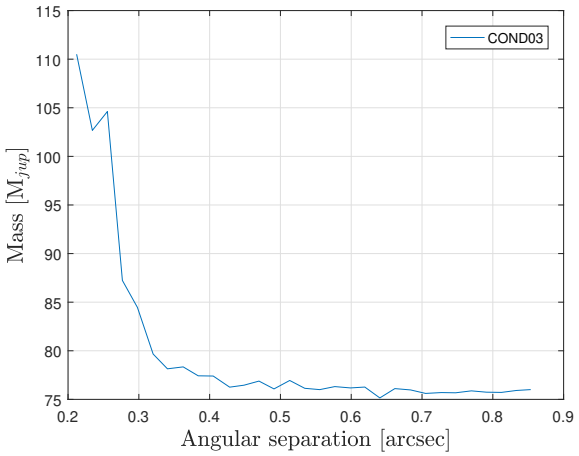

FIGURE 5.4: Mass of the companion in Jupiter mass as a function of the angular separation.

The mass curve from Figure 5.4 is decreasing with increasing angular separation and in overall displays the same profile as the contrast curve. More particularly, for angular separations higher than 0.8 arcsec, the mass of the companion corresponds to approximately 75 M_{jup} or 0.07 M_{sun}, which sets an upper limit on the mass. This means that objects at angular separation higher than 0.8 arcsec, would be detected for masses higher than 0.07 M_{sun}. Since VIP's methodology does not find any companion, its mass is below 0.07 M_{sun} which is in agreement with the mass derived via the MCMC analysis.

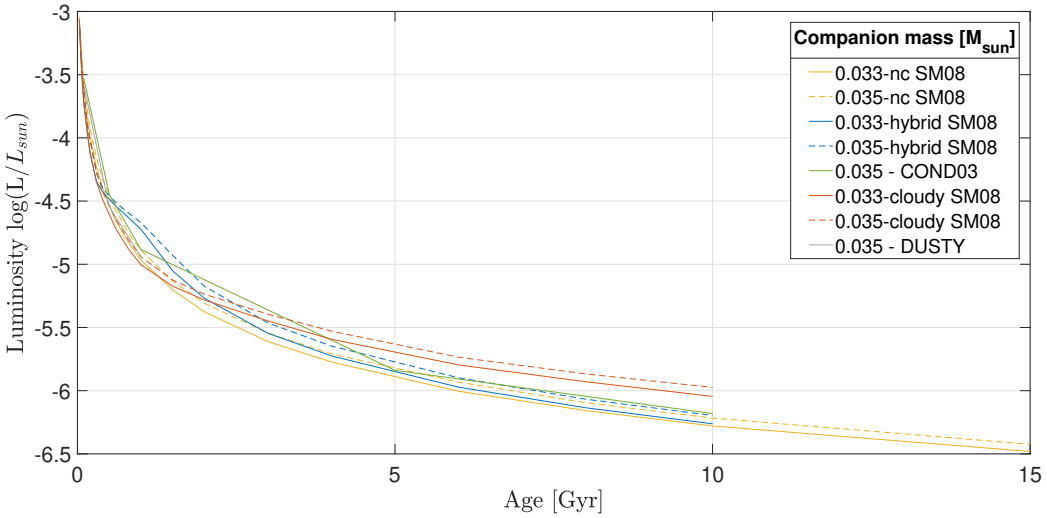

FIGURE 5.5: Bolometric luminosity as a function of the age of the companion for masses ranging in [0.03 0.0391] M_{sun}.

Figure 5.5 displays a general behaviour among the evolutionary models: luminosity is decreasing over time and a more massive companion is brighter at a given age.
Figures 5.5 and 5.6 show that the luminosity, mass and age of a substellar companion are related such as:

- At a given age, a massive companion presents higher luminosity than a lighter companion.
- At a given mass, an old companion is less luminous than a younger one.
- At a given luminosity, a young companion is lighter than an older one.

Therefore to determine the HD18757B age, the luminosity of the companion should be known. The luminosity must be determined with direct imaging, unfortunately as the companion has not been detected by high-contrast Direct Imaging, the companion's age is chosen within an interval and the luminosity is predicted from the evolutionary models. The stellar age cannot be measured but only determined via evolutionary models, empirical activity-age relations[7], gyrochronology[8] or asteroseismology[9]. Thereby, if we could have measured both luminosity and mass of the companion via direct imaging, then the age could have been estimated via the models. Regardless of this lack of information on the luminosity, another strategy is to set the age and find the luminosity via the evolutionary models.

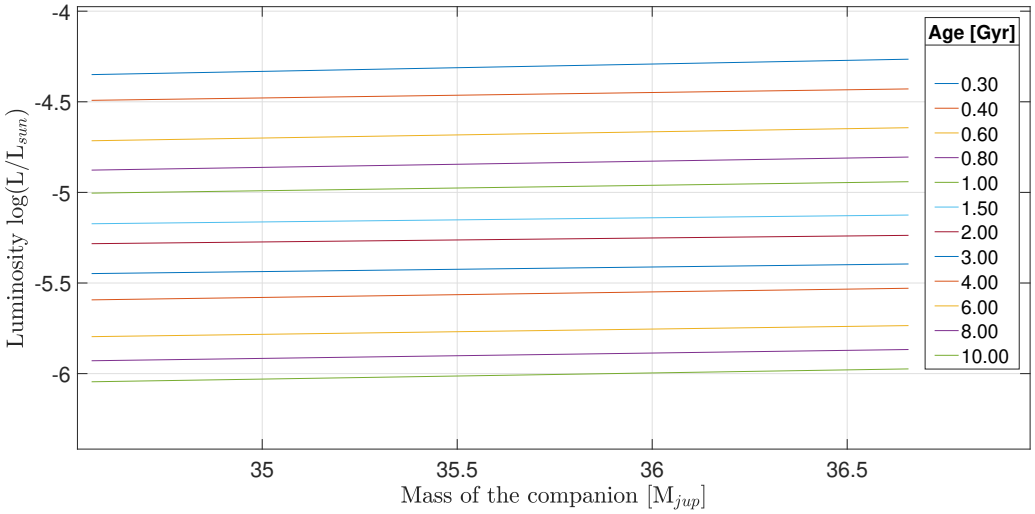

FIGURE 5.6: Mass of the companion, in jovian mass, as a function of the luminosity, in $\log(L/L_{sun})$, for a range of ages. Parameters from *Saumon 2008*, cloudy model.

Since the model predictions are based in a general way on two types of atmosphere: cloudy and non-cloudy, it is more relevant to analyse the parameters in each of these categories separately.

[7]Stars with high stellar activity are considered to be young, whereas low stellar activity characterizes old stars.
[8]It is a method for determining the age of star from the rotation period of the star. Young stars have a higher rotational rate than old stars.[48]
[9]*It is the science that studies the internal structure of stars by the interpretation of their frequency spectra.* In other words, it is the study of oscillations in stars.[49]

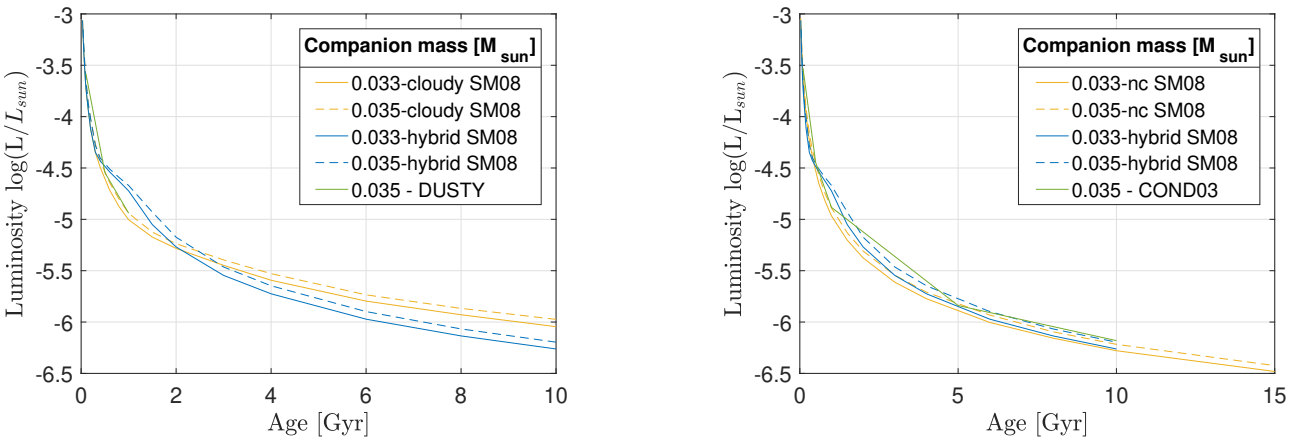

(a) (b)

FIGURE 5.7: Bolometric luminosity as a function of the age of the companion with (a) showing the SM08 hybrid, cloudy and the *Chabrier* DUSTY evolution model. And (b) showing the SM08 hybrid, cloudless and the *Baraffe* COND evolution model. The mass range is [34.393,38.798] M_{jup} which corresponds to the interval of confidence of 68% of the MCMC.

Figure 5.7(a) illustrates the DUSTY model extending up to 1 Gyr for masses in the considered range. This limitation comes from the lower bound on the temperature of the atmospheric model grid which is 900 K.[9] Since, the minimal age is fixed to 0.5 Gyr, DUSTY does not bring relevant information.
Regarding the cloudy *Saumon 2008* evolution model, it shows decreasing luminosities for increasing ages. This behaviour is expected for substellar companions as they cool down with time, thus diminishing their brightness.

From Figure 5.7(a), it is observed that both hybrid and cloudy evolution models display similar curves. The hybrid curve overlaps the cloudy one at younger ages, then predicts higher luminosities and lower ones for companions older than 2 Gyr.
Since brown dwarfs are characterized with cloudy atmospheres that condensate with time as the temperature drops down, the hybrid model is used to describe dwarfs in the L-T transition. In practice this transition represents a passage from a cloudy to a cloudless atmosphere as they grow older.

Regarding Figure 5.7(b), it reveals that the three models are quite similar. At young ages, the hybrid predictions match the ones of the non-cloudy SM08, it predicts higher luminosities than nc-SM08 for ages of 1 and 2 Gyr, then the curves overlap again. This behaviour is once again explained by the atmosphere composition change.
For the third model on the graph CON03, it roughly predicts lower luminosities than hybrid and non-cloudy.
In general, the lack of dust and clouds leads to lower luminosities at a given age and older companion at a given luminosity. The latter is explained by the interior temperature of the object which is lower compared to a cloudy model, due to the cloudless atmosphere.

In addition to luminosity and age, the evolution models bring information about the temperature, the radius, the metallicity and the gravity.

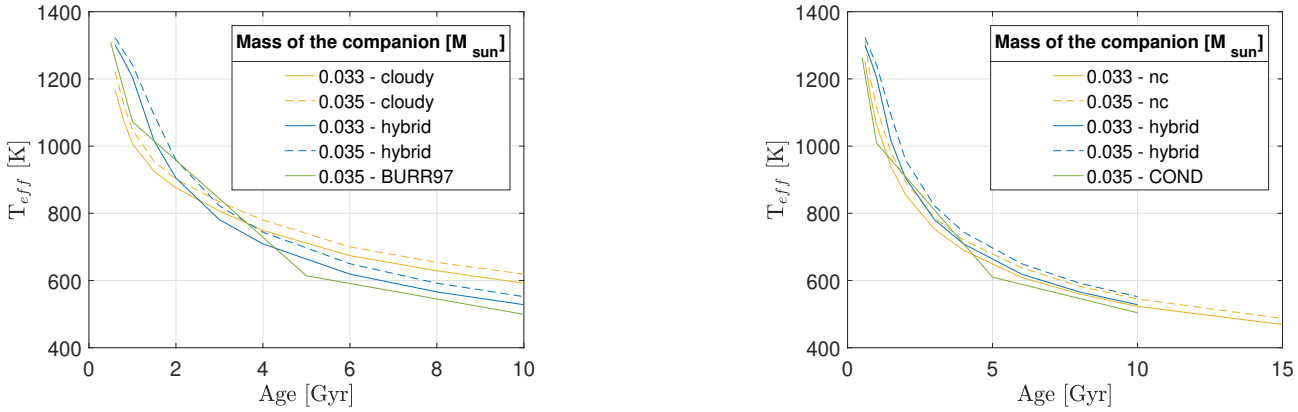

(a) (b)

FIGURE 5.8: The effective temperature of the companion as a function of the age with (a) showing the SM08 hybrid, cloudy and Burrows evolution models. And (b) showing the SM08 hybrid, cloudless and the *Baraffe* COND03 evolution models. The mass range is [34.393,38.798] M_{jup} which corresponds to the interval of confidence of 68% of the MCMC and the age's interval is [0.5 15] Gyr.

Figure 5.8 exhibits the evolution of the effective temperature of the companion over the ages of [0.5,15] Gyr. The graph shows that within this age range, the temperature is varying in [500,1323] K.
As expected the cloudy model predicts higher temperatures compared to the cloudless SM08. This difference is due to the presence of clouds that lead to larger opacities thus higher temperatures.

Furthermore, Figure 5.9 displaying the radius of the companion, confirms that HD18757B is a small companion with a radius in [0.8558,1.065] R_{jup}. Finding such radius interval enhances the brown dwarf companion initial hypothesis since substellar objects are expected to have radii close to Jupiter ones.[1]
Figure 5.9 shows also that cloudy models predict higher radii than cloudless models. This difference comes from the slow radius shrinkage in cloudy atmospheres, thus resulting in larger radii at a given mass and age. In fact, '*The brown dwarf's atmospheric opacities determine the rate with which heat escapes the convective core, and at which the core entropy evolves, and it is the core entropy which sets the radius, for a given mass and internal composition*'.[50]

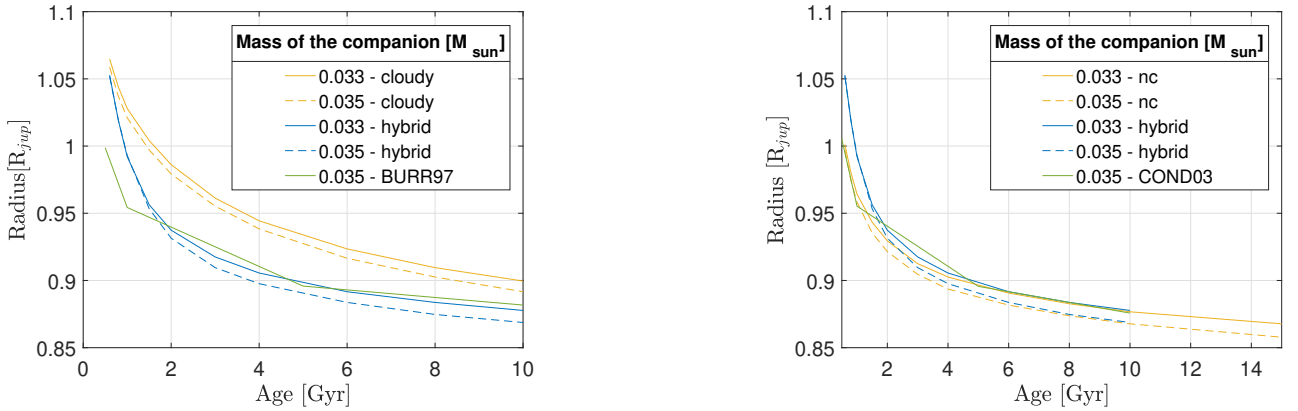

(a) (b)

FIGURE 5.9: Radius as a function of the age of the companion with (a) showing the SM08 hybrid, cloudy and Burrows evolution models. And (b) showing the SM08 hybrid, cloudless and the *Baraffe* COND evolution models. The mass range is [34.4,38.8] M_{jup} which corresponds to the interval of confidence of 68% of the MCMC.

As explained at the beginning of this analysis, the companion's age is chosen within an interval in order to assess the luminosity via the evolutionary models. It is possible to narrow down the companion's age interval by considering the age of the host star predicted by *Bouchy et al.*. This discussion is developed in the following section.

5.3 Analysis with a fixed age

The age of HD18757 is estimated to $11.4^{+0.1}_{-0.1}$ Gyr by *Bouchy et al.*. As it is considered that the protoplanetary disk and the surrounding substellar objects are created at the same time as the star, this age is assumed for the companion HD18757B.

By fixing the companion's age, the luminosity, radius and effective temperature are directly given by the different evolutionary models. Figure 5.10 depicts these parameters in terms of the companion's age and conveys that for a companion of 11.4 Gyr, the three parameters are ranging in an interval.

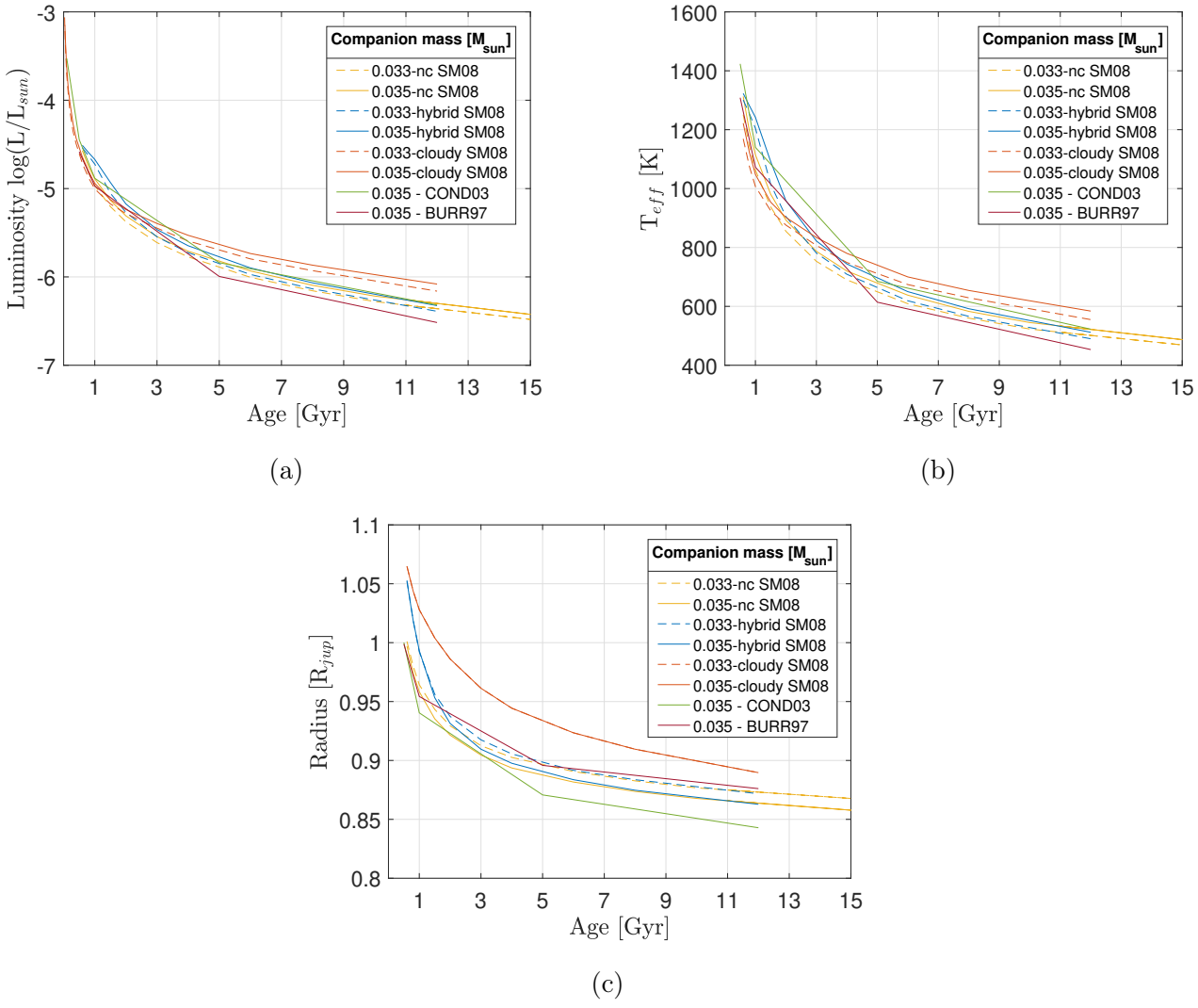

FIGURE 5.10: Bolometric luminosity (a), effective temperature (b) and radius (c) as a function of the age of the companion showing the SM08 hybrid, cloudy, cloudless models, the *Baraffe* COND03 and Burrows evolution models. The mass range is [34.4,38.8] M_{jup} which corresponds to the interval of confidence of 68% of the MCMC.

Graphs indicate luminosities ranging in [-6.516,-6.0275]. These range boundaries correspond to *Burrows* and cloudy SM08 evolutionary models, both models represent extreme cases in terms of the clouds

simulation in the atmosphere. In fact, BURR97 neglects cloud opacity, dust formation and considers a lower abundance of helium leading to a lower luminosity while SM08 models clouds via a sedimentation factor, hence showing a more luminous atmosphere.
For the radius, it is shown that the size of the companion is of the order of a Jovian planet, [0.8429,0.8946] R_{jup}.

Regarding the effective temperature, the parameter is within [464.8,601.5] K for an age of 11.4 Gyr. The interval's boundaries are derived from the SM08 cloudy for a mass of 0.035 M_{sun} and BURR97. It is viewed that there is a temperature difference of approximately 140 K between the cloudy and non-cloudy model.
With this temperature range, it can be deduced that HD18757B is at least a T-type dwarf. These cool T dwarfs are also called methane dwarfs due to a typical signature of methane absorption. This methane stage is associated to a cloudless atmosphere since all dust has precipitated. Therefore, COND03, BURR97 and cloudless SM08 models are most suitable to describe the companion's properties, highlighted in Figure 5.11.

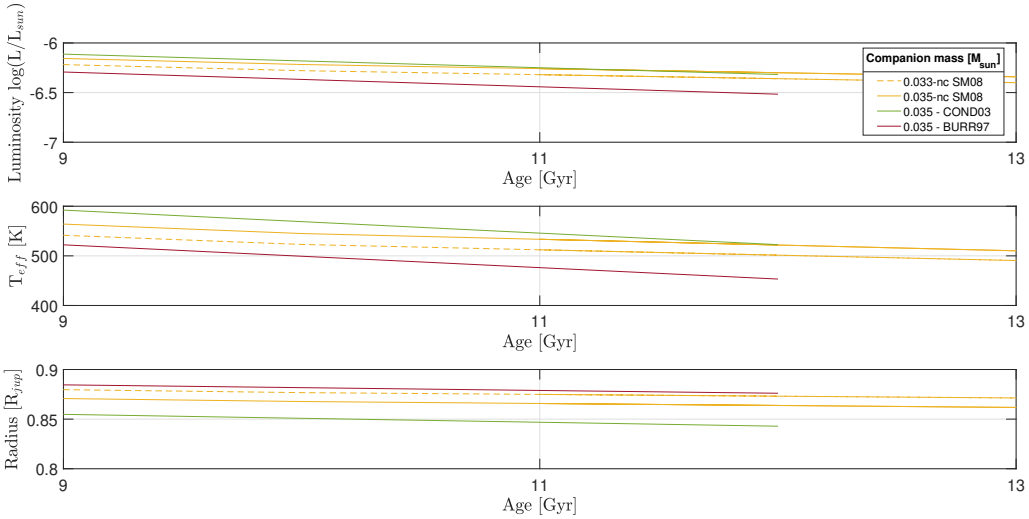

FIGURE 5.11: Bolometric luminosity, effective temperature and radius as a function of the age of the companion showing the SM08 cloudless [M/H] = 0, COND03 and BURR97 evolutionary models. The mass range is [34.4,38.8] M_{jup} which corresponds to the interval of confidence of 68% of the MCMC.

It is possible to refine the analysis by taking the cloud-free model from *Saumon 2008* with a metallicity of [M/H] = -0.3. This metallicity index is closer to the one predicted by *Bouchy et al.* for the host star, [Fe/H] = -0.27+/-0.02 dex. As the companion is supposed to be a brown dwarf, its creation results from the same dust clouds compression as the host star, supposing the gravitational disk instability formation scenario (refer to section 6). Thereby, it is reasonable to consider the same metallicity between the companion and the parent star.

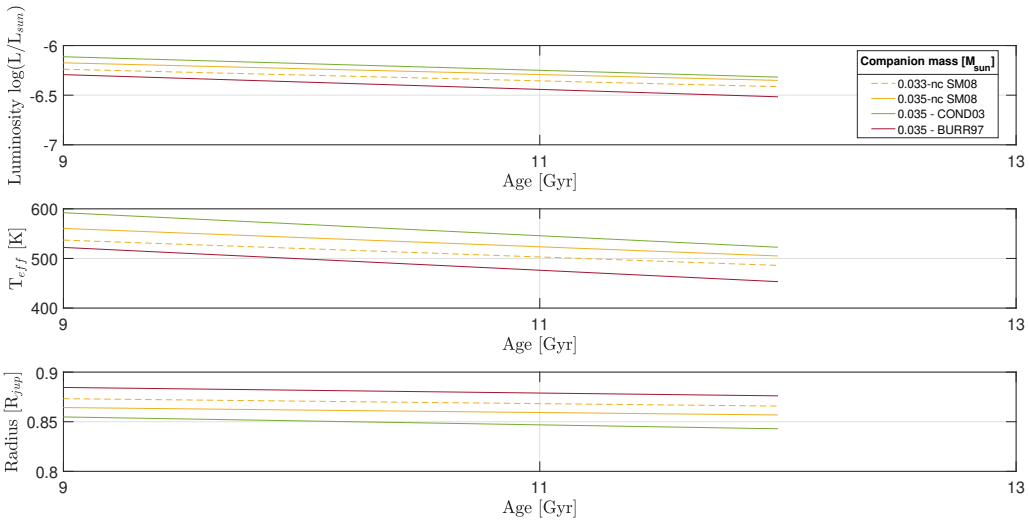

FIGURE 5.12: Bolometric luminosity, effective temperature and radius as a function of the age of the companion showing the SM08 cloudless [M/H] = -0.3, COND03 and BURR97 evolutionary models. The mass range is [34.4,38.8] M_{jup} which corresponds to the interval of confidence of 68% of the MCMC.

Figure 5.12 exhibits the characteristics of the object derived from non-cloudy models. For an age of 11.4 Gyr and mass of 0.035 M_{sun}, the companion's effective temperature is predicted within a range of [514,534] K, its radius is approximately [0.849,0.862] R_{jup} and the luminosity is varying within [-6.321,-6.283]. Note that the extrema of each interval correspond to models nc SM08 and COND03 given that BURR97 is less accurate.

Besides, it is noticed that a lower metallicity (-0.3 dex) leads to lower bolometric luminosities, lower temperatures and lower radii. This behaviour is explained by the fact that metallicity is related to the atmopsheric thickness such as high metallicity leads to higher thickness atmospheres.[50] As a consequence, a low metallicity object presents a less opaque atmosphere resulting in a colder, fainter and smaller object.

In parallel with this comparison between the evolutionary models for the nominal mass, it is interesting to analyse the predicted parameters for each model within the allowed range of mass such that $m_{planet} \in$ [34.4,38.8] M_{jup}.
This evaluation is traced in Figure 5.13 where the three parameters vary in terms of the companion mass. These plots reveal that model COND03 estimates higher bolometric luminosities and effective temperatures in comparison to non-cloudy SM08 and BURR97. And COND03 foresees the lower radii in contrast with the two other models.

By looking at each model individually, the parameter's range is:

- COND03: bolometric luminosity $\in$ [-6.354, -6.204], $T_{eff} \in$ [509.627, 561.888] K and radius $\in$ [0.8351, 0.856] R_{jup}.
- SM08: bolometric luminosity $\in$ [-6.384, -6.251], $T_{eff} \in$ [494.589, 536.39] K and radius $\in$ [0.849, 0.868] R_{jup}.
- BURR97: bolometric luminosity $\in$ [-6.536, -6.410], $T_{eff} \in$ [447.039, 485.926] K and radius $\in$ [0.868, 0.888] R_{jup}.

Overall, each evolutionary model outputs close predictions and presents similar tendencies: as the companion's mass increases, the luminosity and the effective temperature of the substellar object grow as well, on the contrary of the radius which diminishes with increasing mass.
The relation mass-radius of brown dwarfs is dominated by the electron degeneracy pressure[10] which induces: [51]

$$radius \approx mass^{-1/3} \tag{5.2}$$

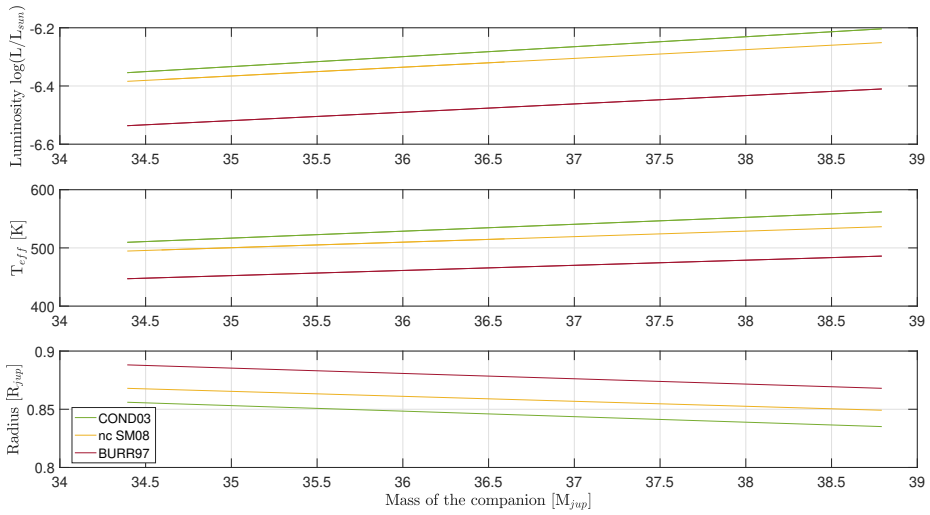

FIGURE 5.13: Bolometric luminosity, effective temperature and radius as a function of the companion's mass showing the SM08 cloudless [M/H] = -0.3 dex and COND03 and BURR97 for an age of 11.4 Gyr. The mass range is [34.4,38.8] M_{jup} which corresponds to the interval of confidence of 68% of the MCMC.

These observations draw a very cool and low luminous object with a size comparable to a Jovian planet. This description matches the late-T and early-Y spectral type of brown dwarfs.
As this substellar object is very faint, it is difficult to detect it by direct imaging method. Figure 5.14 exhibits that such an object is characterized by a contrast of the order of 10^{-6} which is below the detection limit contrast curve computed by VIP.

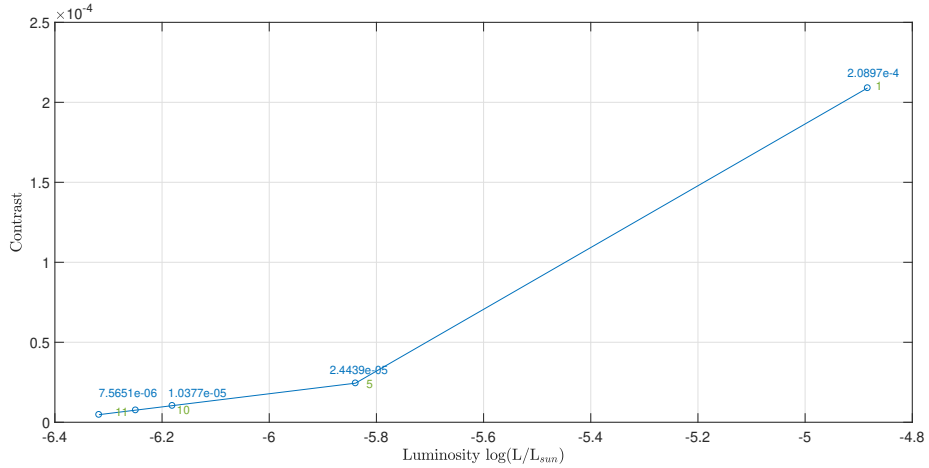

FIGURE 5.14: Contrast as a function of the bolometric luminosity for a fixed companion mass: 0.035 M_s. Model from *Baraffe et al.* for ages varying in [1,11] Gyr in green.

[10]The electron degeneracy pressure is based on the Pauli Exclusion Principle which states: '*no electrons in an atom are permitted to have an identical set of quantum numbers*'. In cold dense-core objects, fast moving electrons generate pressure. In particular, this pressure is balanced against brown dwarf's self gravity and prevent them from collapsing.[51]

5.4 Spectral type T & Y

Brown dwarfs are classified by spectral types which are based on the effective temperature and the atmosphere composition. As a result, in order to assign a spectral class to these objects, it is essential to analyse their spectra with the characteristic absorption bands.

T dwarfs

Brown dwarfs of type T are characterized by a specific spectral signature of methane absorption in the near-infrared [1-2.5] µm. Specifically, the dominant absorption bands are the CH_4 and H_2O in T dwarfs. These T spectral types range from T_{eff} = 1800 K down to 800 K.[52]

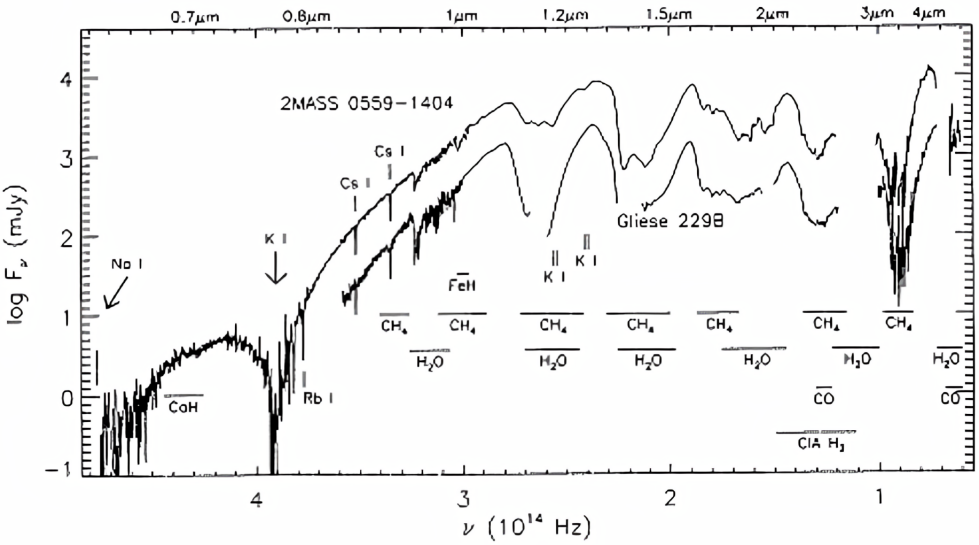

FIGURE 5.15: Spectra of two T dwarfs, 2 MASS 0559-1404 (*Burgasser 2001*) and Gliese 229B (*Oppenheimer et al. 1998*), from 0.63-5.7 µm with major absorption features indicated. [52]

Figure 5.15 depicts the spectral type of two T-dwarfs Gliese 229B, the first T-dwarf discovered, and 2MASS 0559-1404. Both dwarfs share common absorption features such as methane absorption bands at 1.6 µm and 2.2 µm, and H_2O absorption bands around 1.15µm. Along with these two main components, the spectra show common absorption peaks of CsI, KI and NaI.

It is customary to represent stars' spectra with a normalized flux density f_λ such as in Figure 5.16. This graph exhibits a narrower range of wavelengths, focusing on the near-infrared part of the spectrum. The characteristic features of T-dwarfs are displayed with the H_2O and CH_4 absorption bands.

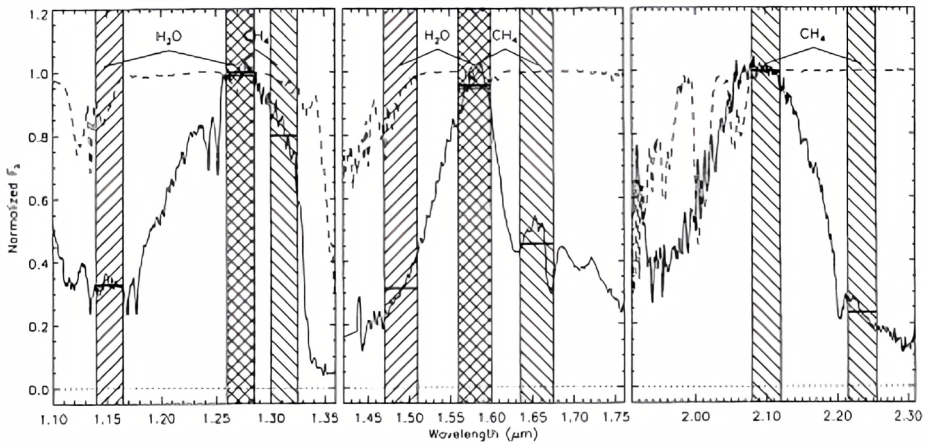

FIGURE 5.16: Spectral indices defined in the joined classification scheme of B02 and G02. G02 scheme is based on a homogeneous sample of early-type T dwarfs down to SSDS and G02 extends to include L dwarfs. Hatched areas indicate spectral regions sampled for H_2O and CH_4 band indices. Normalized GS4 spectra of 2MASS0559-1404 (G02; solid lines) and telluric absorption at Mauna Kea (dashed lines) are plotted for comparison. [52]

Y dwarfs

The spectral type Y is necessary because brown dwarfs cooler than 600 K, exhibit change in their atmosphere. At T_{eff} = 600 K, absorption bands of NH_3 are detected. When temperature reaches 500 K, the resonance bands of NaI and KI weaken. Finally for temperatures from 350 K down to 200 K, NH_3 and H_2O condense out.[53]

Regarding this change of composition, several features can be detected on the spectrum in order to distinguish a Y-dwarf from a T-dwarf. Nonetheless, this spectral type is recent and it is still under study due to the difficulty of observing this type of brown dwarfs. Indeed, Y-dwarfs are very faint so obtaining high-quality spectra is complicated.

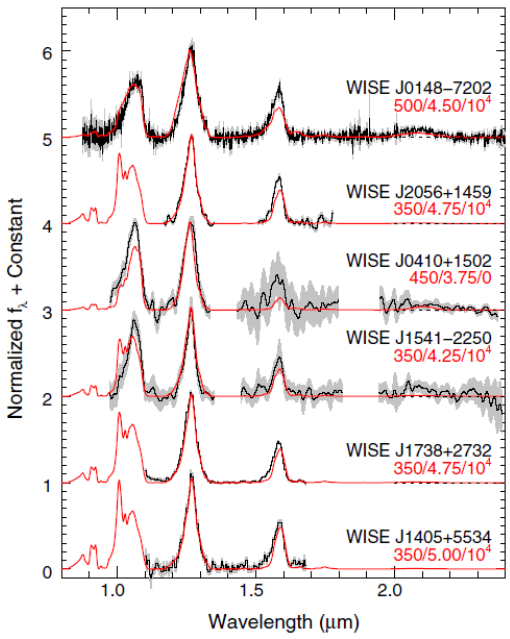

FIGURE 5.17: Best-fitting models (red) overplotted on the near-infrared spectra of six of the seven new WISE brown dwarfs (black). The spectra were normalized to unity at the peak flux in the J band and offset by constants (dotted lines). The uncertainties in the spectra are given by gray bars. The best-fitting model parameters are given in the form T_{eff}(K)/log g (cm s^{-2})/K_{zz}(cm^2 s^{-1}). [54]

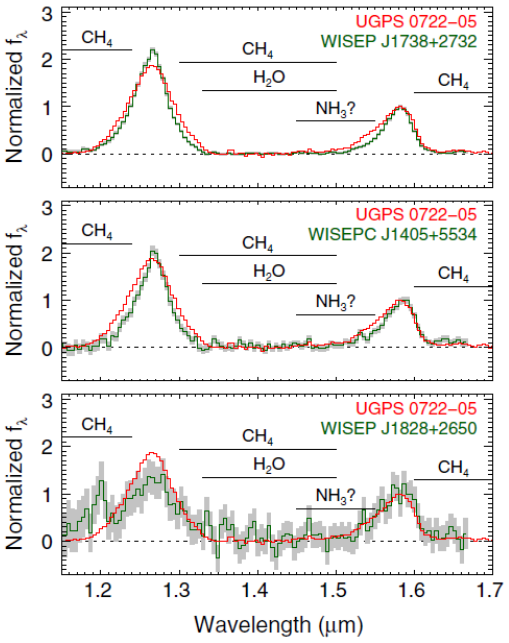

FIGURE 5.18: 1.15-1.70 μm spectra of WISEP J1738+2732, WISEPC J1405+5534, and WISEP J1828+2650 along with the spectrum UGPS 0722-05. The uncertainties in the spectra are shown as gray bars. The spectra were all normalized to unity at the peak of the H band (1.58 μm). Prominent molecular absorption bands are indicated. [54]

Initially, scientists looked for the absorption band of NH_3 which represents the transition from the T to Y type brown dwarfs. Figure 5.19 shows that WISEP j1738 displays additional absorption around 1.56 μm in comparison to the T-dwarfs. This extra absorption matches the NH_3 absorption band, thus potentially being the cause of this spectrum difference. However, this specific feature is difficult to distinguish given the NH_3 absorption band overlaps with the H_2O absorption band.
The spectral signature of Y dwarfs is also represented in Figure 5.18 where the ammonia absorption bands are underlined.

A second feature that distinguishes a Y-dwarf from a T-dwarf is the wideness of the J band peak at 1.27 μm. Figure 5.20 exhibits the J band peak of some late T-dwarfs, which are wider in comparison to the J bands peaks of early Y-dwarfs. Moreover, a narrower J band peak indicates a later subclass of Y-dwarf as it is observed with Y0 and Y1 type dwarfs.

Another way to differentiate the two types, is by looking at the H- and J- band peaks. The heights of these peaks in flux density units of f_λ must be approximately equal such as for WISEP J1828+2650 in Figure 5.18. In conjunction with this spectral specificity, Y-dwarfs usually present a higher Y-band peaks than J-band peaks at 1.07 μm which is not found in late-T dwarfs. This distinction that is shown in Figure 5.17, is due to the disappearance of the alkali resonance lines, KI ans NaI, under 500K.

Furthermore, Y-dwarfs mostly emit in the mid-infrared.[54] On that account, in order to detect and characterize these cool objects, it is better to observe in this wavelength's range. However, the mid-infrared extending from 2.5 μm to 25 μm, overlaps with the thermal radiation of Earth which emits in the

same wavelengths' range. This overlapping restrains the observation to space-based telescopes where the thermal radiation cancels out.

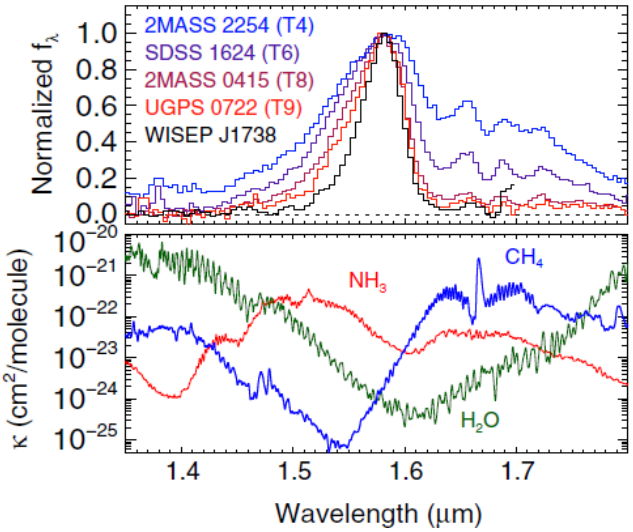

FIGURE 5.19: Top: H-band spectrum of several brown dwarfs denoted on the graph. The spectra have been normalized to unity at their peak flux values. Bottom: opacity data computed in chemical equilibrium for NH_3 (*Yurchenko et al.2011*), H_2O (*Freedman et al.2008*) and CH_4 (*Freedman et al.2008*) at T = 600 K and P = 1 bar. Note that the change in the spectral morphology of the blue wing of the H-band peak is similar between T6/T8 and T8/T9 suggesting a common absorber or set of absorbers. In contrast, the spectrum of WISEP J1738+2732 exhibits excess absorption that matches the position of the NH_3 absorption shown in the lower panel.[54]

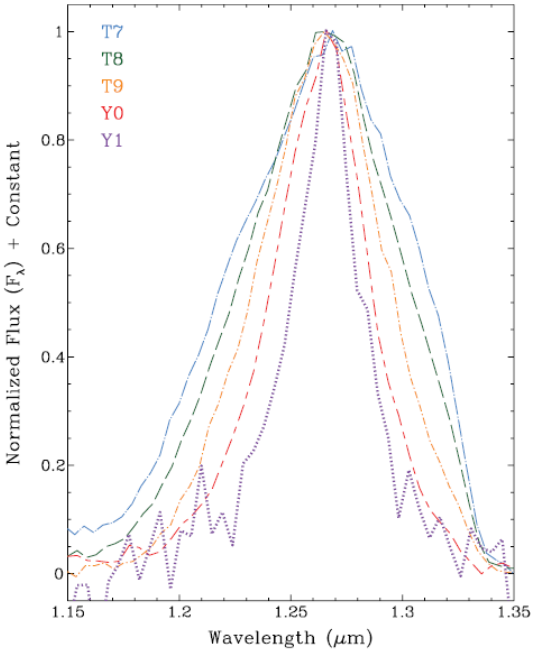

FIGURE 5.20: Overplots of the J-band spectra of the T7, T8, T9, and Y0 standards 2MASS 0727+1710 (light blue, dot/long-dash; *Burgasser et al.2002*), 2MASS 0415-0935 (green, dash; *Burgasser et al.2002*), UGPS 0722-0540 (gold, dot/short-dash; *Lucas et al.2010*), and WISE 1732+2732 (red, long-dash/shortdash;*Cushing et al.2011*), respectively, along with the proposed Y1 standard, WISE 0350-5658 (purple, dot). All spectra are normalized to one at their peak flux.[53]

To summarize, Y dwarfs display particular features in the J and H bands respectively at 1.22 µm and 1.63 µm. In particular, the peaks' height and wideness distinguish T and Y type dwarfs. For this reason, HD18757B must be spotted with instruments, from Earth, observing in the J and H filters thus covering a part of the near-infrared. With future space-based telescopes, cold substellar objects would be better detected in the mid-infrared so in L and M spectral filters.

Considering the effective temperature range of [514, 534] K predicted by evolutionary models and the characteristics of the T and Y spectral type, it is found that the Y-type is more appropriate for HD18757B. Nevertheless, the evolutionary model analysis is based on several assumptions that can biased the conclusion. As a consequence, HD18757B is labeled as a potential T-late or early Y-type brown dwarf until the uncertainty is lifted with further observations.

6 Formation models

As brown dwarfs draw the separation between planets and stars, their mode of formation is unclear and two formation scenarios are considered. The first one is the gravitational instability model which belongs to the family of planets formation models whereas the second one is related to stars formation.

6.1 Gravitational disk instability

The gravitational instability (GI) is one of the formation model of massive gas giant planets and substellar objects along with the core accretion (CA) model. The GI formation scenario assumes that companions are created from a gravitational fragmentation of the circumstellar disk resulting from a gravitational instability. The fragments collide and merge reaching a planetesimal-size aggregate composed of rocks, dust and gas. As the contraction between the fragments continues, sedimentation of dust grains forms layers and the protoplanet migrates towards the host star. Sedimentation is then stopped due to gas turbulence, collisional destruction and evaporation. Eventually this process outputs wide-orbit massive gas giants and brown dwarfs.[12]

This planetary formation scenario is modeled by *Vigan et al. 2017* and accounts for dynamical interactions between objects in multiple companions system. These interactions consist mainly of planet ejection, also called scattering. Consequently two population synthesis models are computed, with and without dynamical interactions, or scattering.

The generated populations with and without scattering are drawn in Figure 6.1 where the red square characterizes HD18757B. It appears that the semi-major axis and the mass of HD18757B are compatible with the distribution of single systems, which is in accordance with what is currently known of the studied system.

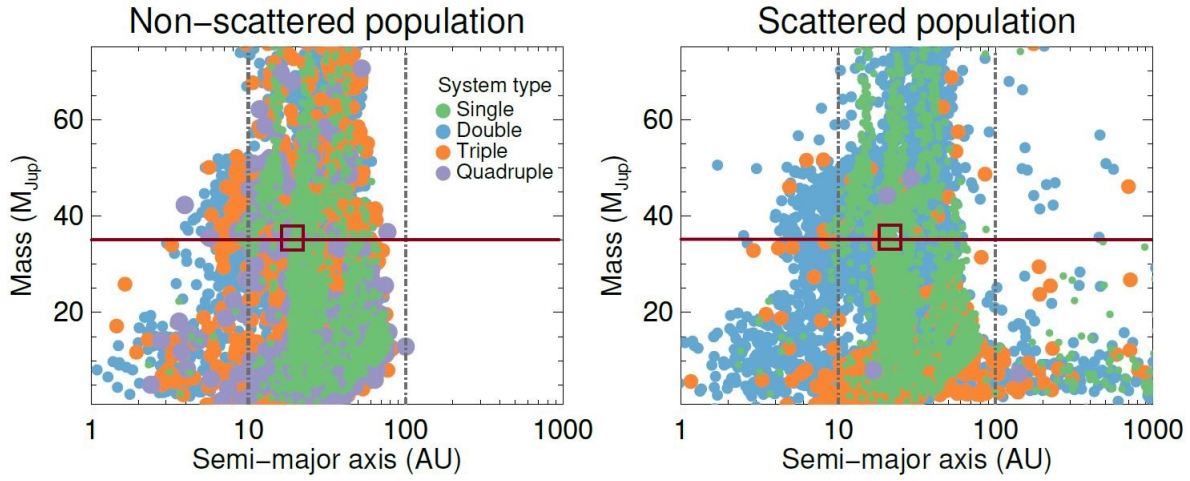

FIGURE 6.1: Mass (M_{Jup}) versus physical separation (AU) for all the companions in the synthetic planet populations generated. Left panel: non-scattered population (*Forgan & Rice 2013*). Right panel: same population including scattering (*Forgan et al. 2015*). Different colors are used for single (green), double (blue), triple (orange), and quadruple (purple) systems. The size of the symbols increases from single to quadruple systems to make the plots easier to read.[12]

The GI simulation of *Vigan et al. 2017* also shows that this formation mechanism is not common and predicts companions at semi-major axis of at least 30-50 AU. These companions can then move closer to their parent star via scattering or tidal evolution which could explain HD18757B separation of 20 AU. Regarding the rarity of this formation scenario, the analysis displayed in Figure 6.2 highlights the fact that GI predicts a better mass-distribution of wide-orbit substellar companions than the core accretion model. By considering HD18757B semi-major axis and mass, it can be deduced that the best suited planetary

formation mechanism is the disk fragmentation by gravitational instability. Besides the model comparison, Figure 6.2 shows that objects similar to HD18757B have high occurrence and are situated above the 50% detection probability curve. This detection frequency comes from an imaging survey performed with the VLT/NaCo instrument by *Vigan et al.*. This result means that if HD18757B was observed in the survey, it would have been detected in 50% of the cases.

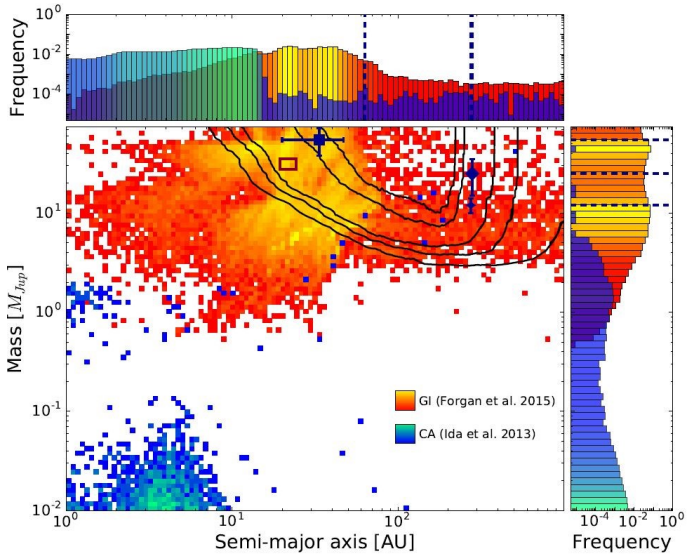

FIGURE 6.2: Density plots representing scattered populations based on GI (*Forgan & Rice 2013; Forgan et al. 2015*) and CA (*Ida et al. 2013*) compared to the detections in the sample and to the mean detection probabilities of the observations (contour lines are at 5%, 25%, 50%, 90%, and 95%). Density colors go from dark blue (low occurrence) to cyan (high occurrence) for the CA population, and from red (low occurrence) to yellow (high occurrence) for the GI population. The histograms on top and on the right represent the relative frequency in each bin of semi-major axis and planetary mass respectively. The histograms take into account the whole population, including the planets that are outside of the visibility window of the main plot. The semi-major axis and mass of the known companions are represented with dashed lines in the histograms.[12]

Furthermore, *Ma & Ge 2014* found that brown dwarfs with mass smaller than 40 M_{jup} are more likely to be formed in a protoplanetary disk than via protostellar disk fragmentation. They also assumed that the high eccentricity distribution can be explained by scattering and they stated that the metallicity of brown dwarf's host star is usually low.[1] This observation matches the poor metallicity of HD18757 which strengthens the hypothesis of HD18757B being a substellar companion.
The eccentricity parameter is not discussed in *Vigan et al. 2017* as it is expected to vary greatly over time. However, disk gravitational instability model is presumed to produce low-eccentricity companions due to external interactions in multiple object systems and interactions with the disk that tend to damp the eccentricity.

6.2 Protostellar disk fragmentation

Stars formation results from the gravitational collapse of molecular clouds. More precisely, the compression of molecular clouds induces an abrupt increase of density and temperature, consequently leading to the creation of a protostellar embryo. During this collapse, the resulting density field is highly contrasted meaning that some zones, ones with higher densities, are gravitationally unstable. These unstable regions fragment into sub-units creating star clusters, binary systems and brown dwarfs.[1]

Considering this protostellar disk fragmentation scenario, *Bate 2009* models the process via two large-scale hydro-dynamical calculations of the collapse and fragmentation of turbulent molecular clouds. The

simulation outputs 1254 stars and brown dwarfs among which 18 very low mass (VLM), objects with mass smaller than 0.1 M_{sun}, binaries with mass in [0.03,0.07] M_{sun}.

The simulation predicts several parameters such as the semi-major axis, the mass-ratio and the eccentricity. From Figure 6.3 which displays the number of VLM generated as a function of the semi-major axis, it is viewed that the number of low mass objects at smaller separations increases with time[11]. This means that '*VLM systems may form with reasonably wide separations and evolve to smaller separations*'.(*Bate 2009*) In addition to this tendency, the simulation predicts that binary systems with host star ranging in [0.5,0.8] M_{sun} have companions' semi-major axis within [27,65] AU.
Since HD18757B semi-major axis is estimated to approximately 20 AU and the host star's mass is constrained to 0.881 M_{sun}, it can be assumed that the companion's initial separation was higher such as in [27,65] AU and then decreased over time.

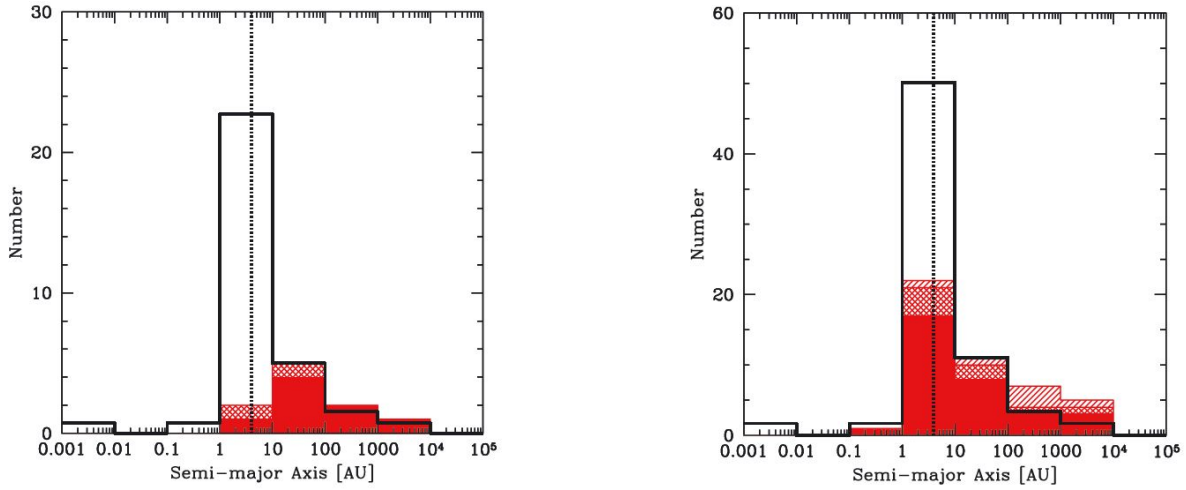

FIGURE 6.3: The distributions of separations (semi-major axes) of multiple systems with VLM primaries produced by the main calculation at t = 1.038 t_{ff} on the left panel and t = 1.5 t_{ff} on the right panel. The solid, double-hashed and single-hashed histograms give the orbital separations of binaries, triples and quadruples, respectively. The open black histogram gives the (scaled to match the number in the 10–100 au range) separation distribution of the known VLM multiple systems maintained by Nick Siegler at http://vlmbinaries.org/ (last updated on 2008 February 4). The vertical dotted line gives the resolution limit of the calculations as determined by the gravitational softening and accretion radii of the sink[12]particles.[13]

Regarding the mass distribution, it can be noticed from Figure 6.4 that most of the very low mass objects evolve into heavier objects with time. This may be explained by the dynamical interactions within the system during the formation.
The mass ratio between HD18757B and its host star is roughly 0.039 which is not the most common mass ratio in the simulated binary system. Therefore, our system is rare but can still be explained with this formation scenario. In particular, by looking on the dependence between the semi-major axis and the eccentricity, depicted in Figure 6.5, it is inferred that objects like HD18757B are formed but in minority. The graph highlights a concentration of binaries with high mass ratio which indicates that companions are more likely to have a mass similar to their host star.

[11]The time is expressed as the free-fall time t_{ff} which represents the time taken for a pressure free, spherical cloud to collapse to a point owing to its self-gravity.(*McKee & Ostriker, 2007*)
[12]Sink particles are required in collapse simulations to model dense core, star, or black hole formation and accretion

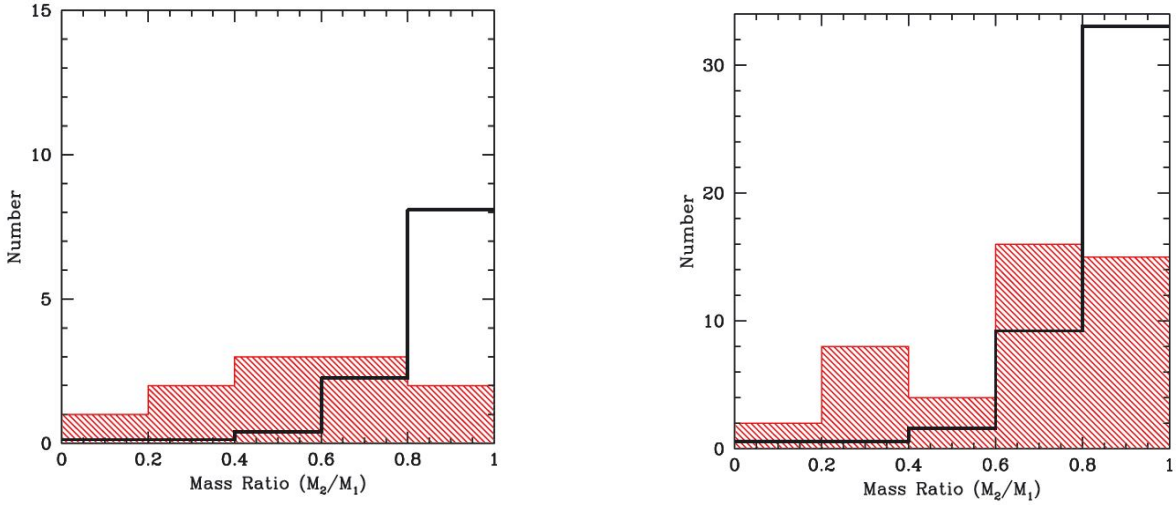

FIGURE 6.4: The mass ratio distributions of binary systems with VLM primaries M_1 <0.1 M_{sun} produced by the main calculation at t = 1.038 t_{ff} on the left panel and t = 1.5 t_{ff} on the right panel. The solid black lines give the observed mass ratio distributions of the known VLM binary systems maintained by *Nick Siegler* at http://vlmbinaries.org/.[13]

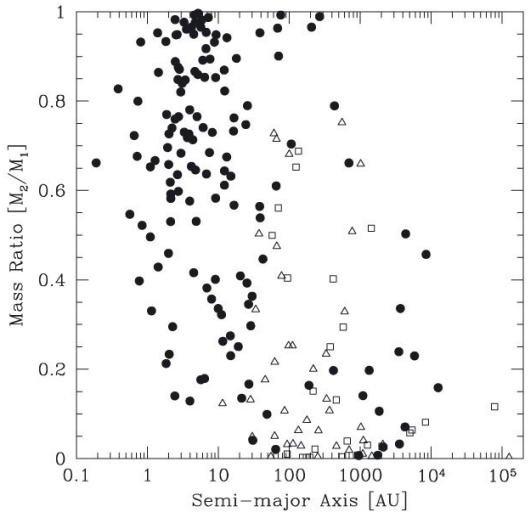

FIGURE 6.5: The mass ratios of binaries (filled circles), triples (open triangles) and quadruples (open squares) as a function of semi-major axis for the main calculation. All mass ratios are defined to be ≤1. There is a clear relationship between mass ratio and separation with closer binaries having a greater fraction of near equal-mass systems.[13]

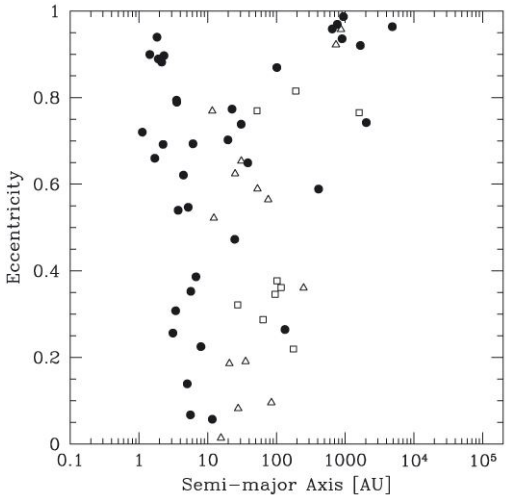

FIGURE 6.6: The eccentricity distribution of binary (filled circles), triple (open triangles) and quadruple orbits (open squares) as a function of semi-major axis at t = 1.038 t_{ff}.[13]

As for the eccentricity parameter which is displayed in Figure 6.6, it can be observed that for binaries at small separations, the eccentricity distribution is dispersed with a small concentration around 0.9. And at larger separations, high eccentricity are favored. Since this simulation presents the formation at 1.038 t_{ff}, the shape of the orbit is still expected to change considering external interactions.
Given that HD18757B is on a highly eccentric orbit, it matches the simulated eccentricity distribution. However, this parameter is quite sensitive to study because it can vary greatly with time due to external

phenomena such as planet-planet interaction, external source of perturbation and so on. Therefore, the actual eccentricity of HD18757B may strongly differ compared to the initial one due to the time difference of approximately 10 Gyr.

Another theory that may explain the companion's high eccentricity is the Kozai mechanism. This mechanism assumes a third body perturbation on a binary system which increases the initial eccentricity and impacts the inclination.[1] To this date, no other object around the star HD18757 has been detected but it could have potentially been ejected by HD18757B.

6.3 Models Comparison

The reviews of the Gravitational disk instability and Protostellar disk fragmentation models show that no model unanimously predicts all parameters.

Gravitational disk instability:

- The simulation of *Vigan et al. 2017* outputs objects which mass and semi-major axis are similar to HD18757B and that are compatible with single systems.
- This formation model is appropriate for companions with semi-major axis of at least 30-50 AU without scattering. With external interactions, the semi-major axis can decrease and thus explain the HD18757B angular separation of 20 AU.
- Brown dwarfs with mass smaller than 40 M_{jup} are more likely to be formed in a protoplanetary disk than via protostellar disk fragmentation according to *Ma & Ge 2014*.

Protostellar disk fragmentation:

- The simulation of *Bate 2009* outputs 18 very low mass binaries out of 1254 stars considering the protostellar disk fragmentation scenario.
- Binaries with host star ranging in [0.5, 0.8] M_{sun}, have companions revolving on orbits with a semi-major axis within [27, 65] AU and longer simulations reveal that semi-major axes decrease due to external interactions.
- This model simulates binaries with low mass ratio but it is not the common solution.
- High eccentricity are found at small angular separations.

In summary, both models are adequate to explain the formation of HD18757B and their suitability is outlined in Table 6.1.

Formation model	Gravitational disk instability	Protostellar disk fragmentation
mass	predicted	predicted
semi-major axis	predicted with scattering	predicted with scattering
mass ratio	not shown	not common
eccentricity	predicted with scattering	predicted

TABLE 6.1: Comparison between the Gravitational disk instability and Protostellar disk fragmentation formation models for different parameters. Green cells represent good agreement, orange is medium agreement for HD18757B. Comments "predicted with scattering" mean that the parameters value fit the model when scattering is accounted and do not fit it otherwise.

7 Perspectives

The angular differential imaging analysis, the evolutionary model review and the spectral type discussion outcome a cold, faint and old substellar companion. In order to verify those predictions and especially to retrieve the spectrum of the companion, the latter must be imaged via a ground-based or space-based telescope.

As already introduced in section 1, imaging an object in a binary system is challenging in many ways. Current instruments observe in the infrared to overcome the large difference in luminosity in the visible between the companion and the parent star, use adaptive optics to suppress atmospheric perturbations, diminish the host star light with coronagraphic masking, improve instrument's resolution due to the small angular separation and many more. With regards to those constraints and predicted features of our companion, it is interesting to review instruments suitable for the observation of HD18757B.

Besides direct imaging, improvements in astrometry can provide more accurate information on the companion and predictions about its positioning. These more precise measurements along with direct imaging would detect and uniquely characterize the substellar object.

7.1 Ground-based telescopes

Important characteristics to take into account for suitable ground-based telescopes are the contrast, the inner working angle, the range of wavelengths covered and the location of the telescope. HD18757B is supposed to be faint with a contrast of the order of 10^{-6} and its angular separation is approximated to 0.9 arcsec from its host star. Moreover from the spectral type discussion, it was concluded that this object may be a late T-type or an early Y-type, thus imposing observation in the J-, H-band and covering specific methane or ammonia absorption band analogous to wavelengths in [1,2.5] µm. Furthermore, the star coordinates are 46.04° in right ascension and 61.706° in declination, thus imposing observation mostly from the Northern Hemisphere. More precisely, the declination must be at least 90° north or at most 90° south from the telescope's latitude for the star to be circumpolar [13].[55]
That is:

$$\begin{aligned} DEC + lat &\geq 90^\circ \quad \text{For an observer in the Northern Hemisphere} \\ DEC + lat &\leq -90^\circ \quad \text{For an observer in the Southern Hemisphere} \end{aligned} \tag{7.1}$$

Similarly, a star is never visible at a given latitude following:

$$\begin{aligned} DEC - lat &\leq -90^\circ \quad \text{For an observer in the Northern Hemisphere} \\ DEC - lat &\geq 90^\circ \quad \text{For an observer in the Southern Hemisphere} \end{aligned} \tag{7.2}$$

Combinations in between imply a partial visibility.[56]

Regarding these conditions, it is seen that telescopes located in the Northern Hemisphere are more appropriate to observe HD18757B that is situated in the Northern Hemisphere of the celestial sphere. With Figure 7.1, it is possible to compute the visibility of our star for several telescopes, based on the rules previously introduced. It follows:

- Large Binocular Telescope: $61.706 + 32.701 = 94.407^\circ \geq 90^\circ$
  The star is always visible for the LBT. However, this is only true for good observation conditions in view of the weather variability at this location.

[13] A star is said to be circumpolar for a given latitude if it is always visible in the sky.

- Subaru Telescope: 61.706 + 19.825 = 81.531° $\not\geq$ 90°
  As it is not circumpolar, it is necessary to verify whether it is partially seen or not at all: 61.706 - 19.825 = 81.531° $\not\leq$ -90°
  The star can be observed from Subaru. Note that since the Thirty Meter Telescope is planned to observe from Hawaii, the visibility analysis is similar.

- Very Large Telescope: 61.706 - 24.625 = 37.081° $\not\leq$ -90°
  The condition for an observer in the Southern Hemisphere is not verified so it follows: 61.706 + 24.625 = 86.331° $\not\geq$ 90°
  Although the non-visibility criterion is not met, it is relatively close. In practice, the star must be seen at least +50° from the zenith to have a large field rotation in a reasonable amount of time. Therefore telescopes located in Chile such as the Very Large Telescope, the Extremely Large Telescope and the Giant Magellan Telescope are not relevant for the observation of HD18757B given their location.

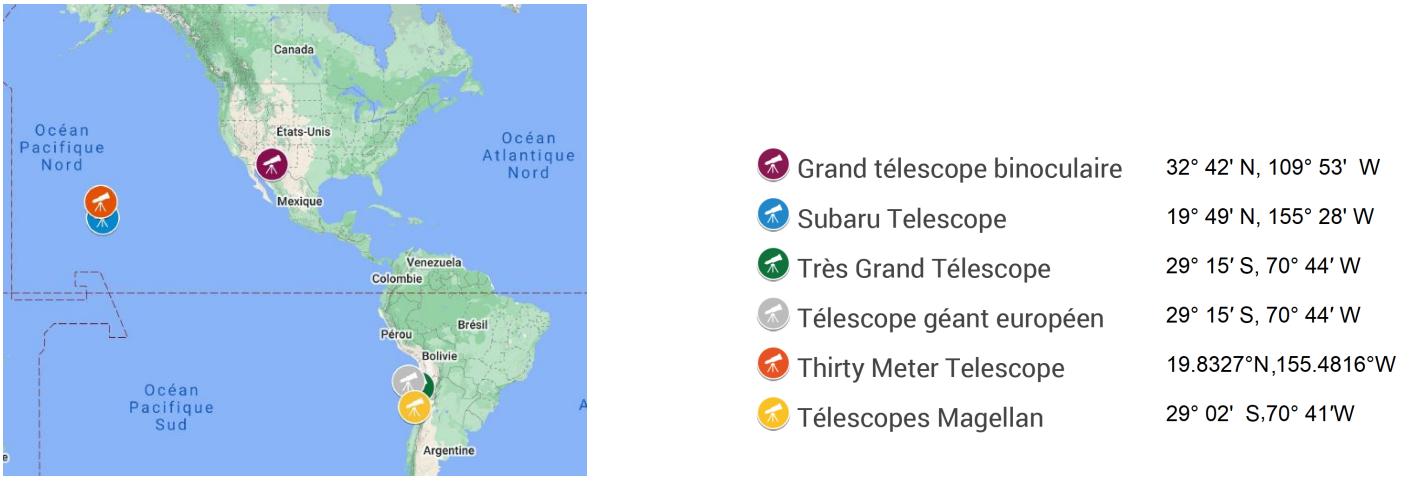

FIGURE 7.1: Positioning of different imaging telescopes marked by symbols on the map, and their corresponding coordinates. Realised with Google Maps.

Now that the telescope's location is constrained to the Northern Hemisphere, it is essential to review performances in terms of the angular resolution, contrast and spectral resolution.

The spectral resolution of a spectrograph is its ability to distinguish features in the electromagnetic spectrum. It is usually given in terms of the resolving power of the instrument, that is:

$$R = \frac{\lambda}{\Delta\lambda} \tag{7.3}$$

Where R is the resolving power, λ is the wavelength at which the instrument observe and $\Delta\lambda$ is the difference in wavelengths that can be distinguished in the spectrum.[23]
From Figure 7.3, it is seen that for a given wavelengths range, correspondingly a band filter, higher resolving power lead to higher spectral resolution.

LBT
Large Binocular Telescope is the first telescope which observed HD18757 with high contrast imaging via the instrument LMIRCam. Unfortunately, the scientific images obtained have a very low contrast and did not highlight any companion, confer section 3.
Nevertheless, the LBT is currently upgrated with new instruments such as SHARK-NIR and SHARK-VIS.[3] They are both designed for coronagraphic imaging, one in the infrared and the other in the visible and cover together wavelengths from 0.5 µm to 1.7 µm. Especially, SHARK-NIR is commissioned to observe in the Y, J and H bands which are the filters of interest to detect Y dwarfs. The SHARK instruments,

standing for System for coronagraphy with High order Adaptive optics from R to K band, also enable spectroscopic observation with two modes: a low-resolution mode with R $\approx$ 100 and a high-resolution mode with R $\approx$ 700. The SHARK instruments are planned to be mounted on the LBT by the end of 2021.[57]

GPI

Gemini Planet Imager is observing over a wavelength range of [0.95,2.4] µm and is able to target planets with a contrast of 10^{-7} for a stellar magnitude I = 6mag and at an angular separation of 0.13 arcsec.[1] Accordingly, GPI is able to image at Y, J and H bands which contain specific features to Y-type brown dwarfs.[58]
More specifically, Figure 7.6 shows that an object at an angular separation of 0.9 arcsec with a contrast of 10^{-6} is expected to be seen with GPI in the H band. Moreover, this instrument displays a spectral resolution of 44-49 in the H-band.
This instrument was originally built for the the Gemini South Telescope located in Chile but is currently updated and moved to Gemini North.[58] Gemini North Observatory is situated in Hawaii and thus is included in the range of acceptable latitudes for the observation of HD18757B.

Subaru

Subaru is a ground-based telescope observing from Maunakea, Hawaii. It is equipped with several instruments allowing observations in the visible and in the mid-infrared. One of the instruments is Subaru-CHARIS, Coronagraphic High Angular Resolution Imaging Spectrograph, which observes over wavelengths of [0.9, 2.4] µm.[1] This instrument operates in the JHK bands which are the spectral filters of interest for the determination of Y dwarfs features, confer to section 5.4. Besides the photometric capabilities, this instrument has a spectral resolution R = 65.2 in the H-band. The performances of CHARIS depend on the instrument SCExAO standing for Subaru Coronagraphic Extreme Adaptive Optics.[59] In particular, SCExAO detection contrast threshold at 500-800 mas is of the order of 5e-6 and at 1000 mas is around 1e-6.[60] The contrast curve in terms of the angular separation is provided in Figure 7.2. This graph shows that object, orbiting around stars with H = 5.3 mag, located at 0.9 arcsec with contrast of 10^{-5} would be detected with Subaru. Considering that the star HD18757 has a magnitude in the H band of 5.115, this graph can be taken as an example for possible detection of HD18757B via Subaru.[61]

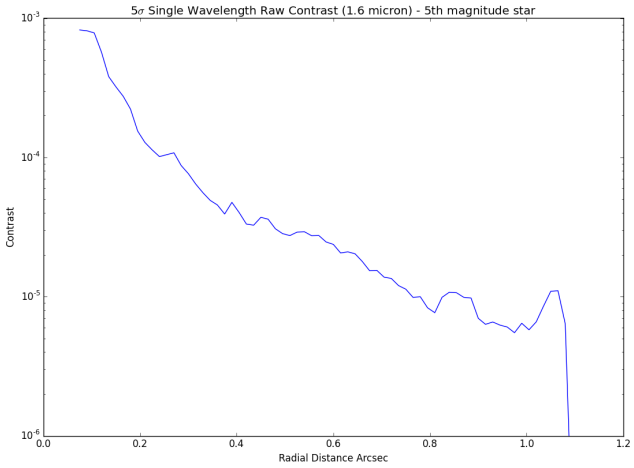

FIGURE 7.2: 5-sigma contrast level provided by SCExAO around a star with Hmag=5.3 from first-light measurements.[59]

TMT

Thirty Meter Telescope, as the name suggests, is a ground-based telescope with a primary mirror aperture of 30 m. This project is currently under development and is planned to be completed in July 2027. This telescope will be equipped with several instruments with high imaging performances including IRIS, the InfraRed Imager and Spectrometer, and PSI, the Planetary System Instrument. IRIS enables observations in the J, H and K+ bands with spectral resolution of the order of 4000-8000, while PSI covers wavelengths from 1 to 5 µm and inner working angle of 10 mas.[62]
In particular, Figure 7.6 depicts TMT contrast curve and informs that this telescope would be able to observe an object such as HD18757B.

7.2 Space-based telescopes

The particularity of space telescopes remains in atmospheric free perturbations, hence improving imaging quality. Nonetheless, these telescopes are high cost instruments and require accurate and robust design which leads to long and extensive creation processes.

JWST
James Webb Space Telescope is a NASA mission which launch is scheduled for October 2021. It is equipped with two imagers: NIRCam, the Near Infrared Camera, and MIRI, the Mid-Infrared Instrument. NIRCam provides high-contrast imaging for wavelengths ranging within [1, 5] µm as shown in Figure 7.3, while MIRI is composed of a camera and a spectrograph observing in the mid-infrared from 5 to 28 µm. Accompanying the imaging instruments, NIRSpec, Near-Infrared Spectrograph, enables low- and medium-resolution spectroscopy.[63]

WFIRST
Wide Field Infrared Survey Telescope, newly renamed Nancy Grace Roman Space Telescope is a NASA mission currently under development and foreseen for 2025. It is equipped with two main instruments: the Wide Field Instrument and the Coronagraph Instrument. The coronagraph is predicted to '*be capable of detecting planetary companions a billion times fainter than their host star and located > 0.15" away*'.[64]

HabEx
The Habitable Exoplanet Imaging Mission, is a space telescope which aims to image exoplanets, to retrieve their spectrum in order to assess their habitability and to extend our understanding of the universe.[1] This NASA mission which is envisioned for 2030, is based on a telescope equipped with a coronagraph, a starshade, a camera and a UV spectrograph. The camera is functional in the visible and mid-infrared at $\lambda \in [0.37, 1.8]$ µm. As for the starshade instrument and the coronagraph, they act as starlight suppression technology in order to enable observation of companions close to their star. Moreover, its coronagraph is designed to reach instrument contrast of the order of 10^{-10}. Regarding its structure, '*The overall HabEx design has been optimized for high-contrast direct imaging at small angular separations and broad spectroscopy of Earth-sized and larger exoplanets*'. [65]

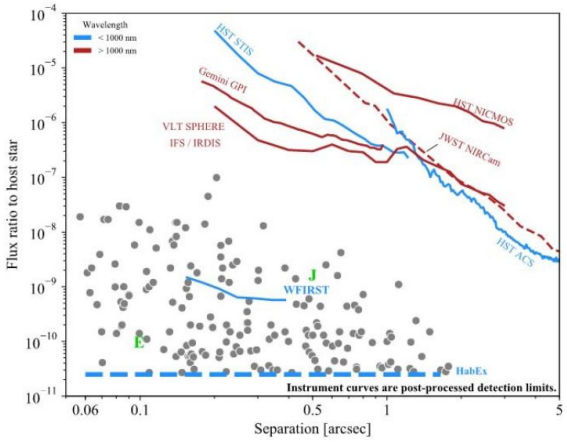

FIGURE 7.3: HabEx will detect and characterize newly discovered exoplanets at low planet-to-star flux ratios (grey points), enabling the first detailed studies of Earth-like planets in the habitable zone. Earth (E) and Jupiter (J) are shown for a solar system analog at 10 pc.[65]

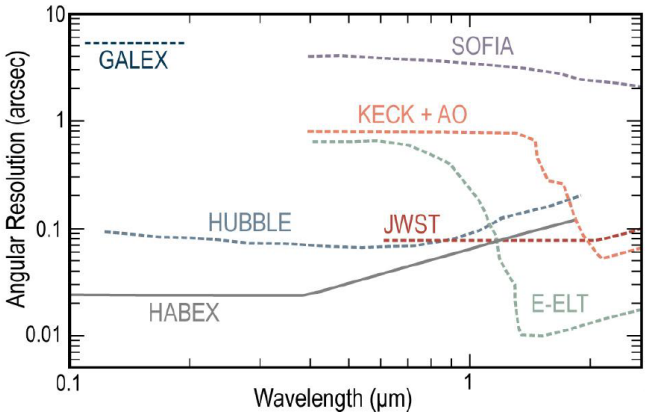

FIGURE 7.4: HabEx will provide the highest-resolution UV/optical images of any current or planned facility, enabling a broad suite of observatory science. Opportunities range from studies of solar system objects, the Milky Way Galaxy, nearby resolved stellar populations, high-redshift galaxies, and large-scale structure. Note: the assessment assumes that the extremely large telescopes will only achieve their theoretical diffraction limit around 1 μm.[65]

Even though HabEx is well suited to image exoplanets located within 10 pc, as depicted in Figure 7.3, a survey of potential direct imaging exoplanets for HabEx reports that over 5 years under ideal conditions, the mission could target exoplanets located up to 22 pc. [65]
From Figure 7.4 it can be noticed that HabEx shows high performance in terms of angular resolution in comparison to other actual and future space telescopes.
Taking into account all these considerations, it can be concluded that this mission could be appropriate to image HD18757B, located around 24 pc with a contrast of 10^{-6}.

LUVOIR
The large ultraviolet optical Infrared Surveyor is a NASA mission foreseen for 2030. This observatory is supplied with several instruments allowing observations of very faint objects. One of the instruments is ECLIPS, Extreme Coronagraph for Living Planetary Systems, which achieve contrast ratio of 10^{-10}. This high performance coronagraph will enable direct imaging of faint exoplanets. Another interesting instrument is HDI standing for High Definition Imager that observe at wavelengths in [0.2, 2.5] μm. Regarding the telescope, two architectures are considered: a 15-m diameter primary telescope and a 8-m telescope aperture. The former, LUVOIR A, provides high optical quality while the later, LUVOIR B, contributes to improve the performance in the observation of high-contrast exoplanets.[66]

LIFE
The Large Interferometer For Exoplanets aims to characterize the habitability of exoplanets by analyzing their spectra. This mission is based on a nulling interferometer concept consisting of several collector telescopes in formation flying.[67]
It will be able to directly image and measure spectra of a great number of small exoplanets over a wavelength range of 4 to 18.5 μm.[68] More particularly, the number of possible detections from different future missions is summarized in Figure 7.5. The graph does not exhibit the detection of Jovian size object,

such as HD18757B because they are not included in the simulation. However, regarding its predicted performances, this future mission remains an acceptable candidate for the imaging of our brown dwarf.

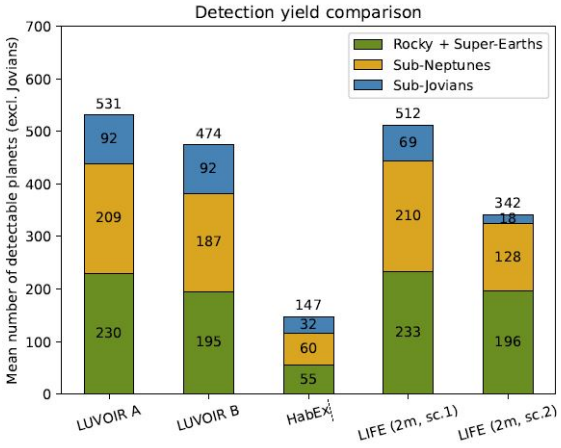

FIGURE 7.5: Detection yield comparison between LUVOIR A/B, HabEx, and LIFE. For LIFE we show the numbers for the D = 2 m reference case; for HabEx the numbers from the baseline 4-m concept. Jovian planets are not shown, because they were not included in the LIFE simulations.[68]

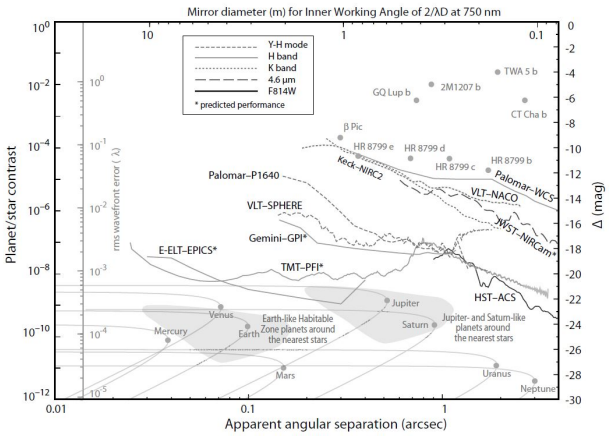

FIGURE 7.6: Current and projected high-contrast imaging performance of instruments from ground and space as a function of angular separation. The left axis shows the planet/star contrast, and the corresponding required rms wavefront quality. The right axis shows the corresponding magnitude difference Δ mag relative to the star. All detectivity curves are 5σ, for 1-h integration. Adapted from *Mawet et al.* (2012b, Figure 1), with permission ©SPIE.[1]

Through this analysis, it is seen that several current and future[14] missions would be appropriate to detect cold and faint objects such as HD18757B. Spectroscopic and photometric characterization of this companion would increase our understanding on the mode of formation of such substellar objects, it would improve the specifications of Y-type dwarfs and it would allow to extract information about their atmospheric composition. As already explained, brown dwarfs formation model is ambiguous as it is currently explained via planet formation and star formation models. Moreover, the spectral type Y that is used to characterize cold and faint substellar object is still under definition. Especially, dwarfs detected and labelled as Y-type are in an isolated system. Therefore, HD18757B is a unique object orbiting a sun-like star for more than 10 Gyr and would be the first observed Y dwarf in a binary system.

[14]Note that space missions HabEx, Luvoir and Life are still projects under study.

7.3 Astrometric measurements

In December 2020, the Gaia Early Data Release 3 (GDR3) was released, which is the successor of Gaia second data release (GDR2).[14]
It contains celestial positions, apparent magnitude in the G band, parallax and proper motions for more than 1 billion stars.

This new catalog presents much higher performances with an increase in 30% in precision for parallax and an increase of a factor 2 in precision for proper motion measurements.[69]
The observations lasted 34 months and covered the period from July 2014 to May 2017. This period corresponds to the retreat of the companion towards the apogee so it will not provide information around the RV peak that occurs at the perigee. However, these updated measurements can be included in the MCMC analysis in order to improve the evaluation on the orbital parameters, especially the inclination and the longitude of ascending node, the companion's mass and the positions predictions for the imaging. More specifically, with more accurate proper motion measurements, we can better estimate the angular separation of the companion around the star.

A subsequent release called GDR3 for Gaia Data release 3 is expected for 2022. It will complete the EDR3 with information about object classification, astrophysical parameters, non-single stars, quasars[15] and many more.[69]
The final catalog named DR4 is expected in late 2023 and will contain individual astrometric measurements from Gaia.[69]

[15]Quasar stands for QUAsi Stellar Astronomical Radio Source, they are found in the center of galaxies and appear to be highly luminous.[15]

Conclusion

The goal of the thesis is the characterization of the substellar companion HD18757B. The angular differential imaging analysis consists in a pre- and post-processing of the LMIRCam data. Detection algorithms are run on this ADI-cube but show no presence of the object. This non-detection, due to the imaging detection limits, implies an old and faint companion with a contrast of the order of 10^{-6}. In addition to the non-detection, the VIP methodology and limitations are verified by injecting fake companions at different contrast levels and by analysing an extra dataset. This verification reveals that objects with contrast lower than 10^{-4} are not found with the VIP methodology.

Combining the radial velocity measurements and astrometry information, the orbital parameters and the dynamical mass of HD18757B are determined via the Markov-Chain Monte Carlo technique. The orbital parameters depict a highly elliptical wide-orbit which is tilted with respect to the line of sight. On account of the lack of measurements in astrometry and the non-detection in direct imaging, the inclination and the longitude of ascending node are not uniquely constrained leading to 2 sets of solutions: prograde and retrograde orbits. Despite these two solutions, the companion's mass is well constrained and estimated to $36.528^{+2.261}_{-2.134}$ M_{jup} which strengthens the brown dwarf nature of the companion. Furthermore, the MCMC simulation predicts the object positions for past and future epochs. The predicted positions denote that the companion is currently moving away from its host star, thus improving the detection likelihood via direct imaging.

With the mass determined from the MCMC analysis, parameters such as luminosity, radius and effective temperature are derived from evolutionary model predictions. This evolutionary model analysis is based on several hypotheses: the companion's age is assumed to 11.4 Gyr which is the estimated age of its host star and its metallicity is set to -0.3 dex that is similar once again to its parent star. With such low mass and advanced age, the predicted range of luminosities and effective temperatures are pretty low, consistent with the non-detection in direct imaging. More specifically, for a companion nominal mass of 0.035 M_{sun}, the effective temperature is predicted within a range of [514, 534] K, its radius is approximately [0.0849, 0.0862] R_{jup} and the luminosity is varying within [-6.321, -6.283].

From the outcome of the evolution model study, we conclude that the properties of the brown dwarf companion are compatible with an object with a cloudless atmosphere and two spectral types: late T-type and early Y-type brown dwarf that can be distinguished via their spectrum. In particular, T-type brown dwarfs are identifiable due to strong methane absorption bands, whereas Y-type brown dwarfs are distinctive through ammonia absorption bands in their spectra.
In parallel to evolutionary models, a discussion on formation models highlights two formations scenario: Gravitational disk instability for planets and Protostellar disk fragmentation for stars. The prior model predicts similar objects to HD18757B in terms of semi-major axis, mass and eccentricity. The second formation model predicts as well several features of the object such as the eccentricity, the mass, the semi-major axis and the mass ratio with its host star. At the end of the discussion, it is concluded that no model characterizes uniquely the object, nor is the more appropriate for brown dwarf formation.

In order to confirm the spectral type assumption, the object must be imaged through ground-based or space-based telescopes to measure its spectrum and luminosity. However due to its faintness and proximity to its parent star, around 0.9 arcsec, imaging such an object is difficult and requires high contrast instruments. Within these considerations, it is established that several ground-based and future space-based telescopes are suitable for the observation of our system. For observations from Earth, the telescopes are limited to the Northern Hemisphere restricting the observations to Subaru, Gemini North, Thirty meter Telescope and the Large Binocular Telescope. For observation from space, the review reveals several appropriate missions under development such as the James Webb Space Telescope, the Nancy Grace Roman Telescope, the HabEx and Luvoir projects or even the Life mission.
Astrometric future measurements are also considered with the new Gaia Early Release 3 that has more accurate measurements. This new catalog could constrain more precisely the orbital parameters and lift

the uncertainty on the inclination and longitude of ascending node, thus narrowing down the two sets of solutions to one orbit family.

In conclusion, this study revealed the characteristics of a unique substellar object HD18757B. This brown dwarf companion is the first known Y-type evolving in such an old binary system, assuming that the age hypothesis is reliable. Future observations will allow to confirm our conclusion and for thorough tests of brown dwarfs evolution, formation models and atmosphere composition.

Acknowledgements

First of all, I would like to specially thank my supervisor Ms. Maire who was very present during my internship. Her advice guided and encouraged me all along this project. I also wish to thank her for her patience and her confidence as the subject was new to me. The numerous discussions that we shared helped me to seek performance through the realisation of my master thesis.

Secondly, I would like to thank Mr. Loicq for his writing advice and his interest in my work.

I am grateful for the positive feedback and interest from my thesis committee.

I also wish to express my appreciation to Mr.Broun who helped me to find this internship. Without his contribution, I would not have been able to explore and learn so much about the exoplanet research field.

Lastly, I would like to express my deepest gratitude for my lovely parents who supported me through this journey.

Glossary

ADI Angular Differential Imaging is a high contrast direct imaging technique. 7–9, 12, 17

BURR97 Burrows 1997 is an evolutionary model used to describe properties, such as effective temperature, luminosity and radius, of giant planets and brown dwarfs. 33, 41

CA Core Accretion is a formation model developed for planets. 47

COND03 Baraffe et al. 2003 is a evolutionary model used to describe properties, such as effective temperature, luminosity and radius, of extrasolar giant planets and cool brown dwarfs with cloudless atmosphere. 33, 41

DUSTY Chabrier 2000 is a evolutionary model used to describe properties, such as effective temperature, luminosity and radius, of very low-mass stars and brown dwarfs with dusty atmosphere. 33

FWHM Full width at half maximum represents the wideness of the point spread function at half maximum. 12, 13, 17

GDR2 Second data release from the Gaia ESA mission which gathers astrometric measurements of several stars. 10, 11

GI Gravitational Instability is a formation model developed for planets. 47

HD18757 Star observed via the Large Binocular Telescope, detected via spectrographs Sophie and Elodie and measured with Gaia and Hipparcos. It is the host star of the companion of interest in this study. 7

LOCI Locally optimized combination of images is a set of methods for the creation of a reference PSF in the ADI post-processing. 8, 9

MCMC Markov-Chain Monte Carlo is a method used to fit a set of parameters on data. 20, 22, 23, 28, 29, 31

PC Principal components of the PCA methodology. 9

PCA Principal component analysis is a set of methods for the creation of a reference PSF in the ADI post-processing part. 8, 9, 17

PM Proper motion is described with the coordinates on the celestial sphere. 10, 11

PMa Proper motion anomaly is the difference between the long-term proper motion that is associated to the center of mass of the system, and the short-term proper motion is caused by a companion orbiting the star, making it wobbling around the barycenter.. 10

PSF Point Spread Function characterizes the intensity distribution of the point source over the image. 7, 9, 12, 17

RV Radial Velocity detection technique is an indirect exoplanet detection method. It consists in measuring periodic shifts of spectral lines in the spectrum of stars. 9, 10, 28–30

SM08 Saumon 2008 is an evolutionary model used to describe properties, such as effective temperature, luminosity and radius, of L and T dwarfs. 33

SNR Signal-to-noise ratio assesses the level of the desired signal over the background noise. 14

VIP Vortex Imaging Processing is a python package, developed by the University of Liège, used for the pre- and post-processing on ADI dataset. 12, 14–17, 35

VLM Very Low Mass object which mass is smaller than 0.1 M_{sun}. 49

References

[1] Michael Perryman. *The Exoplanet Handbook*. Cambridge University Press, 2018.

[2] Díaz, R. F., Delfosse, X., Hobson, M. J., Boisse, I., Astudillo-Defru, N., Bonfils, X., Henry, G. W., Arnold, L., Bouchy, F., Bourrier, V., Brugger, B., Dalal, S., Deleuil, M., Demangeon, O., Dolon, F., Dumusque, X., Forveille, T., Hara, N., Hebrard, G., ... Wilson, P. A. "The SOPHIE search for northern extrasolar planets." In: *Astronomy & Astrophysics* 625 (2019). DOI: https://doi.org/10.1051/0004-6361/201935019.

[3] LBTO. *Large Binocular Telescope Observatory - Futur instruments*. Accessed 25 May 2021. URL: https://www.lbto.org/future-instruments.html.

[4] Christian Marois, David Lafrenie, Rene Doyon, Bruce Macintosh, Daniel Nadeau. "Angular differential imaging: a powerful high-contrast imaging technique". In: *The Astrophysical Journal* (2006). URL: https://iopscience.iop.org/article/10.1086/500401.

[5] Carlos Alberto Gomez Gonzalez. *VIP - Vortex Image Processing package*. Accessed 27 May 2021. URL: https://github.com/vortex-exoplanet/VIP.

[6] Cantalloube, F., Gomez-Gonzalez, C., Absil, O., Cantero, C., Bacher, R., Bonse, M., Bottom, M., Dahlqvist, C.-H., Desgrange, C., Flasseur, O., Fuhrmann, T., Henning, T. H., Jensen-Clem, R., Kenworthy, M., Mawet, D., Mesa, D., Meshkat, T., Mouillet, D., Müller, A., ... Van Droogenbroeck, M. "Exoplanet imaging data challenge: benchmarking the various image processing methods for exoplanet detection". In: (2020). DOI: https://doi.org/10.1117/12.2574803.

[7] A.-L Maire et al. "A dusty benchmark brown dwarf near the ice line of HD 72946". In: *A&A* 633 (2020), p. 2. DOI: 10.1051/0004-6361/201937134. URL: https://doi.org/10.1051/0004-6361/201937134.

[8] Baraffe, I., Chabrier, G., Barman, T. S., Allard, F., & Hauschildt, P. H. "Evolutionary models for cool brown dwarfs and extrasolar giant planets. The case of HD 209458." In: *Astronomy and Astrophysics* (2003). DOI: https://doi.org/10.1051/0004-6361:20030252.

[9] Chabrier, G., Baraffe, I., Allard, F., & Hauschildt, P. H. "Evolutionary models for very low-mass stars and brown dwarfs with dusty atmopshere." In: *The Astrophysical Journal* (2000). DOI: https://doi.org/10.1086/309513.

[10] Saumon, D., & Marley, M. S. "The Evolution of L and T Dwarfs in Color-Magnitude Diagrams." In: *The Astrophysical Journal* (2008). DOI: https://doi.org/10.1086/592734.

[11] Burrows, A., Marley, M., Hubbard, W. B., Lunine, J. I., Guillot, T., Saumon, D., Freedman, R., Sudarsky, D., & Sharp, C. " A Nongray Theory of Extrasolar Giant Planets and Brown Dwarfs." In: *The Astrophysical Journal* (1997). DOI: https://doi.org/10.1086/305002.

[12] Vigan, A., Bonavita, M., Biller, B., Forgan, D., Rice, K., Chauvin, G., Desidera, S., Meunier, J. C., Delorme, P., Schlieder, J. E., Bonnefoy, M., Carson, J., Covino, E., Hagelberg, J., Henning, T., Janson, M., Lagrange, A. M., Quanz, S. P., Zurlo, A., ... Thalmann, C. "The VLT/NaCo large program to probe the occurrence of exoplanets and brown dwarfs at wide orbits." In: *Astronomy & Astrophysics* (2017). DOI: https://doi.org/10.1051/0004-6361/201630133.

[13] Bate, M. R. " Stellar, brown dwarf and multiple star properties from hydrodynamical simulations of star cluster formation". In: *Monthly Notices of the Royal Astronomical Society* (2009). DOI: https://doi.org/10.1111/j.1365-2966.2008.14106.x.

[14] ESA. *GAIA EARLY DATA RELEASE 3 (GAIA EDR3)*. Accessed 30 May 2021. URL: https://www.cosmos.esa.int/web/gaia/earlydr3.

[15] Pierre Magain. *Astrophysics course - University of Liège*. Accessed 31 May 2021. URL: http://www.astro.ulg.ac.be/~magain/PM_Main_Fr/Cours.html.

[16] N. Rumiano. *L'energie des etoiles*. Accessed 3 April 2021. URL: http://nrumiano.free.fr/Fetoiles/energie.html.

[17] Burgasser, A. J. "Brown dwarfs: Failed stars, super Jupiters." In: *Physics Today* 61 (2008), pp. 70–71. DOI: https://doi.org/10.1063/1.2947658.

[18] William & Deborah Hillyard. *Astronomy & Cosmology - Stars - Stellar Classes*. Accessed 8 April 2021. URL: http://www.whillyard.com.

[19] Taweewat Somboonpanyakul and Motohide Tamura, Department of Astronomy and Astrophysics, University of Chicago. *Directing Imaging Techniques of Exoplanets*. URL: https://www.s.u-tokyo.ac.jp/en/utrip/archive/2014/pdf/09TaweewatSoomboonpanyakul.pdf.

[20] Eugene Hecht. *Optique*. Pearson Education France, 2005.

[21] R. Nave. *The Rayleigh Criterion*. Accessed 22 May 2021. URL: http://hyperphysics.phy-astr.gsu.edu/hbase/phyopt/Raylei.html.

[22] Lumen. *Limits of Resolution: The Rayleigh Criterion*. Accessed 22 May 2021. URL: https://courses.lumenlearning.com/austincc-physics2/chapter/27-6-limits-of-resolution-the-rayleigh-criterion/.

[23] Professor S. Habraken. *Course: Coherent and incoherent optics*.

[24] European Space Agency. *Gaia*. Accessed 3 June 2021. URL: https://sci.esa.int/web/gaia/-/28890-objectives.

[25] Persson, C. M., Csizmadia, S., Mustill, A. J., Fridlund, M., Hatzes, A. P., Nowak, G., Georgieva, I., Gandolfi, D., Davies, M. B., Livingston, J. H., Palle, E., Rodríguez, P. M., Endl, M., Hirano, T., Prieto-arranz, J., Korth, J., Grziwa, S., Esposito, M., Albrecht, S., ... Eigmüller, P. "Astrophysics Greening of the brown-dwarf desert". In: *Astronomy and Astrophysics* 628 (2019). DOI: https://doi.org/10.1051/0004-6361/201935505.

[26] The Editors of Encyclopaedia. Britannica. *Henry Draper Catalogue*. Accessed 30 May 2021. URL: https://www.britannica.com/topic/Henry-Draper-Catalogue..

[27] Kervella, P., Arenou, F., Mignard, F., & Thevenin, F. "Stellar and substellar companions of nearby stars from Gaia DR2: Binarity from proper motion anomaly." In: *Astronomy & Astrophysics* 623 (2019). DOI: https://doi.org/10.1051/0004-6361/201834371.

[28] Christian Thalmann. *A short introduction to Angular Differential Imaging*. Accessed 15 May 2021. URL: http://web.archive.org/web/20150915005746/http://www.mpia.de/homes/thalmann/adi.htm.

[29] Flasseur, O., Denis, L., Thiebaut, E., & Langlois, M. "Exoplanet detection in angular differential imaging by statistical learning of the non stationary patch covariances: The PACO algorithm." In: *Astronomy and Astrophysics* 618 (2018). DOI: https://doi.org/10.1051/0004-6361/201832745.

[30] Carlos Alberto Gomez Gonzalez. *High-contrast imaging post-processing methods for exoplanet detection and characterization*. Accessed 26 May 2021. URL: https://speakerdeck.com/carlgogo/high-contrast-imaging-post-processing-methods-for-exoplanet-detection-and-characterization?slide=21.

[31] Gomez Gonzalez, C. A., Wertz, O., Absil, O., Christiaens, V., Defrère, D., Mawet, D., Milli, J., Absil, P. A., van Droogenbroeck, M., Cantalloube, F., Hinz, P. M., Skemer, A. J., Karlsson, M., & Surdej, J. "Vip: Vortex Image Processing Package for High-Contrast Direct Imaging." In: *ArXiv* 154 (2017). DOI: https://doi.org/10.3847/1538-3881/aa73d7.

[32] Ram Chandra Gotame. *Radial Velocity Method or Doppler Spectroscopy for Finding the Exoplanets*. Accessed 13 May 2021. URL: https://physicsfeed.com/post/radial-velocity-method-or-doppler-spectroscopy-finding-exoplanets/.

[33] Wright, J. T. *Radial velocities as an exoplanet discovery method. Handbook of Exoplanets*. Springer International Publishing, 2018, pp. 619–631. URL: https://doi.org/10.1007/978-3-319-55333-7_4.

[34] A. Baranne et al. "ELODIE: A spectrograph for accurate radial velocity measurements." In: *Astronomy and Astrophysics* (1996).

[35] S.A.Ilovaisky & H.Le Coroller. *SOPHIE échelle spectrograph*. Accessed 8 June 2021. URL: http://www.obs-hp.fr/guide/sophie/sophie-eng.shtml.

[36] The Editors of Encyclopaedia Britannica. *AProper motion*. Accessed 31 May 2021. URL: https://www.britannica.com/science/proper-motion.

[37] European Space Agency. *The Hipparcos space astrometry mission*. Accessed 3 June 2021. URL: https://www.cosmos.esa.int/web/hipparcos.

[38] The planetary Society. *Wobbly Stars: The Astrometry Method*. Accessed 18 May 2021. URL: https://www.planetary.org/articles/wobbly-stars-the-astrometry-method.

[39] the free encyclopedia Wikipedia. *Full width at half maximum*. Accessed 30 May 2021. URL: https://en.wikipedia.org/wiki/Full_width_at_half_maximum.

[40] eHelp Corporation. *Nyquist Sampling*. Accessed 30 May 2021. URL: https://cdn.diffractionlimited.com/help/microccd/Nyquist_Sampling.htm.

[41] Yves Usson. *Traitement d'images numeriques en microscopie*. Accessed 30 May 2021. URL: http://membres-timc.imag.fr/Yves.Usson/COURS/Cours-TNT-YU-1.pdf.

[42] Universite de Strasbourg/CNRS. *VizieR Photometry viewer*. Accessed 1 June 2021. URL: http://vizier.u-strasbg.fr/vizier/.

[43] Imad Pasha. *MCMC: A (very) Beginnner's Guide*. Accessed 12 May 2021. URL: https://prappleizer.github.io/Tutorials/MCMC/MCMC_Tutorial.html.

[44] Howard Curtis. *Orbital mechanics for engineering students*. Elsevier Butterworth-Heinemann, 2005.

[45] Dan Foreman-Mackey. *Autocorrelation time estimation*. URL: https://dfm.io/posts/autocorr/.

[46] Evan Kiefl. *Integrated autocorrelation time and its relationship with MCMC convergence*. Accessed 16 May 2021. URL: https://rstudio-pubs-static.s3.amazonaws.com/258436_5c7f6f9a84bd47aeaa33ee763e5html.

[47] Murray, C. D., & Correia, A. C. M. "Keplerian Orbits and Dynamics of Exoplanets." In: (2011). URL: https://arxiv.org/abs/1009.1738v2.

[48] Astrobiology Magazine. *Gyrochronology*. Accessed 4 June 2021. URL: https://www.astrobio.net/cosmic-evolution/gyrochronology/.

[49] CosmoStat. *Asteroseismology*. Accessed 4 June 2021. URL: https://www.cosmostat.org/research-topics/asteroseismology.

[50] Burrows, A., Heng, K., & Nampaisarn, T. "The dependence of brown dwarf radii on atmospheric metallicity and clouds: Theory and comparison with observations". In: *Astrophysical Journal* 736 (2011). DOI: https://doi.org/10.1088/0004-637X/736/1/47.

[51] The Astrophysics Spectator. *The Structure and Evolution of Brown Dwarfs*. Accessed 3 June 2021. URL: https://astrophysicsspectator.org/topics/degeneracy/BrownDwarfStructure.html.

[52] Burgasser, Adam J.; Geballe, Thomas R.; Golimowski, David A.; Leggett, Sandy K.; Kirkpatrick, J. Davy; Knapp, Gillian R.; Fan, Xiaohui. *The Classification of T Dwarfs*. Vol. 211. Martin, Eduardo, 2003, pp. 377–384. URL: https://ui.adsabs.harvard.edu/abs/2003IAUS..211..377B.

[53] Kirkpatrick, J. D., Gelino, C. R., Cushing, M. C., MacE, G. N., Griffith, R. L., Skrutskie, M. F., Marsh, K. A., Wright, E. L., Eisenhardt, P. R., McLean, I. S., Mainzer, A. K., Burgasser, A. J., Tinney, C. G., Parker, S., & Salter, G. "Further defining spectral type "y" and exploring the low-mass end of the field brown dwarf mass function". In: *Astrophysical Journal* 753 (2012). DOI: https://doi.org/10.1088/0004-637X/753/2/156.

[54] Cushing, M. C., Kirkpatrick, J. D., Gelino, C. R., Griffith, R. L., Skrutskie, M. F., Mainzer, A., Marsh, K. A., Beichman, C. A., Burgasser, A. J., Prato, L. A., Simcoe, R. A., Marley, M. S., Saumon, D., Freedman, R. S., Eisenhardt, P. R., & Wright. "The discovery of y dwarfs using data from the wide-field infrared survey explorer (WISE)". In: *Astrophysical Journal* 743 (2011). DOI: https://doi.org/10.1088/0004-637X/743/1/50.

[55] Hirsch Observatory. *Planning Observations - Observational Astronomy*. URL: https://www.rpi.edu/dept/phys/observatory/obsastro6.pdf.

[56] FlatEarth.ws. *Determining the Visibility of a Star From Its Declination and the Observer's Latitude*. Accessed 26 May 2021. URL: https://flatearth.ws/star-visibility.

[57] Farinato, J., Bacciotti, F., Baffa, C., Baruffolo, A., Bergomi, M., Bianco, A., Bongiorno, A., Carbonaro, L., Carolo, E., Carlotti, A., Chinellato, S., Close, L., de Pascale, M., Dima, M., D'Orazi, V., Esposito, S., Fantinel, D., Farisato, G., Gaessler, W., ... Zanutta, A. "SHARK-NIR, the coronagraphic camera for LBT, moving toward construction". In: *ArXiv* (2018). DOI: https://doi.org/10.26698/ao4elt5.0074.

[58] Gemini Observatory. *GPI - Instrument Configuration*. Accessed 25 May 2021. URL: https://www.gemini.edu/instrumentation/gpi/components.

[59] Princeton University. *CHARIS, Coronagraphic High Angular Resolution Imaging Spectrograph*. Accessed 24 May 2021. URL: https://scholar.princeton.edu/charis.

[60] National Astronomical Observatory of Japan Subaru Telescope. *SCExAO, Subaru Coronographic Extreme Adaptive Optics*. Accessed 24 May 2021. URL: https://www.naoj.org/Projects/SCEXAO/scexaoWEB/010usingSCExAO.web/010currentcap.web/040highcontrastimaging.web/indexm.html.

[61] SIMBAD4 rel 1.7 - 2021.05.19. *hd 18757*. Accessed 15 May 2021. URL: http://simbad.u-strasbg.fr/simbad/sim-basic?Ident=hd+18757&submit=SIMBAD+search.

[62] TMT- International Observatory. *Overview of instruments capabilities*. Accessed 25 May 2021. URL: https://www.tmt.org/page/instrument-overview.

[63] NASA - Rob Garner. *The James Webb Space Telescope Instruments*. Accessed 26 May 2021. URL: https://www.nasa.gov/mission_pages/webb/instruments/index.html.

[64] Tony Greicius, Randal Jackson, Naomi Hartono. *Exoplanets and Astrophysics Mission-The Nancy Grace Roman Space Telescope*. Accessed 26 May 2021. URL: https://www.jpl.nasa.gov/missions/the-nancy-grace-roman-space-telescope.

[65] B. Scott Gaudi et al. "The Habitable Exoplanet Observatory (HabEx) Mission Concept Study Final Report". In: (2020). URL: https://arxiv.org/abs/2001.06683v2.

[66] J.D. Myers. *LUVOIR*. Accessed 26 May 2021. URL: https://asd.gsfc.nasa.gov/luvoir/design/.

[67] LIFE project team. *LIFE - Large Interferometer For Exoplanets*. Accessed 27 May 2021. URL: https://www.life-space-mission.com/the-project/technology/.

[68] LIFE collaboration, Quanz, S. P., Ottiger, M., Fontanet, E., Kammerer, J., Menti, F., Dannert, F., Gheorghe, A., Absil, O., Airapetian, V. S., Alei, E., Allart, R., Angerhausen, D., Blumenthal, S., Cabrera, J., Carrión-González, Ó., Chauvin, G., Danchi, W. C., Dandumont, C., ... Wyatt, M. C. "Large Interferometer For Exoplanets (LIFE): I. Improved exoplanet detection yield estimates for a large mid-infrared space-interferometer mission." In: *ArXiv* (2021). URL: http://arxiv.org/abs/2101.07500.

[69] Klioner, S. A., Mignard, F., Lindegren, L., Bastian, U., McMillan, P. J., Hernández, J., Hobbs, D., Ramos-Lerate, M., Biermann, M., Bombrun, A., de Torres, A., Gerlach, E., Geyer, R., Hilger, T., Lammers, U., Steidelmüller, H., Stephenson, C. A., Brown, A. G. A., ... Zwitter, T. " Gaia Early Data Release 3." In: *Astronomy & Astrophysics* (2020). DOI: https://doi.org/10.1051/0004-6361/202039734.